Title
Interference management in multiple-antenna wireless networks

Permalink
https://escholarship.org/uc/item/0vc339j1

Author
Spyropoulos, Ioannis

Publication Date
2009

Peer reviewed|Thesis/dissertation

UNIVERSITY OF CALIFORNIA, SAN DIEGO

Interference Management in Multiple-Antenna Wireless Networks

A dissertation submitted in partial satisfaction of the
requirements for the degree
Doctor of Philosophy

in

Electrical Engineering (Communications Theory and Systems)

by

Ioannis Spyropoulos

Committee in charge:

Professor James R. Zeidler, Chair
Professor Robert R. Bitmead
Professor William S. Hodgkiss
Professor Laurence B. Milstein
Professor John G. Proakis

2009

The dissertation of Ioannis Spyropoulos is approved, and it is acceptable in quality and form for publication on microfilm and electronically:

_____

_____

_____

_____

_____

Chair

University of California, San Diego

2009

DEDICATION

To my beloved parents, Thanasis and Olga.

EPIGRAPH

"The credit belongs to the man who is actually in the arena, whose face is marred by dust and sweat and blood, who strives valiantly, who errs and comes up short again and again, because there is no effort without error or shortcoming, but who knows the great enthusiasms, the great devotions, who spends himself for a worthy cause; who, at the best, knows, in the end, the triumph of high achievement, and who, at the worst, if he fails, at least he fails while daring greatly, so that his place shall never be with those cold and timid souls who knew neither victory nor defeat."

– Theodore Roosevelt, *"Citizenship in a Republic,"* Paris, 1910

"Never discourage anyone who continually makes progress, no matter how slow."

– Plato

TABLE OF CONTENTS

LIST OF TABLES

ACKNOWLEDGEMENTS

First of all, I would like to thank my advisor, Dr. James R. Zeidler, for offering me the opportunity to pursue a Ph.D. degree at UCSD, for his guidance, patience, and support over the last seven years. I would also like to thank Prof. John G. Proakis for taking the time and interest to closely follow my research progress, read my papers, and offer me his invaluable advice. I am also grateful to Prof. Robert R. Bitmead, Prof. William S. Hodgkiss, and Prof. Laurence B. Milstein for serving as members of my committee. It would be an omittance not to thank Dr. William Cooper, Dr. Zhongren Cao, and Dr. Magnus Almgren for numerous helpful technical discussions during the first part of my research. Without them, my first journal paper would have just not been materialized.

I consider myself extremely lucky for having met an exceptional group of people throughout my Ph.D. studies at UCSD. Fellow graduate students and postdoc researchers who became not just close friends but something sort of a family to me; my international family. Many thanks to Kostas Stamatiou, Chandra Murthy, Jittra Jootar, Laddan Hashemian, Maziar Nezhad, Azadeh Bozorgzadeh, Cecile Levasseur, Mohamed Jalloh, Periklis Liaskovitis, Christina Chatzi, Marianna Dakanali, and Stella Vlachou for their companionship, for making my Ph.D. years so memorable.

Last but not least, I am deeply grateful to my parents Thanasis and Olga, my siblings Andromache and Nikos, and my grand-mother Despoina for their enormous moral support, encouragement, and patience during all this time that we have been apart. I would like to assure them that the journey of the past seven years was well worth it.

Chapter 2, in part, is a reprint of the material as it appears in I. Spyropoulos and J. R. Zeidler, "Dynamic Channel Allocation and Space-Time LMMSE Joint Detection in a TDD/CDMA Cellular Network with Traffic Asymmetry," *Proceedings of IEEE Vehicular Technology Conference (VTC)*, Dublin, Ireland, Apr. 2007, pp. 3066–3070 and I. Spyropoulos and J. R. Zeidler, "Supporting Asymmetric Traffic in a TDD/CDMA Cellular Network via Interference-Aware Dynamic Channel Allocation and Space-Time LMMSE Joint Detection," *IEEE Transactions on Vehicular Technology*, vol. 58, no. 2, pp. 744–759, Feb. 2009. The dissertation author was the primary investigator and author of these papers.

Chapter 3, in part, is a reprint of the material as it appears in I. Spyropou-

los and J. R. Zeidler, "A PHY-MAC Cross-Layer Protocol for Ad Hoc Networks with Multiple-Antenna Nodes," *Proceedings of IEEE International Conference on Communications (ICC)*, Dresden, Germany, June 2009. Additionally, it is currently being prepared for submission for publication of the material as I. Spyropoulos and J. R. Zeidler, "PHY-MAC Cross-Layer Protocols for Ad Hoc Networks with Linear Beamformers," in preparation, 2009. The dissertation author was the primary investigator and author of these papers.

VITA

1977	Born, Athens, Greece
2000	Diploma in Electrical and Computer Engineering National Technical University of Athens, Athens, Greece
2001	Graduate Teaching Assistant Stanford University, Stanford, California
2002	M.S. in Electrical Engineering Stanford University, Stanford, California
2002-2009	Graduate Research Assistant University of California at San Diego, La Jolla, California
2009	Ph.D. in Electrical and Computer Engineering University of California at San Diego, La Jolla, California
2009	Sr. Communication Systems Engineer MaxLinear Inc., Carlsbad, California

PUBLICATIONS

I. Spyropoulos and J. R. Zeidler, "Dynamic Channel Allocation and Space-Time LMMSE Joint Detection in a TDD/CDMA Cellular Network with Traffic Asymmetry," in *Proceedings of IEEE Vehicular Technology Conference (VTC)*, Dublin, Ireland, Apr. 2007, pp. 3066–3070.

I. Spyropoulos and J. R. Zeidler, "Supporting Asymmetric Traffic in a TDD/CDMA Cellular Network via Interference-Aware Dynamic Channel Allocation and Space-Time LMMSE Joint Detection," *IEEE Transactions on Vehicular Technology*, vol. 58, no. 2, pp. 744–759, Feb. 2009.

I. Spyropoulos and J. R. Zeidler, "A PHY-MAC Cross-Layer Protocol for Ad Hoc Networks with Multiple-Antenna Nodes," in *Proceedings of IEEE International Conference on Communications (ICC)*, Dresden, Germany, June 2009.

I. Spyropoulos and J. R. Zeidler, "PHY-MAC Cross-Layer Protocols for Ad Hoc Networks with Linear Beamformers," in preparation, 2009.

ABSTRACT OF THE DISSERTATION

Interference Management in Multiple-Antenna Wireless Networks

by

Ioannis Spyropoulos

Doctor of Philosophy in Electrical Engineering (Communications Theory and Systems)

University of California, San Diego, 2009

Professor James R. Zeidler, Chair

This dissertation focuses on the topic of interference management in wireless networks with multiple-antenna nodes. Two network paradigms are considered, namely, time-division duplexing (TDD)/code-division multiple-access (CDMA) cellular and ad hoc.

In TDD/CDMA cellular networks with asymmetric data traffic, dynamic channel allocation (DCA) enhances resource utilization compared to fixed channel allocation (FCA); however, it induces base-to-base and mobile-to-mobile crossed-slot intercell interference that can severely degrade network performance. To deal with this problem, a decentralized scheme is proposed, which combines an interference-aware DCA algorithm with space-time linear minimum-mean-square-error (LMMSE) joint detection at the base and mobile stations. The former assigns active links to timeslots in a way that crossed-slot interference is mitigated, while the latter suppresses the remaining intercell interference (along with intersymbol and intracell interference) by exploiting its spatio-temporal autocorrelation statistics. The performance of this scheme is evaluated in terms of SINR outage and average throughput via analytical approximations and Monte Carlo simulations, and it is compared with that of benchmark random DCA (RDCA)

and FCA schemes. The cases of single- and dual-antenna reception with perfect and imperfect channel state information are examined. It is shown that the proposed scheme achieves higher average throughput than FCA (particularly for dual-antenna reception) as well as RDCA (for heavy traffic loads). These throughput gains are more significant in uplink than in downlink.

In ad hoc networks, interference management via collision-avoidance medium access schemes results in poor spatial reuse and, thus, restricts network throughput. To address this shortcoming, two physical-medium-access-control cross-layer protocols are proposed. The first increases spatial reuse by integrating medium access, power control, and optimum receive beamforming in a distributed manner, and it is named progressive back-off algorithm with optimum receive beamforming (PBOA-ORB). The second additionally incorporates transmit beamforming, on the premise of centralized control, and it is named progressive back-off algorithm with transmit and optimum receive beamforming (PBOA-TORB). The performance of both protocols is evaluated in terms of aggregate throughput and energy efficiency via simulations over a single-hop network. It is shown that the throughput of PBOA-ORB increases linearly with the number of antennas per node thanks to interference suppression provided by optimum receive beamforming. PBOA-TORB achieves only an incremental throughput gain over PBOA-ORB despite its centralized nature. However, it is significantly more energy efficient than PBOA-ORB thanks to extra array gain provided by transmit beamforming.

1 Introduction

Wireless communication is inherently subject to interference as a consequence of the broadcast nature of the wireless channel. This problem is especially acute in multiuser networks where transmissions are mainly interference-limited rather than noise-limited. In such networks, interference management is necessary to ensure efficient spectrum utilization and acceptable quality of service.

In this dissertation, novel schemes are proposed to control interference and, ultimately, increase throughput in two different multiuser wireless network paradigms, namely, time-division duplexing (TDD)/code-division multiple-access (CDMA) cellular and ad hoc. In TDD/CDMA cellular networks with asymmetric data traffic, dynamic channel allocation enhances resource utilization but, at the same time, incurs excess intercell interference which can severely degrade network throughput. In ad hoc networks, medium access protocols based on collision avoidance limit interference inefficiently around the receivers at the expense of spatial reuse. The schemes proposed in this dissertation address both problems effectively by exploiting the availability of multiple antennas at the wireless nodes as well as combining interference management mechanisms from both the physical (PHY) and medium access control (MAC) layers.

Section 1.1 provides the background on the two aforementioned problems and motivates the development of the proposed schemes, while Section 1.2 summarizes the contributions of the dissertation.

1.1 Background

1.1.1 TDD/CDMA Cellular Networks

Recently, the wireless communications industry has witnessed an ever-increasing demand for data services (e.g., Internet access) over mobile cellular networks. Unlike
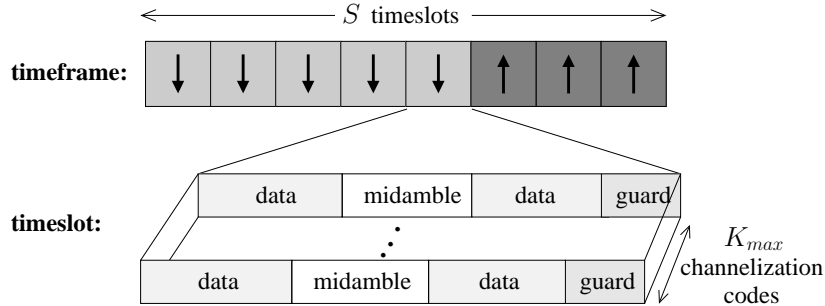
Figure 1.1: Timeframe and timeslot structure in TDD/CDMA.

voice traffic, data traffic is *asymmetric* in terms of the downlink (DL) and uplink (UL) bandwidth it requires. The downlink traffic volume typically exceeds the uplink traffic volume [13]; however, the exact level of asymmetry between the two is time varying, depending on the specific application (e.g., multimedia streaming, peer-to-peer networking, etc.). Under these conditions, time-division duplexing is preferable to frequency-division duplexing (FDD) since it enables flexible allocation of timeslots to downlink and uplink rather than divide the available bandwidth evenly among the two links. Hence, in addition to the FDD mode, the third-generation Universal Mobile Telecommunications System (UMTS) Terrestrial Radio Access (UTRA) standard provides a TDD mode to support high-speed asymmetric data services in microcell and picocell environments [17].

The UTRA TDD mode is based on TDD/CDMA, a hybrid multiple access scheme that allows for multiple short channelization codes per timeslot (see Fig. 1.1). In a TDD/CDMA cellular network, different cells generally experience different degrees of traffic asymmetry. To maximize resource utilization, dynamic channel allocation (DCA) should be employed on a cell basis in accordance to local downlink and uplink traffic requirements, thus, resulting in different timeslot assignments across the cells of a timeframe-synchronous network [21]. In this way, it is possible that the same timeslot is assigned to downlink in one cell and to uplink in an adjacent cell, as shown in Fig. 1.2 for cells A and B. Such a timeslot is referred to as *crossed* timeslot. Since downlink and uplink share the same frequency band, which is reused in every cell for increased spectral efficiency, intercell interference occurs between the transmitting base station of cell A and the receiving base station of cell B as well as between the transmitting mobile station(s) in cell B and the receiving one(s) in cell A. This is known as *crossed-slot* (or *same-entity*) *interference* of base-to-base (BS-to-BS) or mobile-to-mobile (MS-to-MS)
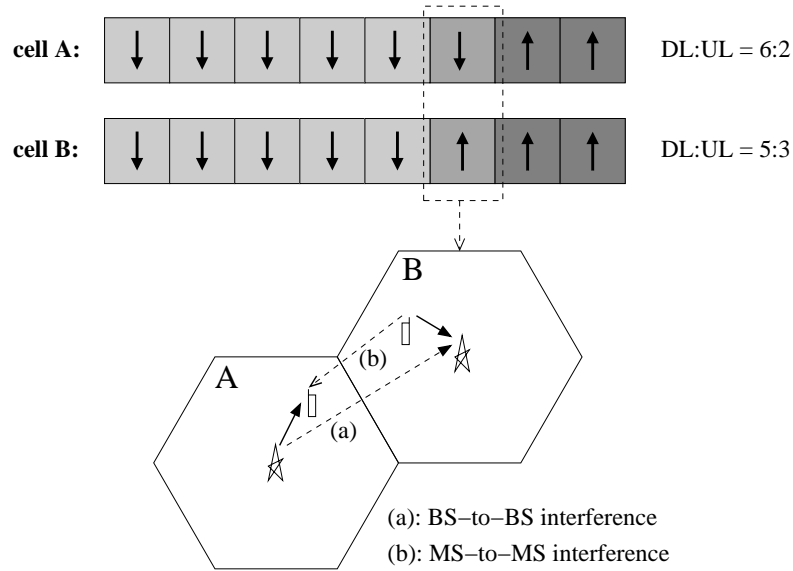
Figure 1.2: Crossed-slot interference in a TDD/CDMA network of two cells that have different downlink-to-uplink traffic ratios and employ dynamic channel allocation.

type, respectively [21], [18].

Crossed-slot interference can be worse than conventional intercell interference between base and mobile stations, significantly impairing the system capacity [19]. In uplink, BS-to-BS interference typically exceeds MS-to-BS interference since BS-BS links experience milder scattering than MS-BS links due to the elevation of base stations relative to mobile stations. Moreover, in downlink, strong MS-to-MS interference is induced to a receiving mobile station by an adjacent-cell transmitting mobile station when both are close to the common boundary of their cells. As a simple remedy, fixed channel allocation (FCA) could be adopted, resulting in identical timeslot assignments across cells. This would eliminate crossed-slot interference, albeit at the expense of wasted resources due to mismatch between downlink-versus-uplink generated traffic and assigned bandwidth in a cell. Clearly, a tradeoff between efficient resource utilization and excess intercell interference occurs in a TDD/CDMA cellular network with asymmetric traffic, and it is of interest to devise schemes that achieve enhanced throughput compared to FCA.

Considerable research effort has been devoted to mitigating crossed-slot interference at the radio resource control layer or at the physical layer via signal processing and antenna-based techniques. In [18], a centralized DCA algorithm was developed to increase the capacity of a TDD/CDMA network by coordinating timeslot allocation across

cells. A genetic algorithm approach was followed by Ni and Hanzo [30] to achieve the same goal. In [47], the uplink capacity was shown to greatly improve by adopting centralized base station signal processing for intercell interference cancellation within a cell cluster. In [10], receive and transmit beamforming were employed at the base stations of a TDD/CDMA network to suppress BS-to-BS interference, while in [22], the use of switched-beam antennas at the base stations was combined with beam-aware timeslot allocation to avoid BS-to-BS interference. In [50], Wang *et al.* proposed a trisector cellular architecture along with DCA on the basis of 'virtual' cells, formed by triplets of adjacent cell sectors, as a solution to the crossed-slot interference problem.

The above works present two limitations. First, those that rely on coordinated channel allocation or centralized processing (e.g., [18], [30], and [47]) require network-wide channel state information (CSI), which is hard to obtain in practical systems, and entail a significant complexity and signaling overhead. Second, those that rely on directional antenna beam patterns (e.g., [10] and [22]) assume line-of-sight (LOS) channel models that account for propagation loss and shadowing but ignore multipath fading. In rich scattering environments, multipath fading destroys the directionality of signals due to angular selectivity and, thus, inhibits the applicability of these works to cellular network scenarios of interest (e.g., urban microcell or picocell). These limitations provide the motivation behind the scheme proposed in Chapter 2 of the dissertation.

1.1.2 Ad Hoc Networks

Ad hoc networks are self-configurable sets of nodes that communicate, directly or by relaying, over the wireless medium with no need for centralized control. These properties make them suitable for communication scenarios where the deployment of a fixed infrastructure is expensive or impractical (e.g., tactical and disaster relief operations, nomadic networking, etc.) and, at the same time, pose significant challenges to their design and operation.

A fundamental challenge in the design of the MAC layer for ad hoc networks arises from the need to limit interference at the receivers while keeping the density of parallel transmissions (i.e., the spatial reuse) high. MAC protocols based on carrier sensing and collision avoidance, such as the carrier-sense multiple access with collision avoidance (CSMA/CA) protocol used in the IEEE 802.11 standard, limit interference by reserving the channel around a transmitter-receiver pair via a request-to-send (RTS)/clear-to-send

(CTS) handshake prior to data transmission. However, they suffer from poor spatial reuse and unresolved collisions, which severely restrict network throughput [3]. Several research efforts have sought to address these shortcomings, often replacing the collision model with a more accurate signal-to-interference-plus-noise ratio (SINR) threshold model. Such efforts include the CDMA-based protocol of [28] and the progressive back-off algorithm (PBOA) of [45], which incorporate power control into medium access so that mutually interfering transmissions take place simultaneously in the vicinity of a receiver. In so doing, these protocols achieve higher throughput than CSMA/CA and also reduce the energy consumption per data packet delivered.

Multiple-antenna or multiple-input-multiple-output (MIMO) techniques offer a great potential for enhancing the throughput of ad hoc networks [9], given that the latter often operate in rich scattering environments. Although *space-time coding* schemes considerably improve the reliability of individual links [42], [43], [44], it is the *spatial multiplexing* and *beamforming* schemes (e.g., [15], [53], and [8]) that are more likely to have a greater impact on network throughput by increasing spatial reuse. Upgrading the physical layer with multiple-antenna techniques while keeping the MAC layer unchanged certainly benefits the network performance [40], [20]. However, significant gains are expected from the joint design of the two layers [55]. This PHY-MAC cross-layer design in multiple-antenna ad hoc networks is a topic that has recently started being addressed, with most existing works (e.g., [31], [5], and [6]) considering the use of spatial multiplexing.

1.2 Dissertation Overview

In Chapter 2, a novel scheme is proposed that mitigates crossed-slot intercell interference in TDD/CDMA networks, in a way that dispenses with the limitations of previous proposals described in Section 1.1.1. The proposed scheme combines an interference-aware DCA (IADCA) algorithm with space-time linear minimum-mean-square-error (LMMSE) joint detection in downlink and uplink, assuming antenna-array-equipped mobile and base stations. The IADCA algorithm is *independently* executed in each cell, and it assigns active MS-BS links to timeslots according to their path loss so that crossed-slot interference is reduced. Path-loss-based DCA has been previously reported in [25], [52], [29], and [32]. However, the proposed scheme is novel compared with these works in that 1) it requires no coordination among cells; and 2) it complements the

IADCA algorithm with space-time LMMSE joint detection to cope with residual crossed-slot interference. Thus, space-time LMMSE joint detection is considered, herein, not only for intersymbol interference (ISI) and intracell multiple access interference (MAI) mitigation, as in [24], but also for intercell interference suppression. The latter is achieved by exploiting the knowledge of the intercell interference spatio-temporal autocorrelation statistics, which is locally acquired at the receivers (e.g., via training sequences on a timeslot basis). This approach is, essentially, the multiple-antenna extension of the 'unstructured-interference' LMMSE joint detection of [7] and is named *space-time LMMSE joint detection for colored intercell interference (LMMSE-CI)*.

The link-level and system-level performances of the proposed scheme are characterized in terms of SINR outage and average throughput, respectively, and are compared with those of benchmark random DCA (RDCA) and FCA schemes. Both performance metrics are evaluated by means of analytical approximations and Monte Carlo simulations for perfect and imperfect receiver CSI in downlink and uplink.

In Chapter 3, two PHY-MAC cross-layer protocols for multiple-antenna ad hoc networks are proposed with the goal of enhancing network throughput in an energy efficient manner. The first protocol extends the PBOA protocol of [45] by integrating medium access and power control with optimum receive beamforming, hence it is named *progressive back-off algorithm with optimum receive beamforming (PBOA-ORB)*. The protocol is novel since optimum receive beamforming and power control have not yet been jointly considered in ad hoc networks (even though they have been shown to improve the capacity and energy efficiency of cellular networks [36]). Similarly to PBOA, time is divided in frames that consist of a contention slot and a data slot. Nodes with a data packet contend for channel access during the contention slot, and those that 'win' transmit their packet in the data slot. Assuming that channel variations are negligible over the frame duration, PBOA-ORB determines, in a distributed fashion, 1) a subset of contending nodes that will successfully deliver their packet to its destination, once they simultaneously transmit in the data slot; 2) their transmit power levels; and 3) the beamforming weights at the receiving nodes. The size of this subset is increased by exploiting the interference suppression capability of optimum receive beamforming. Therefore, higher spatial reuse than PBOA is achieved.

The second protocol dispenses with the assumption of single-antenna transmission underlying in PBOA-ORB and incorporates transmit beamforming into its con-

tention resolution mechanism. Hence, it is named *progressive back-off algorithm with transmit and optimum receive beamforming (PBOA-TORB)*. Adjusting the transmit beamforming weights appropriately offers extra degrees of freedom that can be used to further increase the number of successfully contending nodes in each frame. This adjustment is performed on the basis of the network duality theorem of [38], which requires network-wide channel state information. Consequently, unlike PBOA-ORB, PBOA-TORB is a centralized protocol. As such, it provides an upper bound on the performance of (potentially distributed) protocols that integrate transmit and receive beamforming with the medium access and power control mechanisms of PBOA.

The performance of the two proposed protocols is evaluated in terms of through-put and energy consumption via simulations over a single-hop ad hoc network that is subject to a uniform traffic load. Various numbers of antennas per node are consid-ered. Comparison with PBOA is straightforward since PBOA-ORB coincides with this protocol in the case of single-antenna nodes.

Finally, Chapter 4 summarizes the main conclusions of the dissertation and presents future research ideas.

2 Cross-slot Interference Mitigation in TDD/CDMA Cellular Networks

As mentioned in Section 1.1.1, base-to-base and mobile-to-mobile crossed-slot intercell interference arises in TDD/CDMA cellular networks with asymmetric data traffic when dynamic channel allocation is employed to enhance resource utilization. In this chapter, a decentralized scheme that mitigates crossed-slot intercell interference and, at the same time, ensures efficient resource utilization is proposed. This scheme combines an IADCA algorithm with space-time LMMSE joint detection at the receivers. The former avoids crossed-slot interference in channel allocation. The latter suppresses the remaining intercell interference by modeling it as colored noise with known spatio-temporal autocorrelation (LMMSE-CI joint detection) rather than as white noise (LMMSE-WI joint detection).

This chapter is organized as follows. In Section 2.1, the system model is introduced. Section 2.2 describes the space-time LMMSE joint detection and a practical CSI estimation scheme. Analytical expressions for the SINR and the bit error probability that characterize a reference timeslot are also derived. In Section 2.3, the proposed IADCA algorithm and the RDCA and FCA benchmark algorithms are presented. Section 2.4 defines the metrics used in performance evaluation, and, finally, Section 2.5 discusses the simulation methodology and results.
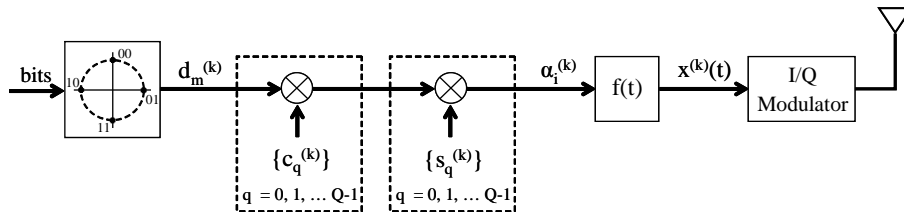
Figure 2.1: Transmitter block diagram for the kth intracell packet in a reference timeslot.

2.1 System Model

An unsectored TDD/CDMA cellular network that consists of a reference cell and the first tier of interferers around it (i.e., seven hexagonal cells in total) is considered. The mobile stations in each cell are served by a base station located in the cell center and both types of stations are equipped with arrays of omnidirectional antennas. Single-antenna transmission and multiple-antenna reception are employed in both downlink and uplink. The network is assumed timeframe synchronous (but not necessarily chip synchronous), and a timeframe is divided into S timeslots, each one supporting up to $K_{\max}$ CDMA channelization codes, as illustrated in Fig. 1.1. Hence, $K_{\max}S$ timeslot-code physical channels are available for transmission. Communication links between the mobile stations and the base station of a cell are assumed to carry downlink and uplink data packet streams in the fashion of [11]. At the beginning of every timeframe, a channel allocation algorithm, which is executed at each base station, allocates timeslots to downlink and uplink, determines the number of generated packets that are admitted to the system per MS-BS link, and assigns each admitted packet to a timeslot-code channel, as described in Section 2.3. Once the channel allocation decisions are made and communicated to the mobile stations (e.g., via a broadcast control channel), packet transmission takes place.

2.1.1 Transmit Signal Model

Fig. 2.1 depicts the transmitter block diagram that corresponds to a packet, which is indexed by k and is assigned to channelization code $\boldsymbol{c}^{(k)} = \left[c_0^{(k)}, \ldots, c_{Q-1}^{(k)}\right]^T$ in a reference timeslot. Orthogonal variable spreading factor (OVSF) codes are employed in UTRA TDD [17] and, for simplicity, only codes with spreading factor Q are considered herein. The mth data symbol $d_m^{(k)}$ of the kth packet, which is drawn from a unit-energy QPSK constellation, is spread by $\boldsymbol{c}^{(k)}$, and the resulting chips are scrambled by a cell-

specific scrambling code $\boldsymbol{s}^{(k)} = \left[s_0^{(k)}, \ldots, s_{Q-1}^{(k)}\right]^T$ for the purpose of intercell interference reduction [1]. Thus, the data symbol sequence of the packet $\left\{d_m^{(k)}, \ m = 0, \ldots, M-1\right\}$ is mapped to the chip sequence $\left\{a_i^{(k)}, \ i = 0, \ldots, MQ-1\right\}$, and the mth symbol chips are represented by the vector

$$\boldsymbol{a}^{(k)}(m) = \left[a_{mQ}^{(k)}, \ldots, a_{(m+1)Q-1}^{(k)}\right]^T = \boldsymbol{c_s}^{(k)} d_m^{(k)}$$

where

$$\boldsymbol{c_s}^{(k)} = \left[c_0^{(k)} s_0^{(k)}, \ldots, c_{Q-1}^{(k)} s_{Q-1}^{(k)}\right]^T \tag{2.1}$$

is the element-by-element product of $\boldsymbol{c}^{(k)}$ and $\boldsymbol{s}^{(k)}$. Prior to in-phase/quadrature (I/Q) modulation, the chips are fed into a chip-pulse shaping filter with impulse response $f(t)$, which is selected so that its energy autocorrelation function $\psi(t) = f(t) \star f^*(-t)$ is a Nyquist pulse. Typically, a truncated root-raised-cosine (RRC) chip pulse with roll-off factor β and bandwidth $B \approx (1+\beta)/2T_c$ is used [34], where T_c denotes the chip period. The baseband equivalent transmit signal corresponding to the kth packet is then given by

$$x^{(k)}(t) = e^{j\theta_k} \sqrt{P_T^{(k)} T_c} \sum_{i=0}^{MQ-1} a_i^{(k)} f(t - iT_c) \tag{2.2}$$

where $e^{j\theta_k}$ captures the carrier phase offset between the transmitter and the receiver, and $P_T^{(k)}$ denotes the transmit power.

In both downlink and uplink, the transmit power is adjusted by a simple power control scheme so that *path loss* is compensated for and a target average power level $P_{R,\text{trgt}}$ is guaranteed at the intended receiver. Herein, path loss refers to the combination of propagation loss and shadowing and is assumed to be known at the transmitter of a link. In practice, this can be achieved by means of a beacon signal broadcasted by the base station in a control channel (e.g., the P-CCPCH channel in UTRA TDD [17]). The beacon transmit power is fixed and *a priori* known to the mobile stations, which measure the average received beacon power, calculate the downlink path loss, and feed its value back to the base station. By exploiting the channel reciprocity due to the TDD component, the same path loss value is used in uplink power control.

2.1.2 Received Signal Model

Fig. 2.2 shows the baseband system model for a reference cell of the TDD/CDMA network under study, during a downlink or uplink timeslot. In downlink, a mobile
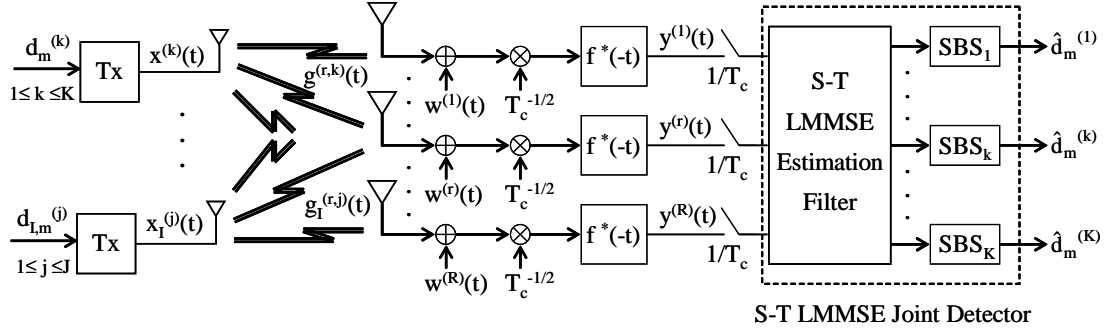
Figure 2.2: Baseband system model in the reference cell of a TDD/CDMA network during a downlink or uplink timeslot.

station in the reference cell receives the packets transmitted by its base station (indexed by k, $1 \leq k \leq K \leq K_{\max}$), as well as those transmitted by interfering intercell base or mobile stations (indexed by j, $1 \leq j \leq J$). In uplink, the base station of the reference cell receives the packets transmitted by intracell mobile stations (indexed by k, $1 \leq k \leq K \leq K_{\max}$), as well as those transmitted by interfering intercell mobile or base stations (indexed by j, $1 \leq j \leq J$).

The channel impulse response between the transmitter of the kth packet and the rth receive antenna is modeled as[1]

$$g^{(r,k)}(t) = \sqrt{\frac{\zeta^{(k)}}{\eta^{(k)}}} \sum_{n=1}^{N} g_n^{(r,k)} \delta(t - \tau_n^{(k)}) \tag{2.3}$$

assuming that the channel is time invariant over the duration of a timeslot. This assumption is fairly realistic in the low mobility scenarios (e.g., pedestrian outdoor or indoor environment) that UTRA TDD is designed for [17]. In the above expression, $\eta^{(k)}$ represents the distance-dependent propagation loss and $\zeta^{(k)}$ the lognormal shadowing between the kth packet transmitter and the receiver. In addition, N is the maximum number of paths, while $g_n^{(r,k)}$ and $\tau_n^{(k)}$ denote, respectively, the nth path fading coefficient and the nth path delay, which also accounts for imperfect user synchronization. In the following analysis, it is convenient to consider the *effective* channel impulse response

$$h^{(r,k)}(t) = e^{j\theta_k} \sqrt{P_T^{(k)}} \, g^{(r,k)}(t) \star f(t) \star f^*(-t) \tag{2.4}$$

which incorporates chip-pulse shaping, multipath channel propagation, and receiver chip-matched filtering. If $\tau_{\max}$ is the maximum path delay experienced by a user in the system

---

[1]Obviously, if packets k_1 and k_2 share a common transmitter (e.g., the base station in downlink), then $g^{(r,k_1)}(t) \equiv g^{(r,k_2)}(t)$.

and $\psi(t) = f(t) \star f^*(-t)$ is causal with finite time duration equal to DT_c, for some $D \in \mathbb{N}$, then $h^{(r,k)}(t)$ is nonzero in $\left[0, DT_c + \tau_{\max}\right)$.

The expression for the baseband equivalent signal at the rth receive antenna, after chip-matched filtering, is

$$y^{(r)}(t) = \sum_{k=1}^{K} \sum_{i=0}^{MQ-1} a_i^{(k)} h^{(r,k)}(t - iT_c) + \underbrace{\sum_{j=1}^{J} \sum_{i=0}^{MQ-1} a_{I,i}^{(j)} h_I^{(r,j)}(t - iT_c) + \tilde{w}^{(r)}(t)}_{n^{(r)}(t)} \qquad (2.5)$$

where the last two terms, corresponding to intercell interference plus thermal noise, are incorporated in $n^{(r)}(t)$. Subscript I indicates a variable associated with intercell packets, and $\tilde{w}^{(r)}(t)$ represents the rth antenna matched filter output due to front-end additive white Gaussian noise (AWGN) $w^{(r)}(t)$ with power spectral density $S_{\tilde{w}^{(r)}}(\omega) = (N_o/T_c)\Psi(\omega)$, where $\Psi(\omega)$ is the Fourier transform of $\psi(t)$. The discrete-time equivalent of (2.5), after sampling at the chip-rate $1/T_c$, is

$$y_i^{(r)} = \sum_{k=1}^{K} \sum_{p=0}^{P-1} h_p^{(r,k)} a_{i-p}^{(k)} + n_i^{(r)} \qquad (2.6)$$

with $y_i^{(r)} = y^{(r)}(iT_c)$, $h_p^{(r,k)} = h^{(r,k)}(pT_c)$, $n_i^{(r)} = n^{(r)}(iT_c)$, and $P = D + \lceil \tau_{\max}/T_c \rceil$, denoting the number of nonzero effective channel impulse response samples. The vector $\boldsymbol{y}^{(r)}(m) = \left[y_{mQ}^{(r)}, \ldots, y_{(m+1)Q+P-2}^{(r)}\right]^T$ of the rth antenna received signal samples that carry *all* the energy due to the mth data symbols of the intracell packets is, thus, given by

$$\boldsymbol{y}^{(r)}(m) = \sum_{k=1}^{K} \boldsymbol{H}^{(r,k)} \tilde{\boldsymbol{a}}^{(k)}(m) + \boldsymbol{n}^{(r)}(m) \qquad (2.7)$$

where $\boldsymbol{n}^{(r)}(m) = \left[n_{mQ}^{(r)}, \ldots, n_{(m+1)Q+P-2}^{(r)}\right]^T$, $\boldsymbol{H}^{(r,k)} \in \mathbb{C}^{(Q+P-1)\times(Q+2P-2)}$ is a Toeplitz matrix with $H_{i,j}^{(r,k)} = h_{P-1-j+i}^{(r,k)}$, and $\tilde{\boldsymbol{a}}^{(k)}(m)$ is the vector of the kth packet chips contributing to $\boldsymbol{y}^{(r)}(m)$. These include not only the chips of the mth data symbol, but also chips of previous and subsequent data symbols, as a consequence of ISI caused by multipath propagation.

Writing the effective channel impulse response length as $P-1 = uQ+q$, for some $u \in \mathbb{N}$ and $q \in \{0, 1, \ldots, Q-1\}$, it is easy to verify that $\tilde{\boldsymbol{a}}^{(k)}(m)$ contains chips due to $U = 1 + 2\lceil (P-1)/Q \rceil$ symbols in total. Specifically, it contains all Q chips of symbols $\{d_{m-u}^{(k)}, \ldots, d_m^{(k)}, \ldots, d_{m+u}^{(k)}\}$, as well as the last q chips of symbol $d_{m-u-1}^{(k)}$ and the first q chips of symbol $d_{m+u+1}^{(k)}$. Therefore, it can be expressed as

$$\tilde{\boldsymbol{a}}^{(k)}(m) = \boldsymbol{C}_s^{(k)} \boldsymbol{d}^{(k)}(m) \qquad (2.8)$$

where
$$\boldsymbol{d}^{(k)}(m) = \left[d_{m-u-1}^{(k)}, d_{m-u}^{(k)}, \ldots, d_m^{(k)}, \ldots, d_{m+u}^{(k)}, d_{m+u+1}^{(k)} \right]^T$$

and $\boldsymbol{C_s}^{(k)}$ is the block diagonal matrix

$$\boldsymbol{C_s}^{(k)} = \begin{bmatrix} \boldsymbol{c}_{s,q-}^{(k)} & \boldsymbol{0} & \cdots & \boldsymbol{0} & \cdots & \boldsymbol{0} & \boldsymbol{0} \\ \boldsymbol{0} & \boldsymbol{c_s}^{(k)} & \cdots & \boldsymbol{0} & \cdots & \boldsymbol{0} & \boldsymbol{0} \\ \vdots & \vdots & \ddots & \vdots & \vdots & \vdots & \vdots \\ \boldsymbol{0} & \boldsymbol{0} & \cdots & \boldsymbol{c_s}^{(k)} & \cdots & \boldsymbol{0} & \boldsymbol{0} \\ \vdots & \vdots & \vdots & \vdots & \ddots & \vdots & \vdots \\ \boldsymbol{0} & \boldsymbol{0} & \cdots & \boldsymbol{0} & \cdots & \boldsymbol{c_s}^{(k)} & \boldsymbol{0} \\ \boldsymbol{0} & \boldsymbol{0} & \cdots & \boldsymbol{0} & \cdots & \boldsymbol{0} & \boldsymbol{c}_{s,q+}^{(k)} \end{bmatrix}$$

with $\boldsymbol{c}_{s,q-}^{(k)} = \left[c_{Q-q}^{(k)} s_{Q-q}^{(k)}, \ldots, c_{Q-1}^{(k)} s_{Q-1}^{(k)} \right]^T$, $\boldsymbol{c}_{s,q+}^{(k)} = \left[c_0^{(k)} s_0^{(k)}, \ldots, c_{q-1}^{(k)} s_{q-1}^{(k)} \right]^T$, and $\boldsymbol{c_s}^{(k)}$ given by (2.1). Due to (2.8), (2.7) is written as

$$\boldsymbol{y}^{(r)}(m) = \sum_{k=1}^{K} \boldsymbol{A}^{(r,k)} \boldsymbol{d}^{(k)}(m) + \boldsymbol{n}^{(r)}(m) \tag{2.9}$$

for

$$\boldsymbol{A}^{(r,k)} = \boldsymbol{H}^{(r,k)} \boldsymbol{C_s}^{(k)}. \tag{2.10}$$

Finally, stacking the samples from all R receive antennas in the composite vector $\boldsymbol{y}(m) = \left[\boldsymbol{y}^{(1)T}(m), \ldots, \boldsymbol{y}^{(R)T}(m) \right]^T$ results in the received signal vector model

$$\boldsymbol{y}(m) = \boldsymbol{A}\boldsymbol{d}(m) + \boldsymbol{n}(m) \tag{2.11}$$

where $\boldsymbol{d}(m) = \left[\boldsymbol{d}^{(1)T}(m), \ldots, \boldsymbol{d}^{(K)T}(m) \right]^T$, $\boldsymbol{n}(m) = \left[\boldsymbol{n}^{(1)T}(m), \ldots, \boldsymbol{n}^{(R)T}(m) \right]^T$, and $\boldsymbol{A}$ is a block matrix that has $\boldsymbol{A}^{(r,k)}$ as its rkth block, for $r = 1, \ldots, R$ and $k = 1, \ldots, K$.

In the above model, $\boldsymbol{A}$ depends on the scrambling and channelization codes of the intracell packets, as well as the corresponding channel coefficients, and captures the effects of ISI and intracell MAI. Since the channels have been assumed to be time invariant during a timeslot, $\boldsymbol{A}$ is independent of the data symbol index m. Intercell interference and thermal noise are captured by the zero-mean random vector $\boldsymbol{n}(m)$, whose autocorrelation matrix $\boldsymbol{R_n} = E\left\{ \boldsymbol{n}(m)\boldsymbol{n}^H(m) \right\}$ is shown, in Appendix A, to be a

block matrix with $r\rho$th block given by[2]

$$\boldsymbol{R_n^{(r,\rho)}} = \sum_{j=1}^{J} \boldsymbol{H}_I^{(r,j)} \boldsymbol{H}_I^{(\rho,j)H} + \frac{N_o}{T_c} \delta_{r,\rho} \boldsymbol{I} \qquad (2.12)$$

for $r, \rho = 1, \ldots, R$.

2.2 Space-Time Processing

2.2.1 Space-Time LMMSE Joint Detection

In order to detect the data symbols of the desired intracell packet(s) at the receiver, a linear detector is employed. It performs joint equalization and multiuser detection by linearly combining the matched filter samples from all the receive antennas (see Fig. 2.2) so that the mean square error between its output and the desired data symbols is minimized. Therefore, not only temporal but also spatial degrees of freedom are utilized in combatting ISI and intracell MAI, further enhancing the receiver performance. This space-time LMMSE joint detector[3] is used in both downlink and uplink, and it requires that the parameters of the received signal model of (2.11) are known at the receiver. Equivalently, it is required that 1) the scrambling and spreading codes of all the intracell packets, and 2) the intracell channel coefficients and intercell-intreference-plus-noise statistics are known at the receiver. The first requirement is directly satisfied in uplink and can also be satisfied in downlink, provided that the base station broadcasts the indices of the codes used in each timeslot to the mobile stations in its cell. The second requirement is practically achieved via joint channel estimation by means of midamble training sequences, as discussed in Section 2.2.2.

Regarding the treatment of intercell interference, two variants of the space-time LMMSE joint detector are considered. The first explicitly suppresses intercell interference on the basis of the intercell-interference-plus-noise spatio-temporal autocorrelation matrix $\boldsymbol{R_n}$, which is assumed to be known (or estimated) at the receiver. This variant is referred to as *space-time LMMSE joint detector for colored intercell interference (LMMSE-CI)* and is favored in our scheme. The second treats intercell interference as

---

[2]Equation (12) suggests that information from adjacent cells (e.g., the number of intercell interferers) is needed to evaluate $\boldsymbol{R_n}$. However, in practice, $\boldsymbol{R_n}$ is locally estimated at the receivers via midamble training sequences, as described in Section 2.2.2.

[3]In the absence of ISI, the space-time LMMSE joint detector reduces to a bank of optimum combiners (in the maximum SINR sense), each one of which is matched to an intracell packet. In the additional absence of MAI, it reduces to a single-user maximal ratio combiner.

spatially and temporally white noise, assuming that only the intercell-interference-plus-noise average power $\sigma_{\boldsymbol{n}}^2$ is known (or estimated) at the receiver. This variant is referred to as *space-time LMMSE joint detector for white intercell interference (LMMSE-WI)* and is used only as a benchmark.

Since TDD/CDMA transmission is organized in timeslots, it seems natural for the LMMSE joint detector to simultaneously process *all* the received signal samples during a timeslot to estimate the data symbols of the desired packet(s). However, the computational complexity incurred by this *block* implementation is prohibitive for typical packet lengths and spreading code factors. Hence, the more practical *sliding processing window* implementation [7] is adopted for a window length of $Q + P - 1$ chips per receive antenna. At the mth detection step, the processing window contains the received signal samples $\boldsymbol{y}(m)$ carrying all the energy due to the mth data symbols of the intracell packets. Soft estimates of these symbols are first produced by feeding the window samples into an LMMSE estimation filter and are, subsequently, transformed into hard symbol decisions via a bank of symbol-by-symbol (SBS) detectors: one per desired packet. The whole process is repeated, sliding the processing window by Q chips so that it contains the received signal samples $\boldsymbol{y}(m + 1)$ due to the $(m + 1)$th data symbols, and so on.

LMMSE filtering performs the well-known optimization

$$\boldsymbol{W}_{\text{LMMSE}} = \underset{\boldsymbol{W}}{\operatorname{argmin}}\, E\left\{|\boldsymbol{W}\boldsymbol{y}(m) - \boldsymbol{d}(m)|^2\right\} \qquad (2.13)$$

which, for independent identically distributed (i.i.d.) and unit-energy data symbols, leads to the expressions

$$\boldsymbol{W}_{\text{LMMSE−CI}} = \hat{\boldsymbol{A}}^H \left(\hat{\boldsymbol{A}}\hat{\boldsymbol{A}}^H + \hat{\boldsymbol{R}}_{\boldsymbol{n}}\right)^{-1} \qquad (2.14)$$

$$\boldsymbol{W}_{\text{LMMSE−WI}} = \hat{\boldsymbol{A}}^H \left(\hat{\boldsymbol{A}}\hat{\boldsymbol{A}}^H + \hat{\sigma}_{\boldsymbol{n}}^2 \boldsymbol{I}\right)^{-1} \qquad (2.15)$$

for LMMSE-CI and LMMSE-WI, respectively, which are independent of the symbol index m. Here, $\hat{\boldsymbol{A}}$, $\hat{\boldsymbol{R}}_{\boldsymbol{n}}$, and $\hat{\sigma}_{\boldsymbol{n}}^2$ denote the estimates of $\boldsymbol{A}$, $\boldsymbol{R}_{\boldsymbol{n}}$, and $\sigma_{\boldsymbol{n}}^2$, which are typically available at the receiver instead of the actual parameters themselves. In practice, Cholesky factorization can be used to reduce the computational complexity due to matrix inversion in the above expressions [49]. The output of either LMMSE filter is written as

$$\boldsymbol{z}(m) = \boldsymbol{W}\boldsymbol{y}(m) = \boldsymbol{G}\boldsymbol{d}(m) + \tilde{\boldsymbol{n}}(m) \qquad (2.16)$$

for $\boldsymbol{W} = \boldsymbol{W}_{\text{LMMSE}-\text{CI}}$ or $\boldsymbol{W}_{\text{LMMSE}-\text{WI}}$, $\boldsymbol{G} = \boldsymbol{W}\boldsymbol{A}$, and $\tilde{\boldsymbol{n}}(m) = \boldsymbol{W}\boldsymbol{n}(m)$ with autocorrelation matrix $\boldsymbol{R}_{\tilde{\boldsymbol{n}}} = \boldsymbol{W}\boldsymbol{R}_{\boldsymbol{n}}\boldsymbol{W}^H$. As a result, the LMMSE soft estimate that corresponds to the mth data symbol $d_m^{(k)}$ of the kth packet is given by the vth element of $\boldsymbol{z}(m)$, i.e.,

$$z_m^{(k)} = z_v(m) = G_{v,v}d_m^{(k)} + \underbrace{\sum_{\substack{i=1 \\ i \neq v}}^{KU} G_{v,i}d_i(m) + \tilde{n}_v(m)}_{\xi_v(m)} \tag{2.17}$$

where $v = U(k-1) + (U-1)/2 + 1$ is the index of $d_m^{(k)}$ in $\boldsymbol{d}(m)$, and $\xi_v(m)$ denotes the residual ISI, intracell MAI, intercell interference, and noise after LMMSE filtering.

The SINR at the input of the kth packet SBS detector, which produces the hard symbol decision $\hat{d}_m^{(k)}$ from $z_m^{(k)}$, is given by

$$\gamma^{(k)} = \frac{|G_{v,v}|^2}{\displaystyle\sum_{\substack{i=1 \\ i \neq v}}^{KU} |G_{v,i}|^2 + [\boldsymbol{R}_{\tilde{\boldsymbol{n}}}]_{v,v}}. \tag{2.18}$$

Note that, since $\boldsymbol{A}$, $\boldsymbol{W}$, and $\boldsymbol{R}_{\boldsymbol{n}}$ are invariant across different processing window instances during a timeslot, $\gamma^{(k)}$ is independent of the data symbol index m and characterizes the detection quality of the whole kth packet. To derive a closed-form expression for the conditional bit error probability $P_b^{(k)}$ of this packet, the residual interference is approximated by a circularly symmetric complex Gaussian random variable $\xi_v(m) \sim \mathcal{N}_c\big(0, \sum_{i \neq v} |G_{v,i}|^2 + [\boldsymbol{R}_{\tilde{\boldsymbol{n}}}]_{v,v}\big)$, as in [7] and [33]. In this case, it can be shown that

$$P_b^{(k)} = \frac{1}{2}\mathcal{Q}\left(\sqrt{\gamma^{(k)}}(\cos\phi_v - \sin\phi_v)\right) + \frac{1}{2}\mathcal{Q}\left(\sqrt{\gamma^{(k)}}(\cos\phi_v + \sin\phi_v)\right) \tag{2.19}$$

where $\mathcal{Q}(x) = \big(1/\sqrt{2\pi}\big)\int_x^{+\infty} e^{-y^2/2}\,dy$, and $\phi_v = \angle G_{v,v}$, which is the phase of the vvth element of matrix $\boldsymbol{G}$. The Gaussian approximation is intuitively justified as follows. Due to ISI, each packet contributes more than one symbol to residual interference (e.g., six symbols for $P = 34$ and $Q = 16$). Thus, even for a few intracell and intercell interferers, the residual interference sum of (2.17) has enough terms for Central Limit Theorem arguments to apply. The accuracy of this approximation is further investigated by simulations in Section 2.5.4.

Equations (2.14)-(2.19) apply to space-time LMMSE-CI and LMMSE-WI joint detection for both cases of perfect CSI (where the intracell channel coefficients used in the definition of $\boldsymbol{A}$ and the intercell-interference-plus-noise statistics are perfectly known at

the receiver) and imperfect CSI (where they are estimated as described in Section 2.2.2). For example, considering space-time LMMSE-CI joint detection with perfect CSI, it is $\hat{\boldsymbol{A}} = \boldsymbol{A}$ and $\hat{\boldsymbol{R}}_{\boldsymbol{n}} = \boldsymbol{R}_{\boldsymbol{n}}$; therefore, (2.18) and (2.19) are further simplified as

$$\gamma_{\text{LMMSE--CI}}^{(k)} = \frac{1}{\left[\left(\boldsymbol{I} + \boldsymbol{A}^H \boldsymbol{R}_{\boldsymbol{n}}^{-1} \boldsymbol{A}\right)^{-1}\right]_{v,v}} - 1 \quad \text{and} \quad P_{b,\,\text{LMMSE--CI}}^{(k)} = \mathcal{Q}\left(\sqrt{\gamma_{\text{LMMSE--CI}}^{(k)}}\right)$$

respectively.

2.2.2 Channel State Information Estimation

In a TDD/CDMA system, CSI estimation is performed at each (mobile or base station) receiver, on a timeslot basis, by means of midamble training chip sequences *a priori* known to this receiver [41]. Denoting the training sequence assigned to the kth intracell packet in a downlink or uplink timeslot as $\left\{\mu_i^{(k)},\ i = -P + 1, \ldots, V - 1\right\}$, the rth antenna received midamble samples carrying energy *only* due to training chips are given by

$$y_{t,i}^{(r)} = \sum_{k=1}^{K} \sum_{p=0}^{P-1} h_p^{(r,k)} \mu_{i-p}^{(k)} + \underbrace{\sum_{j=1}^{J} \sum_{p=0}^{P-1} h_{I,p}^{(r,j)} \mu_{I,i-p}^{(j)} + \tilde{w}_{t,i}^{(r)}}_{n_{t,i}^{(r)}} \tag{2.20}$$

for $i = 0, \ldots, V - 1$, where $n_{t,i}^{(r)}$ captures the thermal noise and the interference due to the training sequences of intercell packets. Defining $\boldsymbol{y}_t^{(r)} = \left[y_{t,0}^{(r)}, \ldots, y_{t,V-1}^{(r)}\right]^T$ and $\boldsymbol{n}_t^{(r)} = \left[n_{t,0}^{(r)}, \ldots, n_{t,V-1}^{(r)}\right]^T$, it is

$$\boldsymbol{y}_t^{(r)} = \sum_{k=1}^{K} \boldsymbol{M}^{(k)} \boldsymbol{h}^{(r,k)} + \boldsymbol{n}_t^{(r)} = \boldsymbol{M} \boldsymbol{h}^{(r)} + \boldsymbol{n}_t^{(r)} \tag{2.21}$$

for $r = 1, \ldots, R$. In the above expression, $\boldsymbol{h}^{(r,k)} = \left[h_0^{(r,k)}, \ldots, h_{P-1}^{(r,k)}\right]^T$ is the vector of the effective channel impulse response samples between the kth packet transmitter and the rth receive antenna, $\boldsymbol{M}^{(k)} \in \mathbb{C}^{V \times P}$ is a Toeplitz matrix that corresponds to the kth packet training sequence with $M_{i,j}^{(k)} = \mu_{i-j}^{(k)}$, $\boldsymbol{h}^{(r)} = \left[\boldsymbol{h}^{(r,1)T}, \ldots, \boldsymbol{h}^{(r,K)T}\right]^T$, and $\boldsymbol{M} = \left[\boldsymbol{M}^{(1)} \ldots \boldsymbol{M}^{(K)}\right]$[4]. Stacking the samples from all R receive antennas leads to

$$\boldsymbol{y}_t = \left(\boldsymbol{I}_R \otimes \boldsymbol{M}\right) \boldsymbol{h} + \boldsymbol{n}_t \tag{2.22}$$

---

[4]For ease of notation, $\boldsymbol{h}^{(r)}$ and $\boldsymbol{M}$ have been defined for the special case where each packet belongs to a distinct MS-BS link. In the general case where multiple packets originate from, or are destined to, a single mobile station, $\boldsymbol{h}^{(r)}$ is the composite vector of *only the distinct* effective channel impulse responses $\boldsymbol{h}^{(r,k)}$, and $\boldsymbol{M}$ is defined accordingly.

for $\boldsymbol{y}_t = \left[\boldsymbol{y}_t^{(1)T}, \ldots, \boldsymbol{y}_t^{(R)T}\right]^T$, $\boldsymbol{h} = \left[\boldsymbol{h}^{(1)T}, \ldots, \boldsymbol{h}^{(R)T}\right]^T$, and $\boldsymbol{n}_t = \left[\boldsymbol{n}_t^{(1)T}, \ldots, \boldsymbol{n}_t^{(R)T}\right]^T$. At the receiver, the channel coefficients $\boldsymbol{h}$ and the second-order statistics of $\boldsymbol{n}_t$, which are required for LMMSE joint detection, need to be estimated, given $\boldsymbol{y}_t$. To address the practical need for low computational complexity, the two estimation problems are decoupled. Thus, a standard *least-squares* joint channel estimator is initially employed, followed by a *sample* estimator of the intercell-interference-plus-noise second-order statistics.

The criterion for least-squares joint channel estimation is

$$\hat{\boldsymbol{h}} = \underset{\boldsymbol{h}}{\mathrm{argmin}} \left|\boldsymbol{y}_t - (\boldsymbol{I}_R \otimes \boldsymbol{M})\,\boldsymbol{h}\right|^2 \tag{2.23}$$

resulting in

$$\hat{\boldsymbol{h}}^{(r)} = \left(\boldsymbol{M}^H \boldsymbol{M}\right)^{-1} \boldsymbol{M}^H \boldsymbol{y}_t^{(r)} \tag{2.24}$$

for $r = 1, \ldots, R$. The above estimates are valid under the condition that $\boldsymbol{M} \in \mathbb{C}^{V \times KP}$ has a full column-rank, which is satisfied by appropriately selecting the midamble sequences $\left\{\mu_i^{(k)}, \; k = 1, \ldots, K\right\}$ and the training length V so that $V \geq KP$.

With respect to the estimation of the intercell-interference-plus-noise second-order statistics, two cases are considered, corresponding to the two variants of space-time LMMSE joint detection introduced in Section 2.2.1. In LMMSE-WI joint detection, where intercell interference is modeled as spatio-temporally white, only knowledge of the intercell-interference-plus-noise average power $\sigma_{\boldsymbol{n}}^2$ is necessary. This is approximated by $\sigma_{\boldsymbol{n}_t}^2$, which can be estimated from the received midamble samples as

$$\hat{\sigma_{\boldsymbol{n}_t}^2} = \frac{1}{RV} \sum_{r=1}^{R} \left|\boldsymbol{y}_t^{(r)} - \boldsymbol{M}\hat{\boldsymbol{h}}^{(r)}\right|^2 = \frac{1}{RV} \sum_{r=1}^{R} \left|(\boldsymbol{I}_V - \boldsymbol{M}(\boldsymbol{M}^H\boldsymbol{M})^{-1}\boldsymbol{M}^H)\boldsymbol{y}_t^{(r)}\right|^2. \tag{2.25}$$

In LMMSE-CI joint detection, knowledge of the full intercell-interference-plus-noise autocorrelation matrix $\boldsymbol{R_n}$ is required. The latter is approximated by its midamble counterpart $\boldsymbol{R_{n_t}}$. Previous works, such as [51] and [39], have exploited the properties of specific channel models to express $\boldsymbol{R_{n_t}}$ as the Kronecker product of a spatial and a temporal autocorrelation matrix that are separately estimated. In this chapter, a more general approach is followed by directly employing a sample estimator of $\boldsymbol{R_{n_t}}$. Since a sliding processing window of length $Q + P - 1$ is considered in joint detection, a similar window is used in the formulation of the sample estimator. As a result, it is

$$\hat{\boldsymbol{R}_{\boldsymbol{n}_t}} = \frac{1}{L} \sum_{\ell=0}^{L-1} \hat{\boldsymbol{n}}_t(\ell)\,\hat{\boldsymbol{n}}_t^H(\ell) \tag{2.26}$$

for $\hat{\boldsymbol{n}}_t(\ell) = \left[\hat{\boldsymbol{n}}_t^{(1)T}(\ell), \ldots, \hat{\boldsymbol{n}}_t^{(R)T}(\ell)\right]^T$ and $L = V - Q - P + 2$. Note that

$$\hat{\boldsymbol{n}}_t^{(r)}(\ell) = \boldsymbol{y}_t^{(r)}(\ell) - \sum_{k=1}^{K} \hat{\boldsymbol{H}}^{(r,k)} \boldsymbol{\mu}^{(k)}(\ell) \tag{2.27}$$

is the estimate of the rth antenna intercell-interference-plus-noise vector over the ℓth window slide that is formed by subtracting the reconstructed intracell midamble samples from the received samples $\boldsymbol{y}_t^{(r)}(\ell) = \left[y_{t,\ell}^{(r)}, \ldots, y_{t,\ell+Q+P-2}^{(r)}\right]^T$. In the above expression, $\hat{\boldsymbol{H}}^{(r,k)} \in \mathbb{C}^{(Q+P-1)\times(Q+2P-2)}$ is the Toeplitz matrix that corresponds to the estimated channel coefficients $\hat{h}_p^{(r,k)}$, and $\boldsymbol{\mu}^{(k)}(\ell) = \left[\mu_{\ell-P+1}^{(k)}, \ldots, \mu_{\ell+Q+P-2}^{(k)}\right]^T$ is the vector of the kth packet training sequence chips that contribute to the ℓth window received samples. Due to the matrix inversion in (2.14), $\hat{\boldsymbol{R}}_{\boldsymbol{n}_t}$ needs to be full-rank. A necessary condition for rank$(\hat{\boldsymbol{R}}_{\boldsymbol{n}_t}) = R(Q+P-1)$ is $L \geq R(Q+P-1)$ or, equivalently, $V \geq (R+1)(Q+P-1)-1$, imposing an additional constraint on the training length.

Finally, the choice of training sequences $\{\mu_i^{(k)}, \; k = 1, \ldots, K\}$ is essential to CSI estimation. A criterion typically used in their design is the minimization of the channel estimation mean square error, which is defined as $\epsilon^2 = \mathrm{tr}\left(E\{\boldsymbol{e}\boldsymbol{e}^H\}\right)$ for $\boldsymbol{e} = \boldsymbol{h} - \hat{\boldsymbol{h}}$. Due to (2.24) and (2.22), it is

$$\epsilon^2 = \mathrm{tr}\left(\left(\boldsymbol{I}_R \otimes (\boldsymbol{M}^H\boldsymbol{M})^{-1}\boldsymbol{M}^H\right) \boldsymbol{R}_{\boldsymbol{n}_t} \left(\boldsymbol{I}_R \otimes \boldsymbol{M}(\boldsymbol{M}^H\boldsymbol{M})^{-1}\right)\right) \tag{2.28}$$

and therefore, the $\boldsymbol{M}$ that minimizes ϵ^2 depends on the intercell-interference-plus-noise autocorrelation matrix $\boldsymbol{R}_{\boldsymbol{n}_t}$. Even if $\boldsymbol{R}_{\boldsymbol{n}_t}$ is perfectly known at the receiver, its variation across timeslots implies that the training sequences must be optimized on a timeslot basis, which is impractical. Therefore, the design is relaxed by minimizing (2.28) under the assumption that $\boldsymbol{R}_{\boldsymbol{n}_t} = \sigma_{\boldsymbol{n}_t}^2 \boldsymbol{I}$. In this case, as shown by [4], the optimum $\boldsymbol{M}$ satisfies $\boldsymbol{M}^H\boldsymbol{M} \propto \boldsymbol{I}$, which is achieved by selecting the kth training sequence as

$$\mu_i^{(k)} = \chi_{(i-(k-1)P) \bmod V} \tag{2.29}$$

for $i = -P+1, \ldots, V-1$, where $\{\chi_i, \; i = 0, \ldots, V-1\}$ is a *perfect root-of-unity sequence (PRUS)* of length V [27]. This choice is adopted herein. Defining $\boldsymbol{\chi}(i) = \left[\chi_{i \bmod V}, \ldots, \chi_{(i+V-1) \bmod V}\right]^T$, $\boldsymbol{M}$ is written as

$$\boldsymbol{M} = \left[\boldsymbol{\chi}(V) \, \boldsymbol{\chi}(V-1), \ldots, \boldsymbol{\chi}(V-KP+1)\right]$$

and satisfies $\boldsymbol{M}^H\boldsymbol{M} = V\boldsymbol{I}$ since $\boldsymbol{\chi}(i)^H\boldsymbol{\chi}(j) = V\delta_{i,j}$ by the PRUS definition. Consequently, the expressions for $\hat{\boldsymbol{h}}^{(r)}$ and $\sigma_{\boldsymbol{n}_t}^2$ are further simplified as

$$\hat{\boldsymbol{h}}^{(r)} = \frac{1}{V}\boldsymbol{M}^H\boldsymbol{y}_t^{(r)} \tag{2.30}$$

and

$$\sigma_{\hat{\boldsymbol{n}}_t}^2 = \frac{1}{RV} \sum_{r=1}^{R} \left| \left(\boldsymbol{I}_V - \frac{1}{V} \boldsymbol{M} \boldsymbol{M}^H \right) \boldsymbol{y}_t^{(r)} \right|^2 \tag{2.31}$$

respectively.

2.3 Channel Allocation Algorithms

In this section, the proposed IADCA algorithm and the RDCA and FCA algorithms that are used as benchmarks in its performance evaluation are presented. All three are executed on a timeframe basis at the base station of every cell in the network, independently of other cells. Each algorithm receives as input R_{DL} downlink and R_{UL} uplink packet transmission requests generated by the active MS-BS links in a cell, at the beginning of a timeframe, and performs three basic operations. First, timeslots are allocated to downlink and uplink. Then, out of all packets requesting transmission, a number of packets, at most equal to the number of available timeslot-code physical channels, are granted admission to the system. Contention for these channels is resolved in such a way that the ratio of admitted-to-generated packets (i.e., packet admission ratio) is practically identical for all active MS-BS links. Finally, admitted packets are assigned to physical channels according to algorithm-specific rules, while the rest are blocked from transmission.

2.3.1 Interference-Aware Dynamic Channel Allocation (IADCA)

The steps of the IADCA algorithm are provided in the flow diagram of Fig. 2.3. First, the number of downlink (S_{DL}) and uplink (S_{UL}) timeslots in a timeframe is dynamically adjusted based on the timeframe's downlink-to-uplink traffic ratio $\rho = R_{\mathrm{DL}}/R_{\mathrm{UL}}$. After timeslot allocation, $K_{\max} S_{\mathrm{DL}}$ downlink and $K_{\max} S_{\mathrm{UL}}$ uplink physical channels are available for packet transmission, resulting in packet admission ratios $\alpha_{\mathrm{DL}} = \min\{1, K_{\max} S_{\mathrm{DL}}/R_{\mathrm{DL}}\}$ and $\alpha_{\mathrm{UL}} = \min\{1, K_{\max} S_{\mathrm{UL}}/R_{\mathrm{UL}}\}$. Packets of every active MS-BS link are admitted to the system, in first-in-first-out (FIFO) order, according to these ratios. Thus, $A_{\mathrm{DL},i}$ out of $R_{\mathrm{DL},i}$ downlink packets generated by the ith MS-BS link and $A_{\mathrm{UL},i}$ out of $R_{\mathrm{UL},i}$ uplink packets generated by the same link are admitted, with $A_{\mathrm{DL},i} = \lfloor 0.5 + \alpha_{\mathrm{DL}} R_{\mathrm{DL},i} \rfloor$ and $A_{\mathrm{UL},i} = \lfloor 0.5 + \alpha_{\mathrm{UL}} R_{\mathrm{UL},i} \rfloor$. Since a total of $\min\{R_{\mathrm{DL}}, K_{\max} S_{\mathrm{DL}}\}$ downlink and $\min\{R_{\mathrm{UL}}, K_{\max} S_{\mathrm{UL}}\}$ uplink packets can be served

in the current timeframe, an adjustment of $A_{\mathrm{DL},i}$'s or/and $A_{\mathrm{UL},i}$'s might be necessary so that they sum up exactly to these numbers.

The proposed algorithm is 'interference aware' in the sense that the packet assignment rules have been designed with the goal of limiting crossed-slot (BS-to-BS or MS-to-MS) intercell interference. Specifically, the admitted downlink and uplink packets are assigned to timeslot-code channels in *decreasing MS-BS link path loss order*, starting from the beginning or the end of the timeframe, respectively, as shown in Fig. 2.3. In this way, downlink and uplink timeslots occupy the opposite sides of the timeframe and crossed timeslots are more likely to occur in the 'middle', where packets corresponding to MS-BS links with small path losses are assigned. Due to the power control scheme assumed in Section 2.1.1, which is based on a target average receive power, small path losses translate into low transmit power levels and, hence, low crossed-slot interference levels. As a side-effect of the above rules, noncrossed timeslots at the edges of the timeframe (where packets with large MS-BS link path losses are assigned) experience increased intercell interference. This can be suppressed by means of space-time LMMSE-CI joint detection, as described in Section 2.2.1.

2.3.2 Random Dynamic Channel Allocation (RDCA)

The RDCA algorithm considered has the same timeslot allocation and packet admission rules as the IADCA algorithm. However, it differs from the latter in that admitted packets are assigned to timeslot-code channels *at random*, with no regard for the corresponding MS-BS link path losses, and no effort is made to control interference in any part of the timeframe. Consequently, it is probable that crossed timeslots suffer from strong BS-to-BS or MS-to-MS interference, even though noncrossed timeslots, at the edges of a timeframe, might experience weaker intercell interference compared to IADCA.

2.3.3 Fixed Channel Allocation (FCA)

In the FCA algorithm considered, packet admission and assignment to physical channels are performed as in IADCA. Nevertheless, timeslot allocation is *identical* for all cells and remains *fixed* across timeframes, as it is determined by the long-term average downlink-to-uplink traffic ratio $\bar{\rho}$ in the network. For instance, if it is suggested by measurements that, on average, 60% of the traffic is downlink, then 60% of the timeslots

DL and UL timeslot allocation

If $\lceil R_{DL}/K_{max} \rceil + \lceil R_{UL}/K_{max} \rceil \leq S$ then allocate $S_{DL} = \lceil R_{DL}/K_{max} \rceil$ timeslots to DL and $S_{UL} = \lceil R_{UL}/K_{max} \rceil$ timeslots to UL, else $S_{DL} = \lfloor 0.5 + \frac{\rho}{\rho+1}S \rfloor$ and $S_{UL} = S - S_{DL}$, for $\rho = \frac{R_{DL}}{R_{UL}}$.

DL and UL packet admission

Admit $A_{DL,i} = \lfloor 0.5 + \alpha_{DL}R_{DL,i} \rfloor$ DL and $A_{UL,i} = \lfloor 0.5 + \alpha_{UL}R_{UL,i} \rfloor$ UL packets for the ith link; $\alpha_{DL} = \min\{1, \frac{K_{max}S_{DL}}{R_{DL}}\}, \alpha_{UL} = \min\{1, \frac{K_{max}S_{UL}}{R_{UL}}\}$. Adjust $A_{DL,i}$'s and $A_{UL,i}$'s, so that $\sum_i A_{DL,i} = \min\{R_{DL}, K_{max}S_{DL}\}$ and $\sum_i A_{UL,i} = \min\{R_{UL}, K_{max}S_{UL}\}$.

DL packet assignment

Assign admitted DL packets to DL channels in *decreasing* MS-BS link path loss order, starting from the *first* timeslot in the timeframe till all DL timeslots are 'filled', or the admitted DL packets are exhausted.

UL packet assignment

Assign admitted UL packets to UL channels in *decreasing* MS-BS link path loss order, starting from the *last* timeslot in the timeframe till all UL timeslots are 'filled', or the admitted UL packets are exhausted.

Figure 2.3: Flow diagram of the IADCA algorithm and timeslot allocation paradigm for two cells, A and B.

are allocated to downlink and the remaining 40% to uplink in every timeframe and cell. In this way, crossed timeslots and crossed-slot interference are completely eliminated, though at the cost of bandwidth inefficiency and increased packet blocking compared with DCA algorithms.

2.4 Performance Metrics

To assess the performance of the proposed IADCA/space-time LMMSE joint detection scheme and compare it with that of benchmark RDCA and FCA schemes, two metrics are used, namely 1) the SINR cumulative distribution function (cdf) and 2) the average throughput. As a link-level metric, the SINR cdf characterizes the efficiency of a scheme in coping with channel impairments, such as ISI, intracell MAI, and intercell interference. It provides the outage probability $P_o = P(\gamma \leq \gamma_o)$ associated with any SINR value γ_o or, equivalently, the SINR value γ_o that can be sustained with probability $1 - P_o = P(\gamma > \gamma_o)$ for any outage level P_o. As a system-level metric, the average throughput additionally captures the effect of channel allocation on resource utilization. In this chapter, it is defined as the average probability that a typical packet, which is generated at the beginning of a timeframe, is admitted for transmission and correctly received by its intended recipient during that timeframe. Hence, retransmission of blocked or erroneously received packets in subsequent timeframes is not considered.

Following this definition, the downlink average throughput can be expressed as

$$
\begin{aligned}
\bar{T}_{\mathrm{DL}} &= \bar{P}(\text{DL packet is admitted and correctly received}) \\
&= P(\text{DL packet is admitted}) \cdot \\
&\quad \bar{P}(\text{DL packet is correctly received|DL packet is admitted}) \\
&= (1 - P_{B,\mathrm{DL}})\bar{P}_{C,\mathrm{DL}}
\end{aligned}
\tag{2.32}
$$

and, similarly, the uplink average throughput as

$$
\bar{T}_{\mathrm{UL}} = (1 - P_{B,\mathrm{UL}})\bar{P}_{C,\mathrm{UL}}.
\tag{2.33}
$$

In the above expressions, $P_{B,\mathrm{DL}}$ and $P_{B,\mathrm{UL}}$ denote, respectively, the probability that a generated downlink or uplink packet is blocked from transmission. This probability depends on the channel allocation algorithm used and the traffic load in the network, and it can be either analytically evaluated (for simple allocation rules and traffic models)

or empirically estimated via simulations. Moreover, $\bar{P}_{C,\mathrm{DL}}$ and $\bar{P}_{C,\mathrm{UL}}$ denote the average probability that an admitted downlink or uplink packet is correctly received, which depends both on the channel allocation algorithm and the signal detector used. Error-correcting coding is not considered herein; therefore, a correctly received packet is one with no bits in error. In general, hard decisions on neighboring bits of a packet are correlated since the residual interference terms of the corresponding soft LMMSE symbol estimates, in (2.17), are correlated. However, to simplify the analysis, we make the approximation that bit errors occur *independently* with probability P_b, which is given by (2.19) for the kth packet in a reference timeslot. Thus, assuming B_p bits per packet, it is

$$\bar{P}_{C,\mathrm{DL}} = E_{\mathrm{DL}}\left\{(1 - P_b)^{B_p}\right\} \qquad \text{and} \qquad \bar{P}_{C,\mathrm{UL}} = E_{\mathrm{UL}}\left\{(1 - P_b)^{B_p}\right\} \tag{2.34}$$

where the expectations $E_{\mathrm{DL}}\{\cdot\}$ and $E_{\mathrm{UL}}\{\cdot\}$ are obtained by averaging over the probability distribution of P_b for downlink and uplink timeslots, respectively. The accuracy of the above approximation is investigated in Section 2.5.4.

The theoretical derivation of the SINR and P_b probability distributions, under realistic channel and traffic models, is too involved to allow analytical performance results. Consequently, the SINR outage and average throughput are evaluated by means of packet-level Monte Carlo simulations of a seven-cell TDD/CDMA network for a large number of timeframes, as described in the following section.

2.5 Simulation Results

2.5.1 Simulation Setup

The simulation parameters are listed in Table 2.1. Every cell serves the same number of mobile stations, whose locations are randomly varied per timeframe following the 2-D uniform distribution. Assuming pedestrian speeds (up to 2 m/s), mobility has hardly any effect on the system performance, due to small normalized Doppler spread,[5] and it is not considered in the simulations. In each timeframe and cell, timeslots are allocated to downlink and uplink, and generated packets are admitted and assigned to timeslot-code channels based on the channel allocation algorithm under study. Blocked

---

[5]For carrier frequency $f_c = 1900$ MHz and mobile station speed $v_{\mathrm{MS}} = 2$ m/s, the Doppler spread normalized to the timeslot rate $1/T_S$ (see Table 2.1) is $f_D T_S \approx 0.0084 \ll 1$, justifying the assumption of time-invariant channels made in Section 2.1.2.

Table 2.1: Simulation parameters.

Cell radius	$R_c = 500$ m
RRC roll-off factor	$\beta = 0.22$
Target average received power	$P_{R,\text{trgt}} = -97$ dBm
Chip rate	$1/T_c = 3.84$ Mcps
Timeslot rate	$1/T_S = 1500$ tslots/s
Timeslots/timeframe	$S = 8$
Channelization codes/timeslot	$K_{\max} = 4$
Spreading factor	$Q = 16$
Packet length	$B_p = 256$ bits
Effective channel impulse response length	$P = 34$ chips
Training length	$V = 352$ chips

downlink and uplink packets are counted towards the estimation of the respective blocking probabilities $P_{B,\text{DL}}$ and $P_{B,\text{UL}}$. In each timeslot, an admitted packet in the central cell is randomly selected as reference. The parameters of the received signal model (2.11) are generated using (2.10) and (2.12), and space-time LMMSE joint detection is performed on the basis of (2.14) or (2.15). Both cases of perfect and imperfect CSI are considered. In the latter case, the intracell channel coefficients and intercell-interference-plus-noise statistics are estimated, as described in Section 2.2.2, for $V = 352$ training chips. The SINR γ and the bit error probability P_b of the reference packet are computed by (2.18) and (2.19) and are used in the numerical evaluation of the downlink or uplink SINR cdf and average packet success probability $\bar{P}_C$ via (2.34). Finally, the average throughput is calculated by (2.32) or (2.33).

To simulate asymmetric data traffic, the dynamic traffic model developed in [11] is employed. Based on this model, the traffic carried by an MS-BS link is generated according to an event-driven Markov process. Each state of the process corresponds to an application-specific client-server packet flow that consists of a predetermined number of downlink and uplink packets with fixed length $B_p = 256$ bits. The model parameters (i.e., packet flow sizes and state transition probabilities) were determined for various applications (e.g., hypertext transfer protocol (HTTP), file transfer protocol (FTP), etc.) by measurements taken at the University of California, San Diego, campus-wide IEEE 802.11b wireless local area network. These measurements were characterized by

average downlink-to-uplink traffic ratio $\bar{\rho} = 3 : 1$.

The urban microcell 3GPP/3GPP2 NLOS spatial channel model [2], for $N = 6$ path clusters with uniformly distributed delays in $(0, 1.2\,\mu\text{s})$, is used to simulate the MS-BS channel impulse responses described by (2.3). Antenna element spacings equal to λ_c and $10\lambda_c$ are assumed at the mobile and base stations, respectively, with λ_c denoting the carrier wavelength. The propagation loss of MS-BS links is provided by the COST 231 Walfisch-Ikegami NLOS model [12] for carrier frequency $f_c = 1900$ MHz, while lognormal shadowing of standard deviation $\sigma_{\text{SF,MS}-\text{BS}} = 10$ dB is also considered. To account for crossed-slot interference scenarios, the 3GPP/3GPP2 model is extended to generate the channel impulse responses of MS-MS and BS-BS links. This extension and the propagation loss models used in these scenarios are described in Appendix B. Lognormal shadowing of $\sigma_{\text{SF,MS}-\text{MS}} = 12$ dB and $\sigma_{\text{SF,BS}-\text{BS}} = 6$ dB is also considered.

2.5.2 Packet Blocking Probabilities

The packet blocking probabilities $P_{B,\text{DL}}$ and $P_{B,\text{UL}}$, which were numerically estimated over 10^6 timeframes for various numbers of mobile stations per cell, are provided in Table 2.2 for all three channel allocation algorithms considered. Obviously, these probabilities increase with the number of mobile stations, as more generated packets contend for a fixed number of timeslot-code channels per timeframe. IADCA and RDCA block packets less often than FCA by virtue of flexible timeslot allocation. In these algorithms, the downlink-to-uplink timeslot ratio is approximately matched to the downlink-to-uplink traffic ratio in each timeframe, and hence, blocking probabilities are similar for the two transmission directions. In contrast, FCA constantly allocates $S_{\text{DL}} = 6$ out of $S = 8$ timeslots per timeframe to downlink and only $S_{\text{UL}} = 2$ timeslots to uplink in accordance with the average downlink-to-uplink traffic ratio $\bar{\rho} = 3 : 1$ characterizing the simulations. Therefore, a larger percentage of uplink than downlink packets are blocked from transmission as the actual traffic ratio fluctuates around this average value.

2.5.3 SINR Outage

In Figs. 2.4 - 2.9, plots of uplink and downlink SINR cdf are shown for the channel allocation algorithms of Section 2.3 with single- and dual-antenna LMMSE-CI or LMMSE-WI joint detection, assuming 32 mobile stations per cell (i.e., under heavy

Table 2.2: Numerically estimated packet blocking probabilities.

MSs/cell	$P_{B,\text{DL}}$		$P_{B,\text{UL}}$	
	IADCA/RDCA	FCA	IADCA/RDCA	FCA
1	0.000	0.000	0.000	0.000
4	0.000	0.000	0.000	0.058
8	0.001	0.006	0.001	0.098
12	0.010	0.022	0.008	0.151
16	0.028	0.050	0.023	0.201
20	0.059	0.085	0.055	0.259
24	0.093	0.126	0.088	0.285
28	0.140	0.168	0.135	0.337
32	0.187	0.218	0.182	0.360

traffic load conditions).

Fig. 2.4 illustrates the impact of the joint detection scheme on the uplink SINR for IADCA, assuming perfect CSI at the receiver. At any outage level, both the LMMSE-WI and the LMMSE-CI SINR increase with the number of receive antennas due to array and diversity gain provided by LMMSE combining. Furthermore, knowledge of the intercell-interference-plus-noise autocorrelation matrix $\boldsymbol{R_n}$, in LMMSE-CI joint detection, results in SINR gain relative to LMMSE-WI. This gain is larger for dual- than single-antenna reception since the spatial information conveyed by $\boldsymbol{R_n}$, in the former case, is exploited to suppress the strongest intercell interferer. The effect of imperfect CSI is shown in Fig. 2.5. All the detection schemes experience SINR degradation, which is more significant for dual-antenna LMMSE-CI joint detection, amounting to 4 dB at 10% outage probability. The LMMSE-CI SINR is still better than the LMMSE-WI SINR at meaningful outage levels; however, it becomes slightly worse at high outage levels, and the respective cdf curves intersect. This occurs because the performance of LMMSE-CI joint detection depends significantly on the estimation accuracy of $\boldsymbol{R_n}$, which degrades for low intercell-interference-plus-noise levels (i.e., high SINR levels). Trends similar to those of Figs. 2.4 and 2.5 have also been observed in downlink.

In Fig. 2.6, IADCA is compared against RDCA and FCA in terms of uplink SINR for single- and dual-antenna LMMSE-CI joint detection with imperfect CSI. In both cases, IADCA outperforms RDCA but achieves lower SINR than FCA at any outage
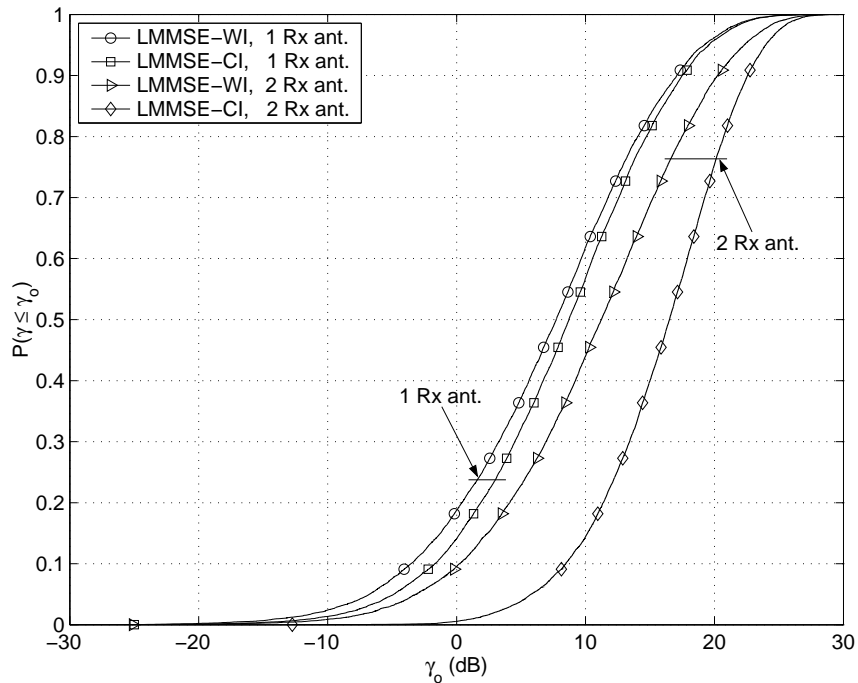
Figure 2.4: Uplink SINR cdf plots for IADCA with single- and dual-antenna LMMSE-WI and LMMSE-CI joint detection, assuming perfect CSI; 32MSs/cell and 8000 timeframes.

probability. This is explained by Fig. 2.7, where separate SINR cdf plots are provided for crossed and noncrossed timeslots, assuming two receive antennas. For RDCA, severe SINR degradation over crossed timeslots is observed, which is caused by strong BS-to-BS interference. IADCA mitigates this type of interference and considerably improves the crossed timeslot SINR by assigning packets to physical channels in decreasing MS-BS link path loss order, from the edges to the 'middle' of the timeframe. In this way, intercell interference over noncrossed timeslots increases relative to RDCA. Nevertheless, for numerous mobile stations per cell, the overall SINR cdf of IADCA is superior to that of RDCA because a large portion of uplink timeslots are crossed, thus dominating performance. In contrast, for FCA, all timeslots are noncrossed and free from BS-to-BS interference, resulting in even higher SINR than IADCA.

Fig. 2.8 compares IADCA against RDCA and FCA in terms of downlink SINR. IADCA and FCA perform slightly better than RDCA for one receive antenna, while all three schemes have similar performance, particularly at low outage, for two receive antennas. This is due to the fact that crossed-slot interference is *not* detrimental in downlink, as verified in Fig. 2.9. Indeed, the SINR achieved by RDCA over crossed timeslots is
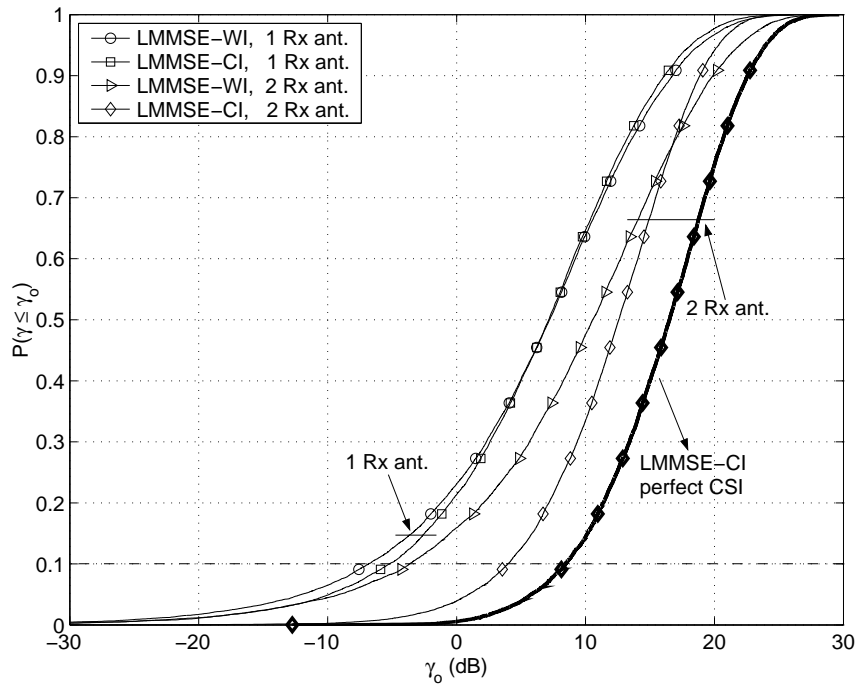
Figure 2.5: Uplink SINR cdf plots for IADCA with single- and dual-antenna LMMSE-WI and LMMSE-CI joint detection under imperfect CSI, estimated as in Section 2.2.2; 32MSs/cell and 8000 timeframes.
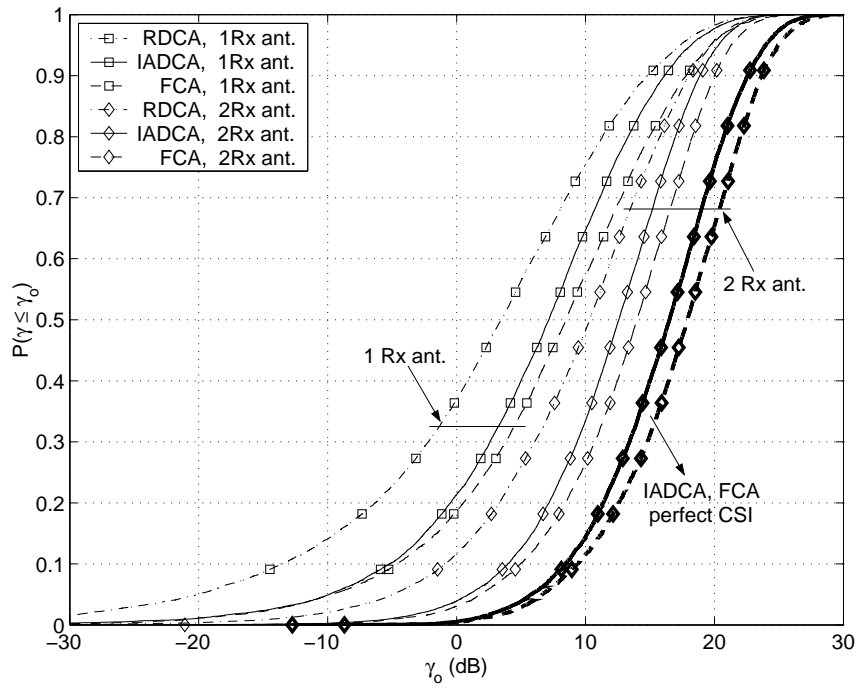
Figure 2.6: Uplink SINR cdf comparison of IADCA against RDCA and FCA for single-and dual-antenna LMMSE-CI joint detection with imperfect CSI; 32MSs/cell and 8000 timeframes.
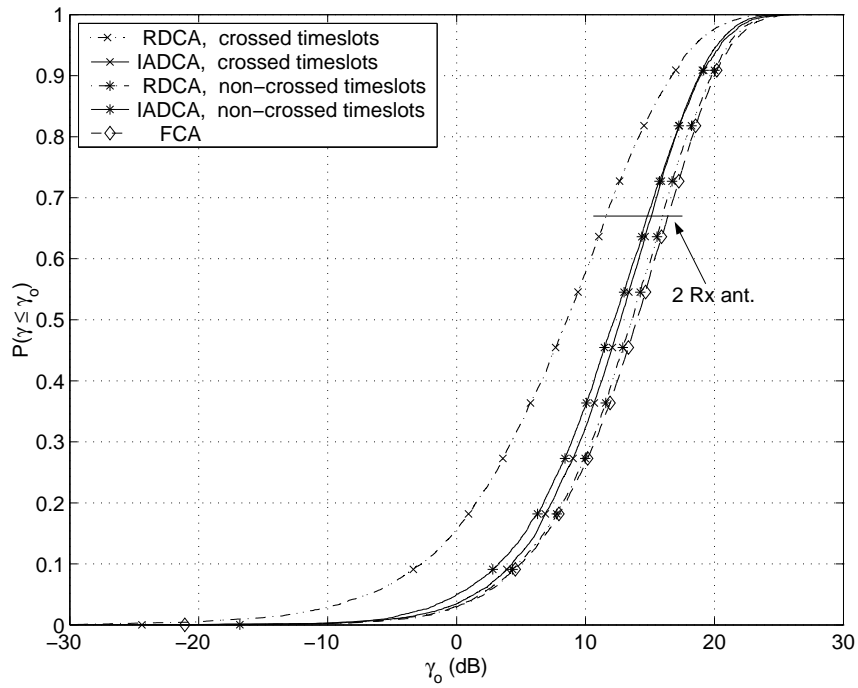
Figure 2.7: Uplink SINR cdf plots for IADCA over crossed and noncrossed timeslots, RDCA over crossed and noncrossed timeslots, and FCA with dual-antenna LMMSE-CI joint detection under imperfect CSI; 32MSs/cell and 8000 timeframes.
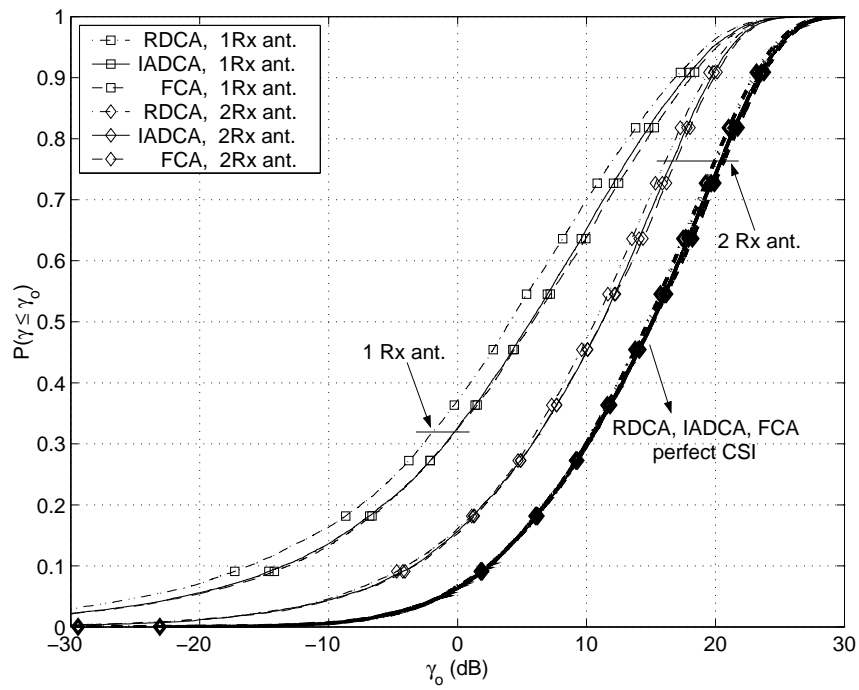
Figure 2.8: Downlink SINR cdf comparison of IADCA against RDCA and FCA for single- and dual-antenna LMMSE-CI joint detection with imperfect CSI; 32MSs/cell and 3400 timeframes.
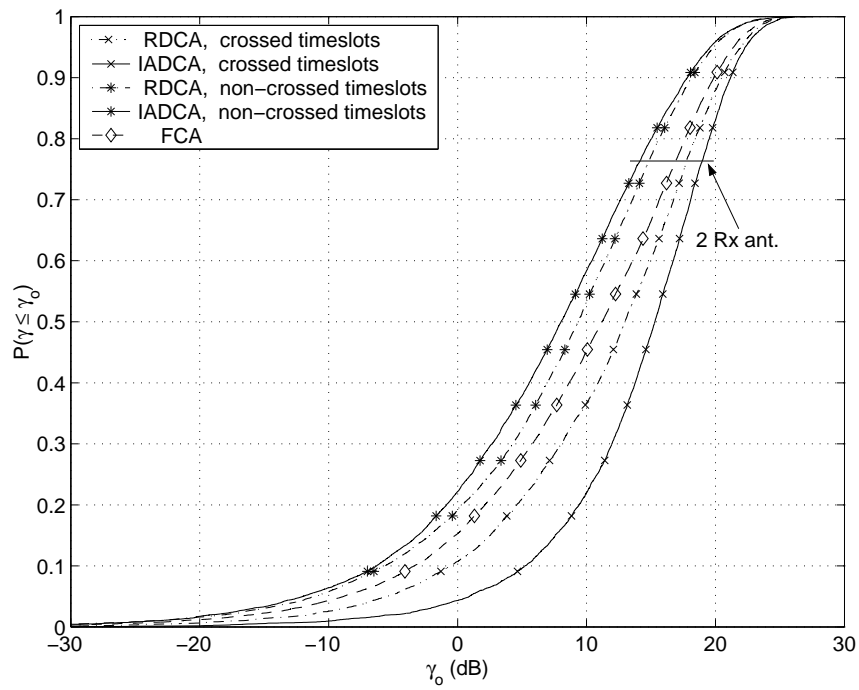
Figure 2.9: Downlink SINR cdf plots for IADCA over crossed and noncrossed timeslots, RDCA over crossed and noncrossed timeslots, and FCA with dual-antenna LMMSE-CI joint detection under imperfect CSI; 32MSs/cell and 3400 timeframes.

higher than the SINR over noncrossed timeslots, exceeding even the SINR achieved by FCA. The reason for this trend is two-fold. First, MS-to-MS interference is typically weaker than BS-to-MS interference since MS-MS links experience more severe scattering than MS-BS links. Second, in the rare occasion that two mobile stations engaged in opposite-direction transmissions are close to each other, dual-antenna LMMSE-CI joint detection efficiently suppresses the strong MS-to-MS interference that arises. Compared with RDCA, IADCA further diminishes intercell interference over crossed timeslots albeit at the cost of increased intercell interference over noncrossed timeslots, affecting the respective SINR cdfs accordingly. The overall IADCA and RDCA SINR cdfs that emerge are similar to each other and to the FCA SINR cdf, and the exact relation among the three is determined by the relative frequency of crossed versus noncrossed downlink timeslots. For the traffic model considered, where 75% of the traffic is downlink on average, this frequency is smaller than in uplink.

2.5.4   Average Throughput

In Fig. 2.10, the uplink average throughput is plotted versus the number of mobile stations per cell for all three channel allocation algorithms with LMMSE-CI joint detection. To examine the accuracy of the Gaussian residual interference approximation, in (2.19), and the bit-error independence approximation, in (2.34), two sets of curves are plotted. The first, which is labeled 'packet-level sim', corresponds to the throughput obtained by (2.33) when the average packet success probability $\bar{P}_{C,\mathrm{UL}}$ is evaluated by packet-level simulations on the basis of (2.19) and (2.34), as described in Section 2.5.1. The second, which is labeled 'bit-level sim', corresponds to the throughput obtained by (2.33) when $\bar{P}_{C,\mathrm{UL}}$ is evaluated by 'brute-force' bit-level simulations of the actual packet transmission and detection. It is observed that the above approximations result in throughput values that closely match those obtained by bit-level simulations, particularly for two receive antennas. Thus, their use is justified since they facilitate performance evaluation for only a slight loss in accuracy.

Focusing on the packet-level simulation curves, the following remarks can be made. The throughput of IADCA exceeds that of RDCA as the traffic load increases, thanks to reduced crossed-slot interference and, therefore, increased average packet success probability $\bar{P}_{C,\mathrm{UL}}$. IADCA also achieves higher throughput than FCA, despite worse SINR outage, due to flexible timeslot allocation resulting in reduced blocking probability
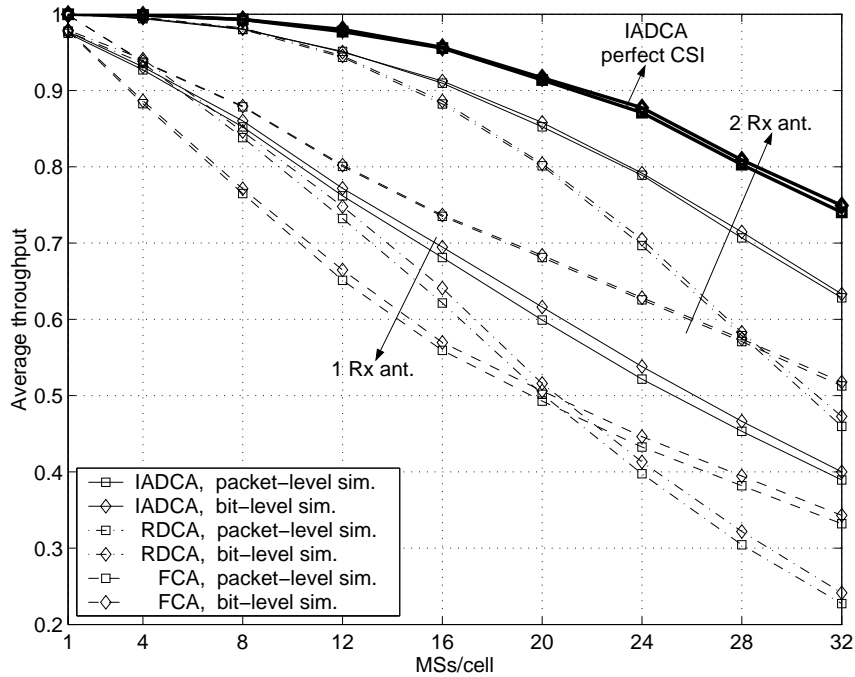
Figure 2.10: Uplink average throughput versus the number of mobile stations per cell for IADCA, RDCA, and FCA with single- and dual-antenna LMMSE-CI joint detection under imperfect CSI.

$P_{B,\mathrm{UL}}$ that dominates the product of (2.33). For the same reason, FCA is also outper-formed by RDCA under moderate traffic loads. However, the trend is reversed under heavy traffic loads, as packet errors for RDCA significantly increase due to uncontrolled crossed-slot interference. Notably, the throughput gap between IADCA and FCA in-creases for two receive antennas, suggesting that space-time LMMSE-CI joint detection is more beneficial to the former, which suffers from stronger intercell interference than the latter.

The downlink average throughput is plotted in Fig. 2.11. For clarity of pre-sentation, only the packet-level simulation curves are provided, noting that they tightly match the bit-level simulation curves, as in uplink. All the three schemes considered achieve similar throughput due to small differences in downlink SINR outage and packet blocking probability. Specifically, the throughput of IADCA is slightly better than that of FCA for dual-antenna reception, even though the two are almost identical for single-antenna reception. Moreover, IADCA outperforms RDCA for a large number of mobile stations per cell, as the impact of crossed timeslots increases, while its throughput is marginally worse than that of RDCA under light traffic loads, because of higher intercell
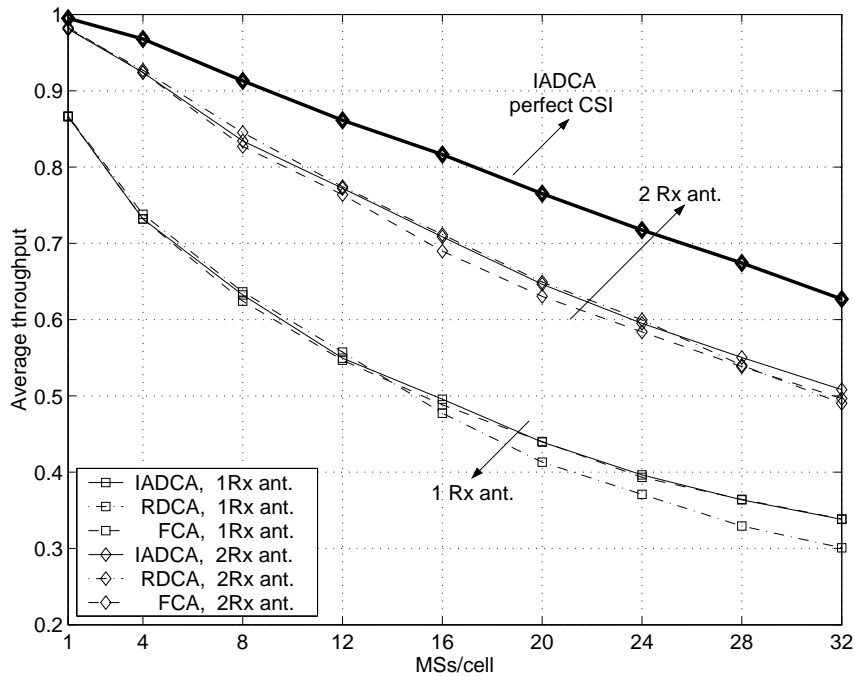
Figure 2.11: Downlink average throughput versus the number of mobile stations per cell for IADCA, RDCA, and FCA with single- and dual-antenna LMMSE-CI joint detection under imperfect CSI.

interference over noncrossed timeslots.

In Fig. 2.12, the uplink throughput of two test schemes, namely, RDCA/LMMSE-CI and IADCA/ LMMSE-WI, is plotted to illustrate the relative effect of interference avoidance and interference suppression on system performance. The first scheme copes with crossed-slot interference only by suppressing it in detection and the second only by avoiding it in channel allocation. The throughput of the proposed IADCA/LMMSE-CI scheme is also plotted for reference. It is observed that interference avoidance via IADCA is more effective than interference suppression via LMMSE-CI joint detection when there are *not enough* degrees of freedom at the receiver for the level of intercell interference encountered. This is the case for one receive antenna or two receive antennas under heavy traffic loads. In contrast, for two receive antennas under moderate traffic loads, the spatial information conveyed by $\boldsymbol{R_n}$ to the receiver is sufficient to ensure that suppressing crossed-slot interference is more effective than avoiding it. In any case, the proposed scheme achieves superior performance by combining interference avoidance in channel allocation with interference suppression in signal detection.
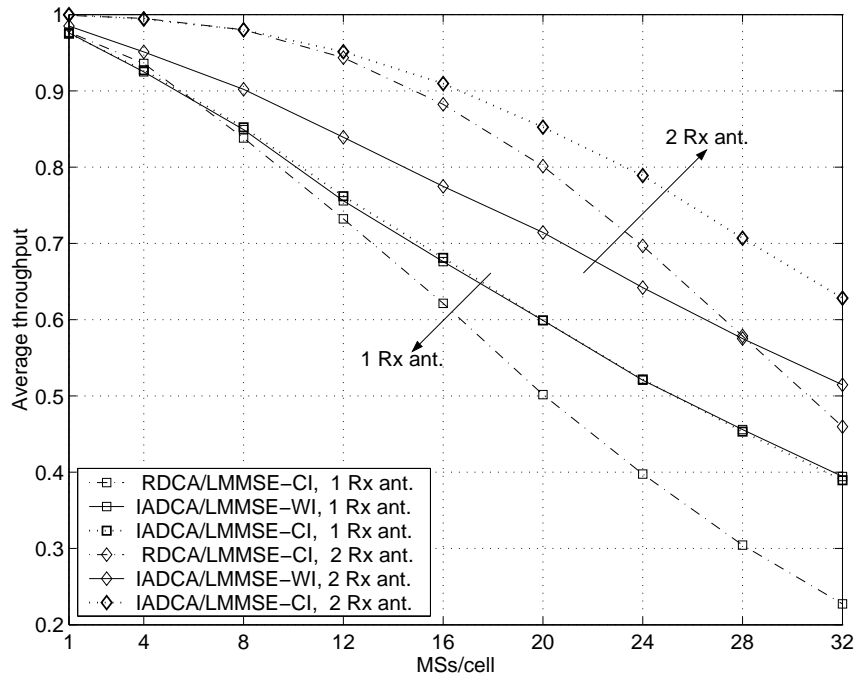
Figure 2.12: Uplink average throughput versus the number of mobile stations per cell for RDCA/LMMSE-CI, IADCA/LMMSE-WI, and IADCA/LMMSE-CI with single- and dual-antenna reception under imperfect CSI.

2.6 Acknowledgement

Chapter 2, in part, is a reprint of the material as it appears in I. Spyropoulos and J. R. Zeidler, "Dynamic Channel Allocation and Space-Time LMMSE Joint Detection in a TDD/CDMA Cellular Network with Traffic Asymmetry," *Proceedings of IEEE Vehicular Technology Conference (VTC)*, Dublin, Ireland, Apr. 2007, pp. 3066–3070 and I. Spyropoulos and J. R. Zeidler, "Supporting Asymmetric Traffic in a TDD/CDMA Cellular Network via Interference-Aware Dynamic Channel Allocation and Space-Time LMMSE Joint Detection," *IEEE Transactions on Vehicular Technology*, vol. 58, no. 2, pp. 744–759, Feb. 2009. The dissertation author was the primary investigator and author of these papers.

3 PHY-MAC Cross-Layer Design in Multiple-Antenna Ad Hoc Networks

In their effort to limit interference around receivers, MAC protocols based on collision avoidance achieve poor spatial reuse and, thus, restrict the throughput of ad hoc networks. In this chapter, two physical-medium-access-control cross-layer protocols are proposed to enhance network throughput in an energy-efficient manner. The first increases spatial reuse by integrating medium access, power control, and optimum receive beamforming in a distributed fashion and is named progressive back-off algorithm with optimum receive beamforming (PBOA-ORB). The second additionally incorporates transmit beamforming, on the premise of centralized control, and is named progressive back-off algorithm with transmit and optimum receive beamforming (PBOA-TORB).

This chapter is organized as follows. The ad hoc network model is introduced in Section 3.1 and the proposed PBOA-ORB and PBOA-TORB protocols are presented in Sections 3.2 and 3.3, respectively. Section 3.4 describes the simulation model used for performance evaluation and discusses the simulation results.

3.1   Network Model

Consider an ad hoc network of N nodes that communicate with each other by exchanging packets over a wireless channel, at a common transmission rate R. For the purposes of this chapter, which focuses on the physical and MAC layers, the network is *single-hop*, meaning that nodes communicate directly, without relaying. Packet transmission is frame-based, and the nodes are synchronized to the frame boundaries. This
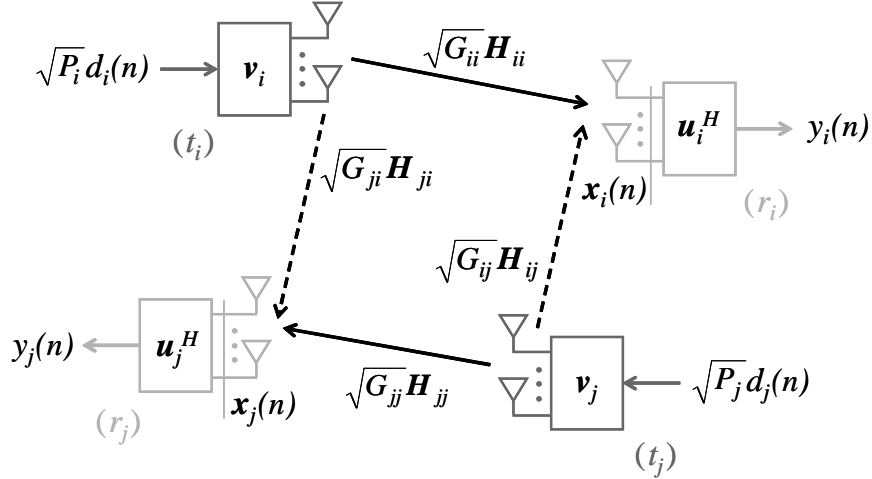
Figure 3.1: Baseband equivalent link model of the ad hoc network under study. Two links are considered, namely, link i between nodes t_i and r_i, and link j between nodes t_j and r_j.

can be practically achieved via GPS technology or clock synchronization protocols, such as those proposed in [37] and [54]. Each node is equipped with a packet queue, a half-duplex transceiver, and an array of M omnidirectional antenna elements. By virtue of this array, nodes are capable of transmit beamforming (i.e., sending weighted versions of the same data symbol over the transmit antennas) and receive beamforming (i.e., coherently combining the signals at the receive antenna outputs) for enhanced communication efficiency.

The baseband equivalent link model of the ad hoc network under study is illustrated in Fig. 3.1. Only two links out of the set $\mathcal{L}$ of active links are shown for simplicity; namely, link i between the transmitting node t_i and its intended receiver r_i and link j between nodes t_j and r_j. Node t_i transmits a packet at power P_i, in the range $[0, P_{\max}]$, weighting each data symbol $d_i(n)$ by the elements of an $M \times 1$ unit-norm beamforming vector $\boldsymbol{v}_i$. The channel from node t_j to node r_i is described by the power gain G_{ij} and the $M \times M$ channel matrix $\boldsymbol{H}_{ij}$ and is assumed *time invariant* for the duration of a frame. This is a reasonable assumption for low-mobility (e.g., pedestrian) scenarios. The power gain captures the effects of distance-dependent propagation and shadowing, while the $k\ell$th element of $\boldsymbol{H}_{ij}$ captures the fading between the ℓth transmit antenna of node t_j and the kth receive antenna of node r_i, which is assumed to be flat.

The received signals at the antenna outputs of node r_i are represented by the

$M \times 1$ vector

$$\boldsymbol{x}_i(n) = \sqrt{P_i G_{ii}} \boldsymbol{H}_{ii} \boldsymbol{v}_i d_i(n) + \sum_{\substack{j \neq i \\ j \in \mathcal{L}}} \sqrt{P_j G_{ij}} \boldsymbol{H}_{ij} \boldsymbol{v}_j d_j(n) + \boldsymbol{w}_i(n). \tag{3.1}$$

These signals are linearly combined with weights provided by the conjugate of the beam-forming vector $\boldsymbol{u}_i$, and the output of the receive beamformer is

$$y_i(n) = \sqrt{P_i G_{ii}} \boldsymbol{u}_i^H \boldsymbol{H}_{ii} \boldsymbol{v}_i d_i(n) + \sum_{\substack{j \neq i \\ j \in \mathcal{L}}} \sqrt{P_j G_{ij}} \boldsymbol{u}_i^H \boldsymbol{H}_{ij} \boldsymbol{v}_j d_j(n) + \boldsymbol{u}_i^H \boldsymbol{w}_i(n). \tag{3.2}$$

In the previous expressions, the first term corresponds to the desired signal from node t_i, the second term to interference from other transmitting nodes, such as t_j, and the third term to thermal and background noise. The latter is modeled by the zero-mean circularly symmetric complex Gaussian random vector $\boldsymbol{w}_i(n)$ with covariance matrix $\boldsymbol{\Phi}_{\boldsymbol{w}_i} = \sigma_w^2 \boldsymbol{I}$, for noise power σ_w^2 at each antenna. Assuming that the data symbols $d_i(n)$, $d_j(n)$ are uncorrelated and drawn from a unit-energy constellation, the SINR at the output of the receive beamformer is

$$\gamma_i = \frac{P_i G_{ii} \boldsymbol{u}_i^H \boldsymbol{H}_{ii} \boldsymbol{v}_i \boldsymbol{v}_i^H \boldsymbol{H}_{ii}^H \boldsymbol{u}_i}{\sum_{\substack{j \neq i \\ j \in \mathcal{L}}} P_j G_{ij} \boldsymbol{u}_i^H \boldsymbol{H}_{ij} \boldsymbol{v}_j \boldsymbol{v}_j^H \boldsymbol{H}_{ij}^H \boldsymbol{u}_i + \sigma_w^2 \boldsymbol{u}_i^H \boldsymbol{u}_i} \tag{3.3a}$$

$$= \frac{P_i G_{ii} \boldsymbol{u}_i^H \boldsymbol{H}_{ii} \boldsymbol{v}_i \boldsymbol{v}_i^H \boldsymbol{H}_{ii}^H \boldsymbol{u}_i}{\boldsymbol{u}_i^H \boldsymbol{\Phi}_{I,i} \boldsymbol{u}_i} \tag{3.3b}$$

where

$$\boldsymbol{\Phi}_{I,i} = \sum_{\substack{j \neq i \\ j \in \mathcal{L}}} P_j G_{ij} \boldsymbol{H}_{ij} \boldsymbol{v}_j \boldsymbol{v}_j^H \boldsymbol{H}_{ij}^H + \sigma_w^2 \boldsymbol{I} \tag{3.4}$$

denotes the interference-plus-noise covariance matrix. Throughout this chapter, it is assumed that node r_i is able to receive a packet from node t_i *successfully* (i.e., with negligible probability of error) provided that the SINR γ_i exceeds a threshold γ_T, which depends on the common transmission rate R and the modulation/coding scheme used. Otherwise, the packet cannot be detected.

3.1.1 Receive Beamforming

Based on the above assumption, it is optimum, in terms of packet throughput, that node r_i employs the receive beamforming vector $\boldsymbol{u}_i$ which maximizes the SINR for given transmit beamforming vectors $\{\boldsymbol{v}_i\}_{i \in \mathcal{L}}$. Using the theory of generalized eigenvalues

(e.g., see [16]), it is straightforward to show that this optimum receive beamforming (ORB) vector is given by

$$
\begin{aligned}
\boldsymbol{u}_{i,o} &= \underset{|\boldsymbol{u}_i|=1}{\operatorname{argmax}} \left\{ \frac{\boldsymbol{u}_i^H \boldsymbol{H}_{ii} \boldsymbol{v}_i \boldsymbol{v}_i^H \boldsymbol{H}_{ii}^H \boldsymbol{u}_i}{\boldsymbol{u}_i^H \boldsymbol{\Phi}_{I,i} \boldsymbol{u}_i} \right\} \\
&= \frac{\boldsymbol{\Phi}_{I,i}^{-1} \boldsymbol{H}_{ii} \boldsymbol{v}_i}{|\boldsymbol{\Phi}_{I,i}^{-1} \boldsymbol{H}_{ii} \boldsymbol{v}_i|}
\end{aligned}
\tag{3.5}
$$

when a unit-norm constraint is also imposed on $\boldsymbol{u}_i$ without loss of generality. In this case, due to (3.3b), the maximum SINR can be expressed as

$$
\begin{aligned}
\gamma_{i,o} &= \frac{P_i G_{ii} \boldsymbol{u}_{i,o}^H \boldsymbol{H}_{ii} \boldsymbol{v}_i \boldsymbol{v}_i^H \boldsymbol{H}_{ii}^H \boldsymbol{u}_{i,o}}{\boldsymbol{u}_{i,o}^H \boldsymbol{\Phi}_{I,i} \boldsymbol{u}_{i,o}} \\
&= P_i G_{ii} \boldsymbol{v}_i^H \boldsymbol{H}_{ii}^H \boldsymbol{\Phi}_{I,i}^{-1} \boldsymbol{H}_{ii} \boldsymbol{v}_i.
\end{aligned}
\tag{3.6}
$$

In essence, the optimum receive beamformer maximizes the SINR by selecting its weights so that the array response $y_i(n)$ is enhanced along the 'spatial signature' $\boldsymbol{H}_{ii}\boldsymbol{v}_i$ of the desired signal and reduced along the 'spatial signatures' $\boldsymbol{H}_{ij}\boldsymbol{v}_j$ of the main interferers.

It is well known that the minimum-mean-square-error (MMSE) beamformer also achieves maximum SINR $\gamma_{i,o}$ (e.g., see [46]). This beamformer, which minimizes the mean square error between the desired signal $d_i(n)$ and its output, is given by

$$
\begin{aligned}
\boldsymbol{u}_{i,\mathrm{MMSE}} &= \underset{\boldsymbol{u}_i}{\operatorname{argmin}} \; E\big\{ |d_i(n) - \boldsymbol{u}_i^H \boldsymbol{x}_i(n)|^2 \big\} \\
&= \frac{\sqrt{P_i G_{ii}}}{1 + P_i G_{ii} \boldsymbol{v}_i^H \boldsymbol{H}_{ii}^H \boldsymbol{\Phi}_{I,i}^{-1} \boldsymbol{H}_{ii} \boldsymbol{v}_i} \boldsymbol{\Phi}_{I,i}^{-1} \boldsymbol{H}_{ii} \boldsymbol{v}_i,
\end{aligned}
\tag{3.7}
$$

while the SINR at its output can be expressed as

$$
\gamma_{i,o} = \frac{1}{E\big\{ |d_i(n) - \boldsymbol{u}_{i,MMSE}^H \boldsymbol{x}_i(n)|^2 \big\}} - 1.
\tag{3.8}
$$

In practical systems, the MMSE beamformer is implemented by means of an adaptive algorithm (e.g., LMS or RLS) that estimates a training sequence $\big\{ d_i(n) \big\}$ *a priori* known to the receiver. Hence, there is no need for accurate knowledge of the effective channel vector $\boldsymbol{H}_{ii}\boldsymbol{v}_i$ and the interference-plus-noise covariance matrix $\boldsymbol{\Phi}_{I,i}$ at the receiver, as suggested by the theoretical expression in (3.7). In addition, the maximum SINR $\gamma_{i,o}$ can be readily computed by measuring the mean square error at the output of the adaptive beamformer after convergence. This practical implementation also applies to the optimum beamformer of (3.5), which is just a normalized version of the MMSE beamformer.
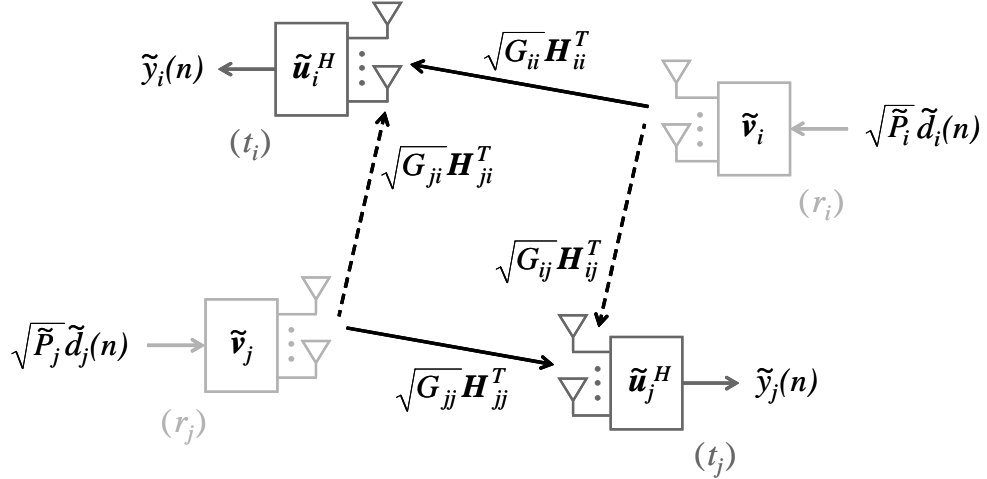
Figure 3.2: Baseband equivalent link model of the dual topology network corresponding to the network of Fig 3.1.

As a final remark on receive beamforming, note that the model considered in this chapter implicitly accounts for the case where two (or more) nodes, for instance t_i and t_j, transmit one packet each to node $r_i \equiv r_j$ at the same time. The antenna outputs $\boldsymbol{x}_i(n)$ can be linearly combined using two different receive beamformers $\boldsymbol{u}_{i,o}$ and $\boldsymbol{u}_{j,o}$, one adapting to estimate the training sequence of t_i and the other the training sequence of t_j, provided that these are uncorrelated and *a priori* known to the receiver. In this way, node r_i is able to successfully receive up to two packets depending on whether the corresponding SINRs exceed the threshold γ_T or not. This multi-packet reception capability generalizes up to M packets for nodes with M antennas.

3.1.2 Transmit Beamforming

Given the SINR threshold model for successful packet reception, it is also desirable that the transmit beamforming vectors $\{\boldsymbol{v}_i\}_{i\in\mathcal{L}}$ are optimized with respect to SINR for fixed receive beamforming vectors $\{\boldsymbol{u}_i\}_{i\in\mathcal{L}}$. However, the trasmit beamforming optimization problem is significantly more involved than the receive beamforming optimization problem. This is due to the fact that transmit beamforming affects the SINR of *all* links, hence it requires network-wide optimization, in contrast to receive beamforming, which affects the SINR of a single link and is optimized for each link individually. Previous works, such as [35], [48], and [38], have addressed this issue by transforming the hard transmit beamforming problem into a simpler receive beamform-

ing problem in the network whose links are reciprocal to those of the original network. This is referred to as *dual topology* network and is depicted in Fig. 3.2 for the original network of Fig. 3.1. The theoretical basis for the above transformation is provided by Theorem 1 in [38], which is restated herein.

Network Duality Theorem. *Consider a MIMO ad hoc network consisting of $L = |\mathcal{L}|$ links that employ transmit beamforming vectors $\{v_i\}_{i \in \mathcal{L}}$ and receive beamforming vectors $\{u_i\}_{i \in \mathcal{L}}$. A set of SINR values $\{\gamma_i\}_{i \in \mathcal{L}}$ is achievable in this network for transmit powers $p = [P_1, \ldots, P_L]^T$, if and only if it is achievable in the dual topology network using transmit beamforming vectors $\{\tilde{v}_i = u_i^*\}_{i \in \mathcal{L}}$ and receive beamforming vectors $\{\tilde{u}_i = v_i^*\}_{i \in \mathcal{L}}$ for transmit powers $\tilde{p} = [\tilde{P}_1, \ldots, \tilde{P}_L]^T$. Furthermore, the transmit power vectors are related by $\tilde{n}^T p = n^T \tilde{p}$, where n and $\tilde{n}$ denote the noise power vectors in the original and the dual topology network, respectively.*

Due to this theorem, in order to improve packet throughput, it is reasonable to select the transmit beamforming vectors $\{v_i\}_{i \in \mathcal{L}}$ in the original network by viewing them as receive beamforming vectors in the dual topology network, for given transmit beamforming vectors $\{u_i^*\}_{i \in \mathcal{L}}$, and individually optimizing them as in Section 3.1.1. Note that the transmit powers used in the dual network topology need to be appropriately related to the actual transmit powers used in the original network. Therefore, the described transmit beamforming method requires network-wide channel state information and, thus, leads to a centralized implementation.

3.2 Progressive Back-Off Algorithm with Optimum Receive Beamforming (PBOA-ORB)

In this section, a PHY-MAC cross-layer protocol for ad hoc networks described by the model of Section 3.1 is proposed, assuming that nodes employ single-antenna transmission and multiple-antenna reception. The protocol is named PBOA-ORB since it adopts the medium access and power control mechanisms of the PBOA protocol of [45] and integrates them with optimum receive beamforming. The same frame format as in PBOA is assumed and is shown in Fig.3.3. Each frame consists of a contention slot, which is divided into m minislot pairs, and a data slot. The first minislot of each pair is dedicated to the transmission of an RTS packet and the second to the transmission of a CTS packet. Among other fields (e.g., guard times, source and destination MAC
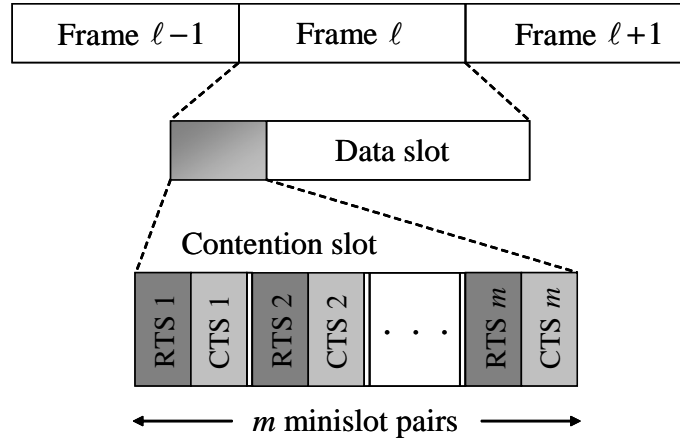
Figure 3.3: Frame format of the PBOA-ORB and PBOA-TORB protocols.

addresses), the RTS and CTS packets contain a training sequence field for the practical implementation of optimum beamforming at the receivers. In addition, the CTS packet contains a power scaling factor field that is used in power control.

3.2.1 Basic Idea

At the beginning of the contention slot, every node with a non-empty packet queue is a *contending* node and will initially contend for the packet at the head of its queue. All the remaining nodes are *silent*. During the contention slot, the goal of the protocol is to determine a subset of contending nodes that will successfully deliver their packet to its destination, once they transmit simultaneously in the subsequent data slot. These nodes are named *locked*. To achieve the above goal in a way that enhances the number of locked nodes (i.e., the spatial reuse), the following mechanisms are employed: 1) *optimum receive beamforming*, so that contending nodes have a better chance to be successful in achieving the SINR threshold γ_T at their intended receiver; 2) *power control*, so that contending nodes which are successful reduce their transmit power, thus causing less interference and increasing the chances of others; 3) *progressive back-off*, so that contending nodes which are unsuccessful quit the contention process, with some probability, to facilitate others; and 4) *non-first-in-first-out (non-FIFO) queueing*, so that contending nodes which are unsuccessful but persist contend for a new packet with a different, possibly more 'favorable', destination.

3.2.2 Protocol Description

The PBOA-ORB protocol is described in more detail as follows.

During the kth RTS minislot:

1) Contending nodes transmit an RTS packet to their intended receiver at maximum power $P_i^{(k)} = P_{\max}$, using only one transmit antenna. Assuming that the first antenna is used, this corresponds to transmit beamforming vector $\boldsymbol{v}_i = [1\ 0 \ldots 0]^T$.

2) Locked nodes transmit an RTS packet to their intended receiver, using only one transmit antenna, at power $P_i^{(k)}$ that was specified by this receiver in a previous CTS minislot.

3) Silent nodes listen. If there is an RTS packet for them, they compute the ORB vector $\boldsymbol{u}_i^{(k)}$, based on the training sequence embedded in the packet, and use it to receive the remainder of the packet at maximum SINR $\gamma_i^{(k)}$.

During the kth CTS minislot:

1) Silent nodes that received an RTS packet from a contending or a locked node with SINR $\gamma_i^{(k)} \geq \gamma_T$ reply with a CTS packet sent at power $\tilde{P}_i^{(k)} = P_{\max}$, using the transmit beamforming vector $\tilde{\boldsymbol{v}}_i^{(k)} = \boldsymbol{u}_i^{(k)*}$. This packet notifies the contending or locked node of the factor $\alpha_i^{(k)} = \min\{1,\ (1+\epsilon)\gamma_T/\gamma_i^{(k)}\}$ by which it must scale its power, where ϵ is a small margin parameter.

2) Contending and locked nodes listen. If there is a CTS packet for them, they compute the ORB vector $\tilde{\boldsymbol{u}}_i^{(k)}$, based on the training sequence embedded in the packet, and use it to receive the remainder of the packet at maximum SINR $\tilde{\gamma}_i^{(k)}$.

At the end of the kth CTS minislot:

1) Contending nodes that successfully received a CTS packet destined for them become locked and scale down their power to $P_i^{(k+1)} = \alpha_i^{(k)} P_i^{(k)}$.

2) Contending nodes that did not receive a CTS packet either persist contending with probability p, or back off and become silent for the rest of the frame with probability $1 - p$. If possible, persisting nodes select from their queue a packet with a *different* destination to contend for, in the next minislot pair (non-FIFO queueing).

3) Locked nodes that successfully received a CTS packet destined for them scale down their power to $P_i^{(k+1)} = \alpha_i^{(k)} P_i^{(k)}$, otherwise they set $P_i^{(k+1)} = P_i^{(k)}$.

During the data slot, locked nodes transmit their data packet, using only one antenna, at the power level specified by the last CTS packet they received. Silent nodes receive the data packet destined for them using the ORB vector $\boldsymbol{u}_i^{(m)}$ that they computed during the last (mth) RTS minislot.

3.2.3   Discussion

Regarding the use of antenna arrays, the following remarks can be made. During an RTS minislot, contending and locked nodes transmit over only one antenna since they lack side information about the channel that would allow them to beamform. Silent nodes, on the other hand, employ optimum receive beamforming by exploiting the training sequence that is embedded in their RTS packet. In accordance with (3.5) and (3.3a), the theoretical expressions for the ORB vector and the corresponding maximum SINR are, respectively,

$$\boldsymbol{u}_i^{(k)} = \frac{\boldsymbol{\Phi}_{I,i}^{(k)^{-1}} \boldsymbol{H}_{ii} \boldsymbol{v}_i}{|\boldsymbol{\Phi}_{I,i}^{(k)^{-1}} \boldsymbol{H}_{ii} \boldsymbol{v}_i|} \tag{3.9}$$

and

$$\gamma_i^{(k)} = \frac{P_i^{(k)} G_{ii} |\boldsymbol{u}_i^{(k)H} \boldsymbol{H}_{ii} \boldsymbol{v}_i|^2}{\displaystyle\sum_{\substack{j \neq i \\ j \in \mathcal{L}^{(k)}}} P_j^{(k)} G_{ij} |\boldsymbol{u}_i^{(k)H} \boldsymbol{H}_{ij} \boldsymbol{v}_j|^2 + \sigma_w^2} \tag{3.10}$$

for interference-plus-noise covariance matrix

$$\boldsymbol{\Phi}_{I,i}^{(k)} = \sum_{\substack{j \neq i \\ j \in \mathcal{L}^{(k)}}} P_j^{(k)} G_{ij} \boldsymbol{H}_{ij} \boldsymbol{v}_j \boldsymbol{v}_j^H \boldsymbol{H}_{ij}^H + \sigma_w^2 \boldsymbol{I}, \tag{3.11}$$

assuming a set $\mathcal{L}^{(k)}$ of active links during the kth RTS minislot. During a CTS minislot, silent nodes transmit while contending and locked nodes receive, hence the link model is the reciprocal of that in Fig. 3.1 and is shown in Fig. 3.2. By virtue of reciprocity, silent nodes employ transmit beamforming using the same weights $\boldsymbol{u}_i^{(k)*}$ that were used for optimum receive beamforming in the previous RTS minislot[1]. In this way, they reduce the interference caused to contending or locked nodes other than their corresponding one. Contending and locked nodes, on the other hand, extract from the training sequence of

---

[1]This heuristic choice of transmit beamforming weights during CTS minislots has been shown, via simulations, to slightly increase network throughput compared to single-antenna transmission.

their CTS packet the receive beamforming vector that maximizes their SINR. Similarly to (3.9) and (3.10), the theoretical expressions for this ORB vector and the maximum SINR are, respectively,

$$\tilde{\boldsymbol{u}}_i^{(k)} = \frac{\tilde{\boldsymbol{\Phi}}_{I,i}^{(k)^{-1}} \boldsymbol{H}_{ii}^T \boldsymbol{u}_i^{(k)*}}{|\tilde{\boldsymbol{\Phi}}_{I,i}^{(k)^{-1}} \boldsymbol{H}_{ii}^T \boldsymbol{u}_i^{(k)*}|} \tag{3.12}$$

and

$$\tilde{\gamma}_i^{(k)} = \frac{\tilde{P}_i^{(k)} G_{ii} |\tilde{\boldsymbol{u}}_i^{(k)H} \boldsymbol{H}_{ii}^T \boldsymbol{u}_i^{(k)*}|^2}{\displaystyle\sum_{\substack{j \neq i \\ j \in \mathcal{S}^{(k)}}} \tilde{P}_j^{(k)} G_{ji} |\tilde{\boldsymbol{u}}_i^{(k)H} \boldsymbol{H}_{ji}^T \boldsymbol{u}_j^{(k)*}|^2 + \sigma_w^2} \tag{3.13a}$$

$$= \frac{P_{\max} G_{ii} |\tilde{\boldsymbol{u}}_i^{(k)H} \boldsymbol{H}_{ii}^T \boldsymbol{u}_i^{(k)*}|^2}{\displaystyle\sum_{\substack{j \neq i \\ j \in \mathcal{S}^{(k)}}} P_{\max} G_{ji} |\tilde{\boldsymbol{u}}_i^{(k)H} \boldsymbol{H}_{ji}^T \boldsymbol{u}_j^{(k)*}|^2 + \sigma_w^2} \tag{3.13b}$$

where

$$\tilde{\boldsymbol{\Phi}}_{I,i}^{(k)} = \sum_{\substack{j \neq i \\ j \in \mathcal{S}^{(k)}}} \tilde{P}_j^{(k)} G_{ji} \boldsymbol{H}_{ji}^T \boldsymbol{u}_j^{(k)*} \boldsymbol{u}_j^{(k)T} \boldsymbol{H}_{ji}^* + \sigma_w^2 \boldsymbol{I} \tag{3.14a}$$

$$= \sum_{\substack{j \neq i \\ j \in \mathcal{S}^{(k)}}} P_{\max} G_{ji} \boldsymbol{H}_{ji}^T \boldsymbol{u}_j^{(k)*} \boldsymbol{u}_j^{(k)T} \boldsymbol{H}_{ji}^* + \sigma_w^2 \boldsymbol{I} \tag{3.14b}$$

is the interference-plus-noise covariance matrix corresponding to a set $\mathcal{S}^{(k)}$ of active links during the kth CTS minislot.

Finally, by design, the PBOA-ORB protocol satisfies the following proposition, which is mathematically proved in Appendix C.

Proposition 1. *Assuming channel time invariance, the PBOA-ORB protocol guarantees that, if a contending node delivers an RTS packet to its intended receiver at SINR $\gamma_i^{(k)} \geq \gamma_T$ in the kth minislot, and receives a CTS packet in response, it will also deliver an RTS packet at SINR $\gamma_i^{(k+1)} \geq \gamma_T$ in the $(k+1)$th minislot.*

Essentially, this proposition implies that a contending node which becomes locked is guaranteed to successfully deliver its subsequent RTS packets and, eventually, its data packet to the intended receiver, provided that the channel remains fixed for the duration of a frame. Since this condition is, often, not satisfied in practice, the margin parameter ϵ is introduced in the expression of the power scaling factor $\alpha_i^{(k)}$ to compensate for minor channel fluctuations or SINR estimation inaccuracies (e.g., due to imperfect beamforming) that could possibly occur.

3.3 Progressive Back-Off Algorithm with Transmit and Optimum Receive Beamforming (PBOA-TORB)

The PBOA-ORB protocol does not fully exploit the multiple-antenna capability of the nodes as it considers only receive beamforming. Transmit beamforming offers the potential to further enhance spatial reuse by increasing the number of locked nodes in a contention period. This can be achieved if locked nodes adjust (in addition to their transmit power) their transmit beamforming vectors so that: 1) the interference they incur is reduced to improve the chances of other nodes to access the channel; and 2) successful transmission of packets is guaranteed, under the assumption of channel time invariance. The PBOA-TORB protocol presented in this section incorporates transmit beamforming into the contention resolution mechanisms of PBOA-ORB in a way that satisfies the above design requirements.

3.3.1 Basic Idea

The PBOA-TORB protocol, which uses the same frame format as PBOA-ORB, exploits the fact that the network topology during a CTS minislot is, essentially, the dual of the network topology during an RTS minislot due to channel reciprocity. Hence, by the Network Duality Theorem, locked nodes can employ the optimum beamforming weights that are used to receive a CTS packet as transmit beamforming weights to transmit a subsequent RTS packet. This packet will be delivered at SINR greater than the threshold γ_T as long as the CTS packet is received at SINR greater than the threshold, provided that the corresponding transmit powers are appropriately related as dictated by the theorem. This implies that both RTS and CTS transmissions need to be power controlled in a coordinated way. Therefore, PBOA-TORB requires network-wide channel state information and is a centralized protocol. In fact, it is rather challenging to devise distributed protocols that satisfy the same design requirements as PBOA-TORB. Even if such protocols are feasible, it is expected that their performance will be upper bounded by the performance of PBOA-TORB.

3.3.2 Protocol Description

The PBOA-TORB protocol is described in more detail as follows.

During the kth RTS minislot:

1) Contending nodes transmit an RTS packet to their intended receiver at maximum power $P_i^{(k)} = P_{\max}$, using the transmit beamforming vector $\boldsymbol{v}_i^{(k)} = [1\,0\ldots 0]^T$.

2) Locked nodes transmit an RTS packet to their intended receiver using power $P_i^{(k)}$ and transmit beamforming vector $\boldsymbol{v}_i^{(k)}$ that were specified in a previous CTS minislot.

3) Silent nodes listen. If there is an RTS packet for them, they compute the ORB vector $\boldsymbol{u}_i^{(k)}$ and use it to receive the packet at maximum SINR $\gamma_i^{(k)}$.

   At the end of the kth RTS minislot:

1) Silent nodes that successfully received an RTS packet from a contending or locked node

   (a) compute the SINR $\gamma_{i,out}^{(k)}$ at which they would receive their RTS packet, using the beamforming vector $\boldsymbol{u}_i^{(k)}$, in case the transmitting nodes updated their power to $P_{i,out}^{(k)} = P_i^{(k)} \min\{1,\, (1+\epsilon)\gamma_T/\gamma_i^{(k)}\}$, and

   (b) compute the transmit power $\tilde{P}_i^{(k)}$ that they will use in the subsequent CTS minislot by means of the Network Duality Theorem for SINR values $\{\gamma_{i,out}^{(k)}\}$.

   During the kth CTS minislot:

1) Silent nodes that successfully received an RTS packet reply with a CTS packet that is sent at power $\tilde{P}_i^{(k)}$, using the transmit beamforming vector $\tilde{\boldsymbol{v}}_i^{(k)} = \boldsymbol{u}_i^{(k)*}$.

2) Contending and locked nodes listen. If there is a CTS packet for them, they compute the ORB vector $\tilde{\boldsymbol{u}}_i^{(k)}$ and use it to receive the packet at maximum SINR $\tilde{\gamma}_i^{(k)}$.

   At the end of the kth CTS minislot:

1) Contending nodes that successfully received a CTS packet destined for them become locked and

   (a) compute the SINR $\tilde{\gamma}_{i,out}^{(k)}$ at which they would receive their CTS packet, using the beamforming vector $\tilde{\boldsymbol{u}}_i^{(k)}$, in case the silent nodes updated their transmit power to $\tilde{P}_{i,out}^{(k)} = \tilde{P}_i^{(k)} \min\{1,\, (1+\epsilon)\gamma_T/\tilde{\gamma}_i^{(k)}\}$,

(b) update their transmit power to $P_i^{(k+1)}$, that is obtained by means of the Network Duality Theorem for SINR values $\{\tilde{\gamma}_{i,out}^{(k)}\}$, and their transmit beam-forming vector to $\boldsymbol{v}_i^{(k+1)} = \tilde{\boldsymbol{u}}_i^{(k)*}$.

2) Contending nodes that did not receive a CTS packet either persist contending with probability p or back off and become silent for the rest of the frame with probability $1-p$. If possible, persisting nodes select from their queue a packet with a different destination to contend for, in the next minislot pair.

3) Locked nodes that successfully received a CTS packet destined for them follow the same steps a) and b) as successfully contending nodes, otherwise they set $P_i^{(k+1)} = P_i^{(k)}$ and $\boldsymbol{v}_i^{(k+1)} = \boldsymbol{v}_i^{(k)}$.

During the data slot, locked nodes transmit their data packet using the most recent power and transmit beamforming vector updates. Silent nodes receive the data packet destined for them using the ORB vector $\boldsymbol{u}_i^{(m)}$ that they computed during the last (mth) RTS minislot.

3.3.3 Discussion

During an RTS minislot, silent nodes employ optimum receive beamforming to maximize their SINR, in a similar fashion as in the PBOA-ORB protocol. The theoretical expressions for the ORB vector $\boldsymbol{u}_i^{(k)}$ and the maximum SINR $\gamma_i^{(k)}$ are provided by (3.9) and (3.10), respectively, after replacing $\boldsymbol{v}_i$ with $\boldsymbol{v}_i^{(k)}$. Depending on the maximum SINR value relative to the threshold γ_T, it is possible to divide the set of active RTS links $\mathcal{L}^{(k)}$ into two disjoint subsets; namely, the subset of successful links $\mathcal{S}^{(k)}$ (for which $\gamma_i^{(k)} \geq \gamma_T$) and the subset of unsuccessful links $\bar{\mathcal{S}}^{(k)}$ (for which $\gamma_i^{(k)} < \gamma_T$). In this case, the SINR expression for the ith successful link can be written as

$$\gamma_i^{(k)} = \frac{P_i^{(k)} G_{ii} |\boldsymbol{u}_i^{(k)H} \boldsymbol{H}_{ii} \boldsymbol{v}_i^{(k)}|^2}{\displaystyle\sum_{\substack{j \neq i \\ j \in \mathcal{S}^{(k)}}} P_j^{(k)} G_{ij} |\boldsymbol{u}_i^{(k)H} \boldsymbol{H}_{ij} \boldsymbol{v}_j^{(k)}|^2 + \sum_{\ell \in \bar{\mathcal{S}}^{(k)}} P_\ell^{(k)} G_{i\ell} |\boldsymbol{u}_i^{(k)H} \boldsymbol{H}_{i\ell} \boldsymbol{v}_\ell^{(k)}|^2 + \sigma_w^2} \tag{3.15a}$$

$$= \frac{P_i^{(k)} G_{ii} |\boldsymbol{u}_i^{(k)H} \boldsymbol{H}_{ii} \boldsymbol{v}_i^{(k)}|^2}{\displaystyle\sum_{\substack{j \neq i \\ j \in \mathcal{S}^{(k)}}} P_j^{(k)} G_{ij} |\boldsymbol{u}_i^{(k)H} \boldsymbol{H}_{ij} \boldsymbol{v}_j^{(k)}|^2 + n_i^{(k)}} \geq \gamma_T \tag{3.15b}$$

where

$$n_i^{(k)} = \sum_{\ell \in \bar{\mathcal{S}}^{(k)}} P_\ell^{(k)} G_{i\ell} |\boldsymbol{u}_i^{(k)H} \boldsymbol{H}_{i\ell} \boldsymbol{v}_\ell^{(k)}|^2 + \sigma_w^2 \tag{3.16}$$

denotes the effective 'noise' power due to thermal noise and interference from unsuccessfully contending nodes. After receiving an RTS packet, silent nodes determine the power $\tilde{P}_i^{(k)}$ that they will use to transmit a CTS packet, in the subsequent minislot, following a two-step process. First, the SINR that would be achieved if the contending and locked nodes reduced their power to $P_{i,out}^{(k)} = P_i^{(k)} \min\{1, (1+\epsilon)\gamma_T/\gamma_i^{(k)}\}$, while the transmit and receive beamforming vectors remained fixed to $\boldsymbol{v}_i^{(k)}$ and $\boldsymbol{u}_i^{(k)}$, respectively, is computed as

$$\gamma_{i,out}^{(k)} = \frac{P_{i,out}^{(k)} G_{ii} |\boldsymbol{u}_i^{(k)H} \boldsymbol{H}_{ii} \boldsymbol{v}_i^{(k)}|^2}{\displaystyle\sum_{\substack{j \neq i \\ j \in \mathcal{S}^{(k)}}} P_{j,out}^{(k)} G_{ij} |\boldsymbol{u}_i^{(k)H} \boldsymbol{H}_{ij} \boldsymbol{v}_j^{(k)}|^2 + n_i^{(k)}}. \tag{3.17}$$

It is shown that $\gamma_{i,out}^{(k)} \geq \gamma_T$ for $i \in \mathcal{S}^{(k)}$ in Appendix D. Second, the Network Duality Theorem is invoked. Considering only the set of successful RTS links $\mathcal{S}^{(k)}$, the network topology in the kth CTS minislot is the dual of the network topology in the kth RTS minislot due to channel reciprocity. Consequently, there exist power levels $\tilde{P}_i^{(k)} \geq 0$, which, if used by silent nodes in conjunction with transmit beamforming vectors $\boldsymbol{u}_i^{(k)*}$ and receive beamforming vectors $\boldsymbol{v}_i^{(k)*}$, achieve SINR $\gamma_{i,out}^{(k)}$ at the corresponding contending or locked nodes. For the ith link in this dual network topology (see Fig 3.2), it is

$$\gamma_{i,out}^{(k)} = \frac{\tilde{P}_i^{(k)} G_{ii} |\boldsymbol{v}_i^{(k)T} \boldsymbol{H}_{ii}^T \boldsymbol{u}_i^{(k)*}|^2}{\displaystyle\sum_{\substack{j \neq i \\ j \in \mathcal{S}^{(k)}}} \tilde{P}_j^{(k)} G_{ji} |\boldsymbol{v}_i^{(k)T} \boldsymbol{H}_{ji}^T \boldsymbol{u}_j^{(k)*}|^2 + \sigma_w^2} \tag{3.18a}$$

$$= \frac{\tilde{P}_i^{(k)} G_{ii} |\boldsymbol{u}_i^{(k)H} \boldsymbol{H}_{ii} \boldsymbol{v}_i^{(k)}|^2}{\displaystyle\sum_{\substack{j \neq i \\ j \in \mathcal{S}^{(k)}}} \tilde{P}_j^{(k)} G_{ji} |\boldsymbol{u}_j^{(k)H} \boldsymbol{H}_{ji} \boldsymbol{v}_i^{(k)}|^2 + \sigma_w^2} \tag{3.18b}$$

which can also be written as

$$\tilde{P}_i^{(k)} - \frac{\gamma_{i,out}^{(k)}}{g_{ii}^{(k)}} \sum_{\substack{j \neq i \\ j \in \mathcal{S}^{(k)}}} g_{ji}^{(k)} \tilde{P}_j^{(k)} = \frac{\gamma_{i,out}^{(k)}}{g_{ii}^{(k)}} \sigma_w^2 \tag{3.19}$$

by defining $g_{ij}^{(k)} = G_{ij} |\boldsymbol{u}_i^{(k)H} \boldsymbol{H}_{ij} \boldsymbol{v}_j^{(k)}|^2$. Writing similar equations for all links in $\mathcal{S}^{(k)}$ and stacking them, in vector form, results in

$$\left(\boldsymbol{I} - \boldsymbol{D}^{(k)} \boldsymbol{A}_G^{(k)T}\right) \tilde{\boldsymbol{p}}^{(k)} = \sigma_w^2 \boldsymbol{D}^{(k)} \boldsymbol{1},$$

hence,

$$\tilde{\boldsymbol{p}}^{(k)} = \sigma_w^2 \left(\boldsymbol{I} - \boldsymbol{D}^{(k)} \boldsymbol{A}_G^{(k)T}\right)^{-1} \boldsymbol{D}^{(k)} \boldsymbol{1} \tag{3.20}$$

where $\tilde{\boldsymbol{p}}^{(k)}$ is a vector with elements $\tilde{P}_i^{(k)}$, $\mathbf{1}$ is a vector with all elements equal to 1, $\boldsymbol{D}^{(k)}$ is a diagonal matrix with elements $D_{i,i}^{(k)} = \gamma_{i,out}^{(k)}/g_{ii}^{(k)}$, and $\boldsymbol{A}_G^{(k)}$ is a matrix with elements $A_{G\,i,j}^{(k)} = (1 - \delta_{i,j})g_{ij}^{(k)}$.

During a CTS minislot, silent nodes that successfully received an RTS packet transmit a CTS packet using power $\tilde{P}_i^{(k)}$, provided by the corresponding element of $\tilde{\boldsymbol{p}}^{(k)}$, and transmit beamforming vector $\tilde{\boldsymbol{v}}_i^{(k)} = \boldsymbol{u}_i^{(k)*}$. Contending and locked nodes, on the other hand, employ the ORB vector $\tilde{\boldsymbol{u}}_i^{(k)}$ of (3.12) to achieve maximum SINR $\tilde{\gamma}_i^{(k)}$ given by (3.13a). It is shown that $\tilde{\gamma}_i^{(k)} \geq \gamma_T$ in Appendix D; therefore, successful reception of the CTS packets is guaranteed by the protocol, as stated in the following remark.

Remark 1. *Silent nodes that receive an RTS packet from a contending or locked node at SINR $\gamma_i^{(k)} \geq \gamma_T$ are guaranteed to deliver their CTS packet to that node at SINR $\tilde{\gamma}_i^{(k)} \geq \gamma_T$.*

After receiving a CTS packet, contending and locked nodes update their transmit power based on a two-step process similar to that followed by silent nodes at the end of an RTS minislot. First, the SINR that would be achieved if the transmitting silent nodes reduced their power to $\tilde{P}_{i,out}^{(k)} = \tilde{P}_i^{(k)} \min\{1, (1 + \epsilon)\gamma_T/\tilde{\gamma}_i^{(k)}\}$, while the transmit and receive beamforming vectors remained fixed to $\boldsymbol{u}_i^{(k)*}$ and $\tilde{\boldsymbol{u}}_i^{(k)}$, respectively, is computed according to

$$\tilde{\gamma}_{i,out}^{(k)} = \frac{\tilde{P}_{i,out}^{(k)} G_{ii} |\tilde{\boldsymbol{u}}_i^{(k)H} \boldsymbol{H}_{ii}^T \boldsymbol{u}_i^{(k)*}|^2}{\displaystyle\sum_{\substack{j \neq i \\ j \in \mathcal{S}^{(k)}}} \tilde{P}_{j,out}^{(k)} G_{ji} |\tilde{\boldsymbol{u}}_i^{(k)H} \boldsymbol{H}_{ji}^T \boldsymbol{u}_j^{(k)*}|^2 + \sigma_w^2}. \tag{3.21}$$

It is shown that $\tilde{\gamma}_{i,out}^{(k)} \geq \gamma_T$, in the same way as $\gamma_{i,out}^{(k)} \geq \gamma_T$, in Appendix D. Then, the Network Duality Theorem is invoked. Remark 1 implies that links which are successful in the kth RTS minislot will be active in the $(k+1)$th RTS minislot. Considering only this set of links $\mathcal{S}^{(k)}$, the network topology during the $(k+1)$th RTS minislot is the dual of the network topology during the kth CTS minislot. Consequently, there exist power levels $P_i^{(k+1)} \geq 0$, which, if used by the transmitting nodes in conjunction with transmit beamforming vectors $\tilde{\boldsymbol{u}}_i^{(k)*}$ and receive beamforming vectors $\boldsymbol{u}_i^{(k)}$, achieve SINR $\tilde{\gamma}_{i,out}^{(k)}$ at the corresponding silent nodes. The worst interference scenario occurs when all active links in the kth RTS minislot are also active in the $(k+1)$th RTS minislot (i.e., when *all* unsuccessfully contending nodes persist contending rather than back off). In this case,

for the ith RTS link, it is

$$\tilde{\gamma}_{i,out}^{(k)} = \frac{P_i^{(k+1)} G_{ii} |\boldsymbol{u}_i^{(k)H} \boldsymbol{H}_{ii} \tilde{\boldsymbol{u}}_i^{(k)*}|^2}{\displaystyle\sum_{\substack{j \neq i \\ j \in \mathcal{S}^{(k)}}} P_j^{(k+1)} G_{ij} |\boldsymbol{u}_i^{(k)H} \boldsymbol{H}_{ij} \tilde{\boldsymbol{u}}_j^{(k)*}|^2 + \underbrace{\displaystyle\sum_{\ell \in \bar{\mathcal{S}}^{(k)}} P_\ell^{(k)} G_{i\ell} |\boldsymbol{u}_i^{(k)H} \boldsymbol{H}_{i\ell} \boldsymbol{v}_\ell^{(k)}|^2 + \sigma_w^2}_{n_i^{(k)}}} \quad (3.22)$$

which can be written as

$$P_i^{(k+1)} - \frac{\tilde{\gamma}_{i,out}^{(k)}}{\tilde{g}_{ii}^{(k)}} \sum_{\substack{j \neq i \\ j \in \mathcal{S}^{(k)}}} \tilde{g}_{ji}^{(k)} P_j^{(k+1)} = \frac{\tilde{\gamma}_{i,out}^{(k)}}{\tilde{g}_{ii}^{(k)}} n_i^{(k)} \quad (3.23)$$

by defining $\tilde{g}_{ij}^{(k)} = G_{ji} |\tilde{\boldsymbol{u}}_i^{(k)H} \boldsymbol{H}_{ji}^T \boldsymbol{u}_j^{(k)*}|^2$. Stacking similar equations for all links in $\mathcal{S}^{(k)}$, in vector form, results in

$$\big(\boldsymbol{I} - \tilde{\boldsymbol{D}}^{(k)} \tilde{\boldsymbol{A}}_G^{(k)T}\big) \boldsymbol{p}^{(k+1)} = \tilde{\boldsymbol{D}}^{(k)} \boldsymbol{n}^{(k)},$$

hence

$$\boldsymbol{p}^{(k+1)} = \big(\boldsymbol{I} - \tilde{\boldsymbol{D}}^{(k)} \tilde{\boldsymbol{A}}_G^{(k)T}\big)^{-1} \tilde{\boldsymbol{D}}^{(k)} \boldsymbol{n}^{(k)}, \quad (3.24)$$

where $\boldsymbol{p}^{(k+1)}$ is a vector with elements $P_i^{(k+1)}$, $\boldsymbol{n}^{(k)}$ is a vector with elements $n_i^{(k)}$, $\tilde{\boldsymbol{D}}^{(k)}$ is a diagonal matrix with elements $\tilde{D}_{i,i}^{(k)} = \tilde{\gamma}_{i,out}^{(k)}/\tilde{g}_{ii}^{(k)}$, and $\tilde{\boldsymbol{A}}_G^{(k)}$ is a matrix with elements $\tilde{A}_{G\,i,j}^{(k)} = (1 - \delta_{i,j})\tilde{g}_{ij}^{(k)}$.

In a similar fashion to PBOA-ORB, the PBOA-TORB protocol is designed to guarantee that, once a contending node becomes locked, it will successfully deliver subsequent RTS packets and its data packet to the intended receiver. This property is formalized in the following proposition, which is mathematically proved in Appendix D.

Proposition 2. *Assuming channel time invariance, the PBOA-TORB protocol guarantees that, if a contending node delivers an RTS packet to its intended receiver at SINR $\gamma_i^{(k)} \geq \gamma_T$ in the kth minislot, and receives a CTS packet in response, it will also deliver an RTS packet at SINR $\gamma_i^{(k+1)} \geq \gamma_T$ in the $(k+1)$th minislot.*

3.3.4 Maximum Power Constraint Considerations

The presentation of the PBOA-TORB protocol in the previous Sections has neglected the fact that the available power per packet transmission is constrained by $P_{\max}$ at each node. Clearly, there is no guarantee that the CTS transmit power levels obtained by (3.20) or the updated RTS transmit power levels obtained by (3.24) will satisfy

$\tilde{P}_i^{(k)} \le P_{\max}$ or $P_i^{(k+1)} \le P_{\max}$, respectively. Since this is undesirable in practical applications, the protocol is modified to account for the maximum power constraint, while still meeting the design objective of Proposition 2, as described below.

First, the case where the CTS transmit powers obtained from (3.20) violate the maximum power constraint is considered. This is mathematically modeled as

$$\max_{i \in \mathcal{S}^{(k)}} \tilde{P}_i^{(k)} = \left(1 + \tilde{\beta}^{(k)}\right) P_{\max}$$

for some $\tilde{\beta}^{(k)} > 0$. In this case, silent nodes transmit at power $\tilde{P}_i^{(k)\prime} = \frac{\tilde{P}_i^{(k)}}{1 + \tilde{\beta}^{(k)}} \le P_{\max}$ rather than $\tilde{P}_i^{(k)}$, in the kth CTS minislot, and the SINR achieved at the corresponding contending or locked node, after optimum receive beamforming with vector $\tilde{\boldsymbol{u}}_i^{(k)}$, is

$$\tilde{\gamma}_i^{(k)\prime} = \frac{\tilde{P}_i^{(k)\prime} G_{ii} |\tilde{\boldsymbol{u}}_i^{(k)H} \boldsymbol{H}_{ii}^T \boldsymbol{u}_i^{(k)*}|^2}{\displaystyle\sum_{\substack{j \ne i \\ j \in \mathcal{S}^{(k)}}} \tilde{P}_j^{(k)\prime} G_{ji} |\tilde{\boldsymbol{u}}_i^{(k)H} \boldsymbol{H}_{ji}^T \boldsymbol{u}_j^{(k)*}|^2 + \sigma_w^2} \tag{3.25a}$$

$$\ge \frac{\tilde{P}_i^{(k)\prime} G_{ii} |\boldsymbol{v}_i^{(k)T} \boldsymbol{H}_{ii}^T \boldsymbol{u}_i^{(k)*}|^2}{\displaystyle\sum_{\substack{j \ne i \\ j \in \mathcal{S}^{(k)}}} \tilde{P}_j^{(k)\prime} G_{ji} |\boldsymbol{v}_i^{(k)T} \boldsymbol{H}_{ji}^T \boldsymbol{u}_j^{(k)*}|^2 + \sigma_w^2} \tag{3.25b}$$

$$= \frac{\tilde{P}_i^{(k)} G_{ii} |\boldsymbol{u}_i^{(k)H} \boldsymbol{H}_{ii} \boldsymbol{v}_i^{(k)}|^2}{\displaystyle\sum_{\substack{j \ne i \\ j \in \mathcal{S}^{(k)}}} \tilde{P}_j^{(k)} G_{ji} |\boldsymbol{u}_j^{(k)H} \boldsymbol{H}_{ji} \boldsymbol{v}_i^{(k)}|^2 + \left(1 + \tilde{\beta}^{(k)}\right)\sigma_w^2} \tag{3.25c}$$

$$= \left(\frac{1}{\gamma_{i,out}^{(k)}} + \frac{\tilde{\beta}^{(k)} \sigma_w^2}{\tilde{P}_i^{(k)} g_{ii}^{(k)}} \right)^{-1} \tag{3.25d}$$

where (3.25b) follows by definition of the ORB vector, and (3.25d) follows due to (3.18b). Based on this expression, if it is

$$\tilde{\beta}^{(k)} \le \min_{i \in \mathcal{S}^{(k)}} \left\{ \frac{\tilde{P}_i^{(k)} g_{ii}^{(k)}}{\sigma_w^2} \left(\frac{1}{\gamma_T} - \frac{1}{\gamma_{i,out}^{(k)}} \right) \right\}, \tag{3.26}$$

successful reception of all CTS packets at SNIR $\tilde{\gamma}_i^{(k)\prime} \ge \gamma_T$ is guaranteed, and Proposition 2 is satisfied, as shown in Appendix D. However, if the above condition is not valid, it is possible that $\tilde{\gamma}_i^{(k)\prime} < \gamma_T$, and one or more CTS packets might be lost. Hence, the PBOA-TORB protocol falls back to PBOA-ORB to ensure that Proposition 2 is satisfied. Specifically, nodes that receive a CTS packet transmit using power $P_i^{(k+1)} = P_i^{(k)} \min\{1, (1+\epsilon)\gamma_T/\gamma_i^{(k)}\}$ and beamforming vector $\boldsymbol{v}_i^{(k)}$ in the $(k+1)$th RTS minislot.

The case where the updated RTS transmit powers obtained by (3.24) violate the maximum power constraint is addressed in a similar way. This is mathematically modeled as

$$\max_{i \in \mathcal{S}^{(k)}} P_i^{(k+1)} = \left(1 + \beta^{(k)}\right) P_{\max}$$

for some $\beta^{(k)} > 0$. Assuming that locked nodes transmit at power $P_i^{(k+1)\prime} = \frac{P_i^{(k+1)}}{1+\beta^{(k)}} \leq P_{\max}$ rather than $P_i^{(k+1)}$, in the $(k+1)$th RTS minislot, it is straightforward to show that the SINR achieved at the corresponding silent node, after optimum receive beamforming, satisfies

$$\gamma_i^{(k+1)\prime} \geq \left(\frac{1}{\tilde{\gamma}_{i,out}^{(k)}} + \frac{\beta^{(k)} n_i^{(k)}}{P_i^{(k+1)} \tilde{g}_{ii}^{(k)}} \right)^{-1} \tag{3.27}$$

by using (3.22) and (D.4). Consequently, if it is

$$\beta^{(k)} \leq \min_{i \in \mathcal{S}^{(k)}} \left\{ \frac{P_i^{(k+1)} \tilde{g}_{ii}^{(k)}}{n_i^{(k)}} \left(\frac{1}{\gamma_T} - \frac{1}{\tilde{\gamma}_{i,out}^{(k)}} \right) \right\}, \tag{3.28}$$

locked nodes are guaranteed to deliver their RTS packets at SINR $\gamma_i^{(k+1)\prime} \geq \gamma_T$, hence the PBOA-TORB protocol is modified so that locked nodes transmit at power $P_i^{(k+1)\prime}$ indeed. Otherwise, it is possible that $\gamma_i^{(k+1)\prime} < \gamma_T$, and the PBOA-TORB protocol falls back to PBOA-ORB, in the sense that locked nodes transmit using power $P_i^{(k+1)} = P_i^{(k)} \min\{1, (1+\epsilon)\gamma_T/\gamma_i^{(k)}\}$ and beamforming vector $\boldsymbol{v}_i^{(k)}$ in the $(k+1)$th RTS minislot.

3.4 Performance Evaluation

3.4.1 Simulation Model

The performance of the protocols described in the previous section is evaluated via simulation over a single-hop ad hoc network that consists of $N = 20$ nodes. These are randomly and uniformly placed in a 100 m $\times$ 100 m square area. The network is *fully connected*, in the sense that the average (with respect to shadowing and fading) SNR of a link between any two nodes exceeds the threshold γ_T. Thus, every node can, at least theoretically, communicate with all other nodes in the absence of interference. This is guaranteed by the following choice of parameter values.

Each node can transmit a packet at any power up to $P_{\max} = 0.2$ W and is subject to noise power $\sigma_n^2 = -114$ dBm while receiving. The power gain between two nodes at

distance d_{ij} is provided by the dual-slope model as

$$G_{ij}(d_{ij}) = \begin{cases} S_{ij} \left(\frac{\lambda_c}{4\pi d_{ij}} \right)^2, & d_{ij} \leq d_o \\ S_{ij} \left(\frac{\lambda_c}{4\pi d_o} \right)^2 \left(\frac{d_o}{d_{ij}} \right)^{\alpha}, & d_{ij} > d_o \end{cases}, \tag{3.29}$$

for lognormal shadowing S_{ij} with 6 dB standard deviation, carrier wavelength $\lambda_c = 0.125$ m (corresponding to carrier frequency $f_c = 2.4$ GHz), path loss exponent $\alpha = 4$, and break-point constant $d_o = 1$ m. The corresponding channel matrix $\boldsymbol{H}_{ij}$ consists of i.i.d. zero-mean and unit-variance circularly symmetric complex Gaussian random entries that vary independently per frame (i.e., fading is quasi-static, flat, Rayleigh distributed, and independent across the antennas). The SINR threshold is set to $\gamma_T = 10$ dB and the power control margin to $\epsilon = 0.01$.

Data traffic in the network is generated according to a Poisson process with aggregate rate λ packets/s. The traffic load is uniform, meaning that each node creates data packets at rate $\lambda/(N(N-1))$ for any other node. Data packets are 10 Kbits long, and nodes can store up to $B = 100$ of them in their queue. RTS and CTS packets are 100 bits long. The transmission rate is fixed to $R = 1$ Mbps, resulting in data slot duration $\tau_D = 10$ ms and RTS-CTS minislot pair duration $\tau_m = 0.2$ ms.

3.4.2 Optimum Persistence Probability

The simulation results presented in the following sections were obtained using the *optimum* value of persistence probability p for the number of contention minislot pairs m considered. Such a value exists since, if p is too small, network throughput decreases as contending nodes back off too 'soon', while, if p is too large, network throughput decreases as contention cannot not resolved. The optimum persistence probability values p_o corresponding to various numbers of minislot pairs were determined by exhaustive simulation search for both PBOA-ORB and PBOA-TORB protocols. Indicatively, some of these values are reported in Tables 3.1 and 3.2 for $M = 1$, 2, 3, and 4 antennas per node. It is observed that p_o increases with the number of minislots as well as the number of antennas. In the first case, contention is resolved over more minislots while, in the second case, higher levels of contention can be sustained; hence, in terms of throughput, it is better for nodes to be more persistent and gradually back off.

Table 3.1: Optimum persistence probability values for the PBOA-ORB protocol.

m	p_o			
	$M = 1$	$M = 2$	$M = 3$	$M = 4$
8	0.600	0.650	0.700	0.750
9	0.650	0.700	0.725	0.750
10	0.650	0.700	0.750	0.775
11	0.700	0.725	0.775	0.800
12	0.700	0.750	0.800	0.825
13	0.725	0.775	0.800	0.825
14	0.750	0.800	0.825	0.825
15	0.750	0.800	0.825	0.850
16	0.775	0.800	0.850	0.850
17	0.800	0.825	0.850	0.850
18	0.800	0.825	0.850	0.875

Table 3.2: Optimum persistence probability values for the PBOA-TORB protocol.

m	p_o			
	$M = 1$	$M = 2$	$M = 3$	$M = 4$
8	0.600	0.650	0.725	0.750
9	0.650	0.700	0.750	0.775
10	0.650	0.725	0.775	0.800
11	0.700	0.750	0.775	0.825
12	0.700	0.775	0.800	0.825
13	0.725	0.775	0.800	0.850
14	0.750	0.800	0.825	0.850
15	0.750	0.800	0.825	0.850
16	0.775	0.825	0.850	0.875
17	0.800	0.825	0.850	0.875
18	0.800	0.825	0.850	0.875

3.4.3   Aggregate Throughput

In this section, the performance of the proposed protocols is evaluated in terms of aggregate throughput for $M = 1$, 2, 3, and 4 antennas per node. Aggregate throughput

is defined as the average total number of received data bits per time unit and is expressed as

$$T(\lambda) = T_P(\lambda)R\frac{\tau_D}{m\tau_m + \tau_D} \tag{3.30}$$

where $T_P(\lambda)$ denotes the average total number of successfully received data packets per frame that is obtained by simulations for aggregate traffic rate λ. Note that, for $M = 1$ antenna, the PBOA-ORB protocol coincides with the PBOA protocol of [45], so comparison between the two is straightforward.

Fig. 3.4 illustrates the aggregate throughput of the PBOA-ORB protocol versus the offered traffic load for $m = 13$ minislot pairs. As the traffic load increases, the throughput increases in proportion, up to a point where node queues fill up due to high contention, and any extra load causes them to overflow, leading to throughput saturation. Multiple antennas enable nodes to cope with higher levels of contention thanks to the interference suppression and multi-packet reception capabilities offered by optimum receive beamforming. As a result, PBOA-ORB achieves higher throughput than PBOA, which is roughly proportional to the number of antennas. Similar trends are observed for the PBOA-TORB protocol in Fig. 3.5, where the PBOA-ORB curves are also plotted for comparison. Transmit beamforming allows for even higher levels of contention due to interference avoidance. Thus, PBOA-TORB achieves a throughput gain over PBOA-ORB at high traffic loads, which increases with the number of antennas.

In Fig. 3.6, the maximum aggregate throughput is plotted as a function of the number of minislot pairs m for the PBOA-ORB protocol. In this chapter, maximum aggregate throughput is defined so that *at most* 1% of the generated packets of any source-destination node pair are discarded due to queue overflow, and it corresponds to a point near the 'knee' of the curves in Fig. 3.4. The throughput increases with m up to a value m_o, above which any throughput gain due to contention resolution over more minislot pairs is outweighed by the overhead that they incur. The optimum operation points (m_o, T_o) are marked with crosses on the curves. Based on the corresponding values, it is deduced that: 1) the protocol overhead, expressed by m_o, is a non-increasing function of the number of antennas; and 2) the peak throughput T_o increases linearly (at very good accuracy) with the number of antennas, as depicted in Fig. 3.9. This is in agreement with the results of [23], where it is theoretically shown that linear throughput increase is feasible in an ad hoc network with nodes that employ single-antenna transmission and MMSE receive beamforming. As a final observation, the PBOA-ORB protocol is quite
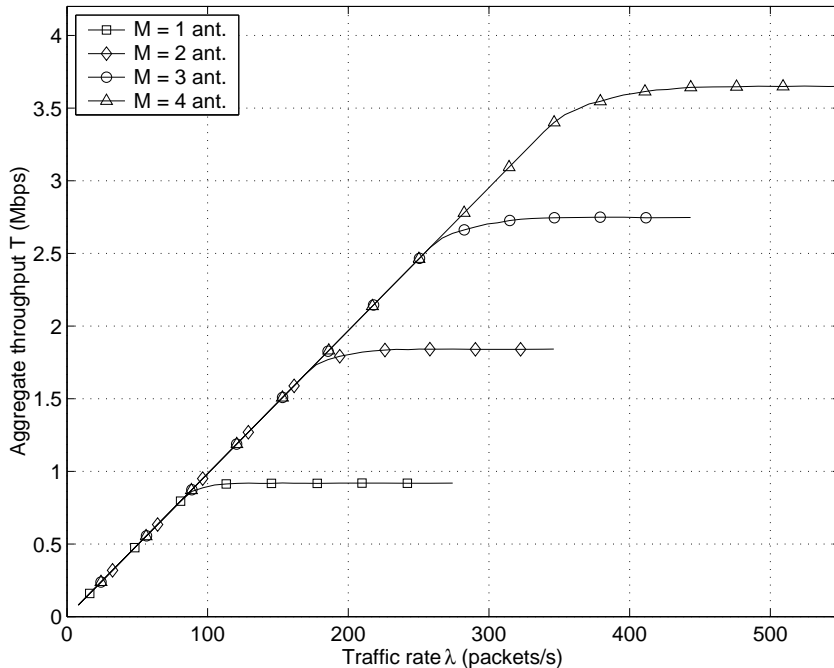
Figure 3.4: Aggregate throughput versus offered traffic load for the PBOA-ORB protocol, assuming $m = 13$ minislot pairs and optimum persistence probability p_o obtained from Table 3.1.

robust to the choice of m since more than 94% of the peak throughput is achieved for $8 \leq m \leq 16$.

Fig. 3.7 illustrates the effect of power control on the maximum aggregate throughput of PBOA-ORB by juxtaposing the curves of Fig. 3.6 against similar curves obtained for the case where no power control is used (i.e. nodes always transmit at maximum power $P_{\max}$). Two main conclusions can be drawn from this figure. First, in the absence of power control, the maximum aggregate throughput decreases. It also obtains its peak value for a smaller number of minislot pairs, compared to the original PBOA-ORB protocol, as nodes have now less degrees of freedom to resolve contention. Second, power control, which simply reduces the interference level, contributes less to the overall throughput than optimum receive beamforming, which nulls out interference and allows for multi-packet reception. However, its contribution becomes more significant as the number of antennas increases due to array gain.

In Fig. 3.8, the maximum aggregate throughput of PBOA-TORB is plotted versus the number of minislot pairs m. The corresponding curves for the PBOA-ORB protocol are also plotted for comparison. For any meaningful value of m, PBOA-TORB
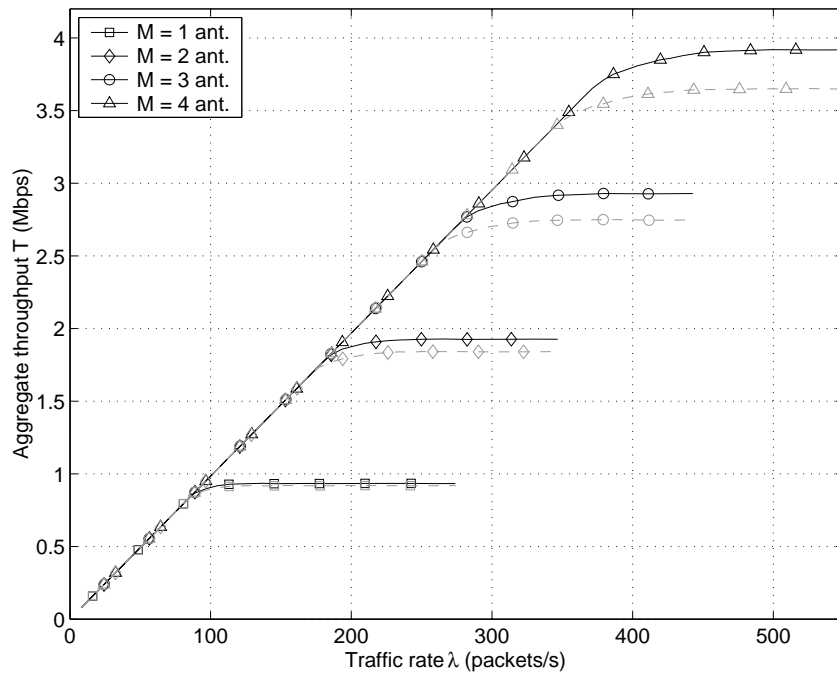
Figure 3.5: Aggregate throughput versus offered traffic load for the PBOA-TORB protocol, assuming $m = 13$ minislot pairs and optimum persistence probability p_o obtained from Table 3.2. Dashed curves corresponding to the PBOA-ORB protocol are also shown for comparison.
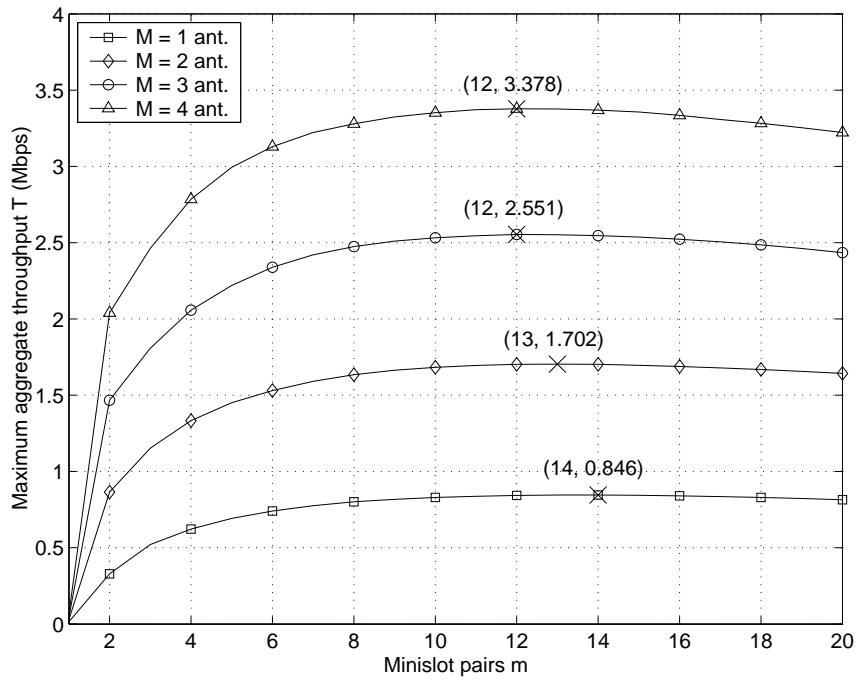
Figure 3.6: Maximum aggregate throughput versus the number of minislot pairs m for the PBOA-ORB protocol. For each value of m, the corresponding optimum persistence probability p_o from Table 3.1 is used. Optimum points on the curves are marked with crosses.
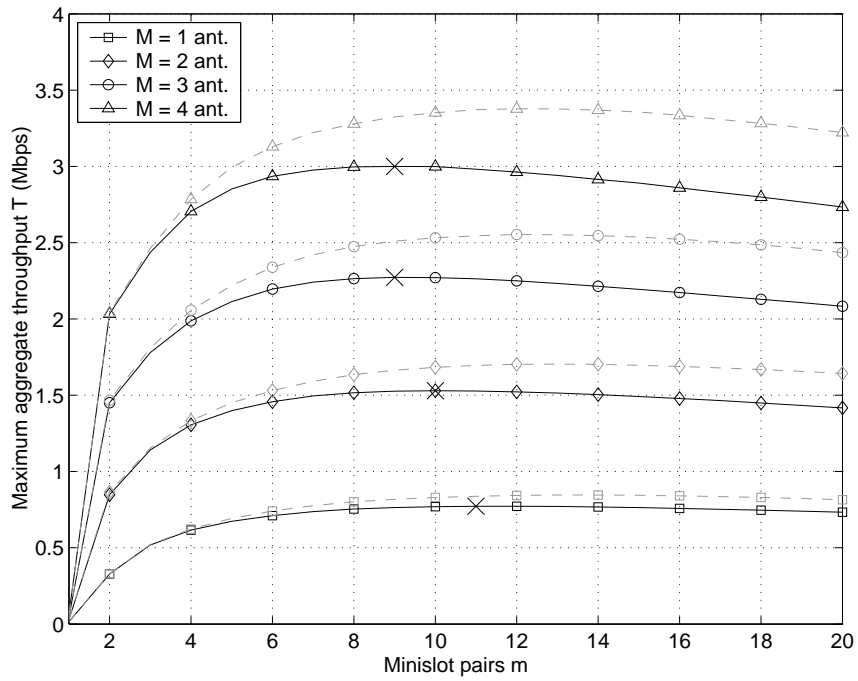
Figure 3.7: Maximum aggregate throughput versus the number of minislot pairs m for the PBOA-ORB protocol with no power control. Dashed curves correspond to the original PBOA-ORB protocol. For each value of m, the optimum persistence probability p_o is used.
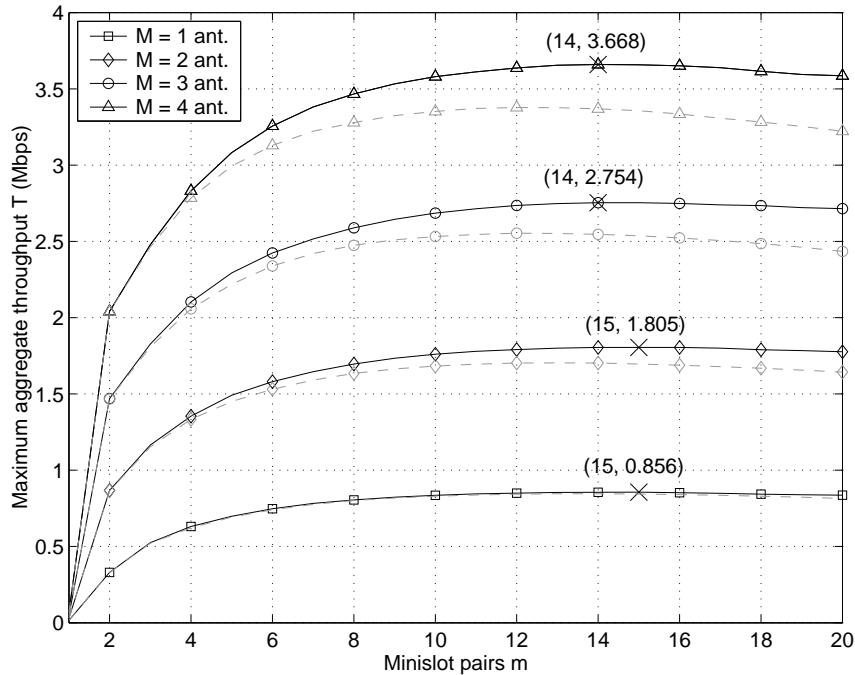
Figure 3.8: Maximum aggregate throughput versus the number of minislot pairs m for the PBOA-TORB protocol. For each value of m, the corresponding optimum persistence probability p_o from Table 3.2 is used. Dashed curves correspond to the PBOA-ORB protocol.

achieves higher throughput than PBOA-ORB by virtue of transmit beamforming. In fact, its peak throughput increases faster than linearly with the number of antennas, as shown in Fig. 3.9. From both figures, it is obvious that the throughput gain due to PBOA-TORB is rather incremental (e.g., 8.6% for $M = 4$ antennas) despite the increased complexity and centralized nature of the protocol. This result can be explained as follows. In both PBOA-ORB and PBOA-TORB protocols, optimum receive beamforming utilizes a fraction of the spatial degrees of freedom at silent nodes to improve the desired signal, via array gain, and the remaining fraction to suppress interference from nodes other than the node of interest. In this way, it directly enhances spatial reuse and contributes the main bulk of network throughput. In PBOA-TORB, transmit beamforming further improves the desired signal, via extra array gain, and also reduces the interference perceived at silent nodes. In so doing, it facilitates optimum receive beamforming and allows for a larger fraction of spatial degrees of freedom to be used for interference suppression; hence, it indirectly enhances spatial reuse and has a smaller contribution to network throughput.
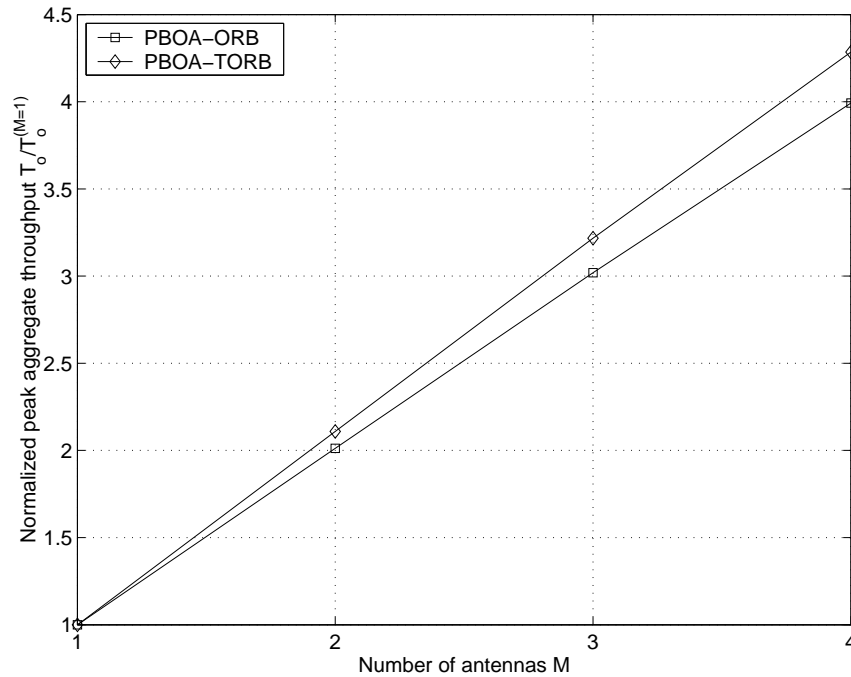
Figure 3.9: Normalized peak aggregate throughput versus the number of antennas M for the PBOA-ORB and PBOA-TORB protocols. Normalization is performed by dividing with the peak aggregate throughput for $M = 1$ antenna.

3.4.4 Energy Efficiency

In Fig. 3.10, the average energy consumed per data packet transmission is plotted versus the aggregate throughput for the PBOA-ORB protocol, assuming $m = 13$ minislot pairs. As expected, less energy is consumed for a larger number of antennas, hence, PBOA-ORB is more efficient than PBOA. This is explained by the fact that optimum receive beamforming maximizes the SINR, and the resulting SINR improvement is translated into transmit power reduction via power control. Since the maximum SINR increases with the number of antennas due to array gain, the energy consumption decreases. However, it increases with aggregate throughput as higher traffic load causes more interference that needs to be overcome. Fig. 3.11 shows that PBOA-TORB is significantly more energy efficient than PBOA-ORB. In fact, the energy consumption of PBOA-TORB decreases more dramatically with the number of antennas, due to extra array gain offered by transmit beamforming, and increases more smoothly with aggregate throughput. Note that, at low throughput, PBOA-ORB with $M = 4$ antennas and PBOA-TORB with $M = 2$ antennas spend similar average energy per data packet due

Figure 3.10: Average energy consumed per data packet versus aggregate throughput for the PBOA-ORB protocol, assuming $m = 13$ minislot pairs and optimum persistence probability p_o obtained from Table 3.1.

to similar array gain.

3.5   Acknowledgement

Chapter 3, in part, is a reprint of the material as it appears in I. Spyropoulos and J. R. Zeidler, "A PHY-MAC Cross-Layer Protocol for Ad Hoc Networks with Multiple-Antenna Nodes," *Proceedings of IEEE International Conference on Communications (ICC)*, Dresden, Germany, June 2009. Additionally, it is currently being prepared for submission for publication of the material as I. Spyropoulos and J. R. Zeidler, "PHY-MAC Cross-Layer Protocols for Ad Hoc Networks with Linear Beamformers," in preparation, 2009. The dissertation author was the primary investigator and author of these papers.
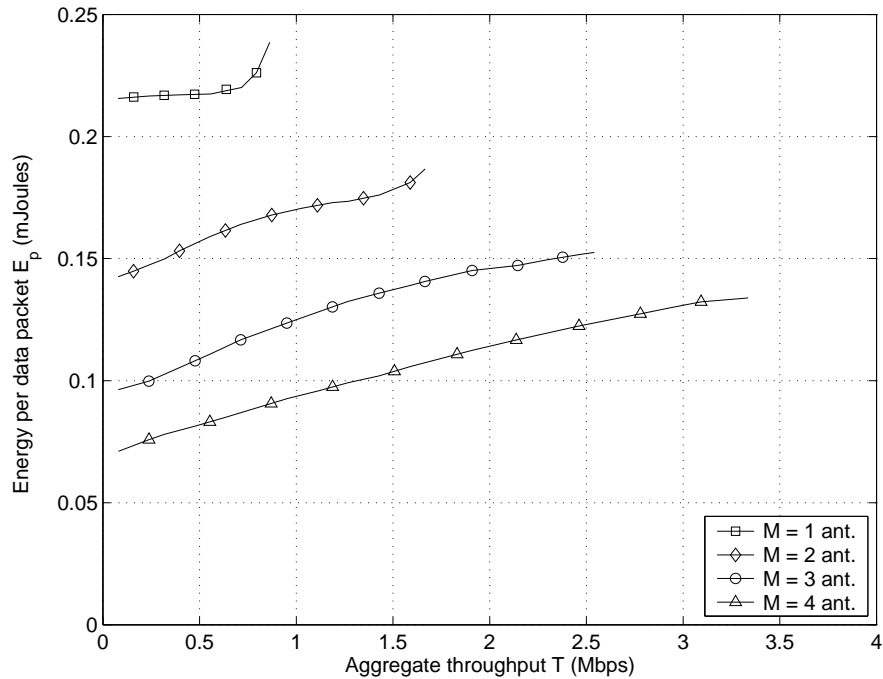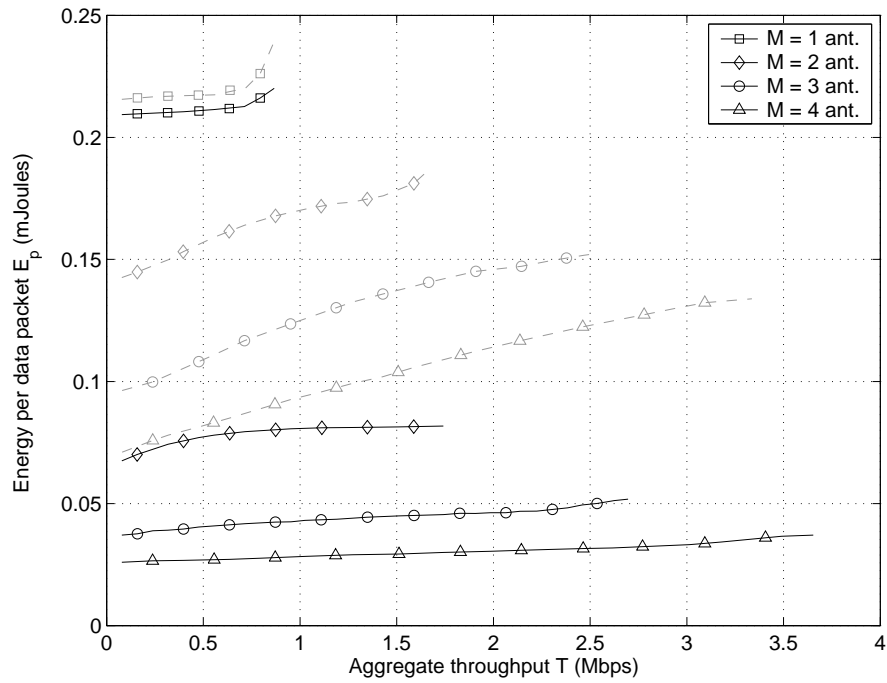
Figure 3.11: Average energy consumed per data packet versus aggregate throughput for the PBOA-TORB protocol, assuming $m = 13$ minislot pairs and optimum persistence probability p_o obtained from Table 3.2. Dashed curves correspond to the PBOA-ORB protocol.

4 Conclusions

In this dissertation, novel schemes have been proposed to control interference and increase throughput in two multiuser wireless network paradigms, namely, a TDD/CDMA cellular network with asymmetric traffic and an ad hoc network. The proposed schemes exploit the availability of multiple antennas at the nodes and combine interference management mechanisms from both the physical and the medium access control (or link) layers for enhanced network performance.

In Chapter 2, the problem of crossed-slot intercell interference in TDD/CDMA cellular networks with asymmetric traffic is considered. A decentralized scheme that mitigates crossed-slot intercell interference and, at the same time, ensures efficient resource utilization is proposed. This scheme combines an IADCA algorithm with space-time LMMSE joint detection at the receivers. The former avoids crossed-slot interference in channel allocation. The latter suppresses the remaining intercell interference by modeling it as colored noise with known spatio-temporal autocorrelation (LMMSE-CI joint detection) rather than as white noise (LMMSE-WI joint detection). The performance of the proposed scheme is evaluated in terms of SINR outage and average throughput via Monte Carlo simulations, and it is compared to that of benchmark RDCA and FCA schemes. The cases of single- and dual-antenna reception for perfect and imperfect CSI are investigated.

It is demonstrated that, in uplink, IADCA outperforms RDCA by avoiding strong BS-to-BS interference. It also achieves a considerable throughput gain over FCA, in spite of worse SINR outage, mainly due to flexible timeslot allocation that significantly reduces packet blocking. Interestingly, this gain is larger for dual- than single-antenna reception, implying that space-time LMMSE-CI joint detection is more beneficial to IADCA than FCA. In downlink, the performance differences among the three schemes are smaller since the effects of crossed-slot interference and packet blocking are milder

than in uplink. Nonetheless, IADCA achieves slightly higher average throughput than FCA (for dual-antenna reception) as well as RDCA (for heavy traffic loads). Based on the above results, it is concluded that IADCA, combined with space-time LMMSE-CI joint detection, provides a better tradeoff between resource utilization and crossed-slot interference mitigation than its FCA and RDCA counterparts.

In Chapter 3, two PHY-MAC cross-layer protocols are proposed with the goal of enhancing throughput in multiple-antenna ad hoc networks. The first increases spatial reuse by integrating medium access, power control, and optimum receive beamforming in a distributed manner and is named progressive back-off algorithm with optimum receive beamforming (PBOA-ORB). The second additionally incorporates transmit beamforming, on the premise of centralized control, and is named progressive back-off algorithm with transmit and optimum receive beamforming (PBOA-TORB). Both protocols are evaluated in terms of aggregate throughput and energy efficiency via simulations over a single-hop network with uniform traffic load. It is shown that the throughput of PBOA-ORB increases linearly with the number of antennas per node thanks to interference suppression provided by optimum receive beamforming. PBOA-TORB achieves only an incremental throughput gain over PBOA-ORB despite its centralized nature. However, it is significantly more energy efficient than PBOA-ORB thanks to extra array gain provided by transmit beamforming. Therefore, it is deduced that, in the context of the proposed protocols, receive beamforming mainly benefits spatial reuse (i.e., throughput), while transmit beamforming mainly benefits energy efficiency.

As a future research thrust, it is of interest to investigate PHY-MAC cross-layer designs other than PBOA-TORB that exploit the extra degrees of freedom provided by multiple transmit antennas more efficiently to further increase spatial reuse. It is desirable that these designs rely on local rather than network-wide channel state information and allow for distributed implementation. Potential techniques to be considered include random beamforming and spatial multiplexing, where each node contends for more than one packets simultaneously with different packets transmitted over different antennas.

A

Intercell-Interference-plus-Noise Autocorrelation Matrix Calculation

Similarly to $\boldsymbol{y}^{(r)}(m)$ given by (2.9), the vector of the rth antenna intercell-interference-plus-noise samples, which carry all the energy due the mth data symbols of the intercell packets, can be expressed as

$$\boldsymbol{n}^{(r)}(m) = \sum_{j=1}^{J} \boldsymbol{H}_I^{(r,j)} \boldsymbol{C}_{\boldsymbol{s},I}^{(j)} \boldsymbol{d}_I^{(j)}(m) + \tilde{\boldsymbol{w}}^{(r)}(m) \tag{A.1}$$

where $\tilde{\boldsymbol{w}}^{(r)}(m)$ is a complex Gaussian random vector with distribution $\mathcal{N}_c(\boldsymbol{0}, (N_o/T_c)\boldsymbol{I})$, and $\boldsymbol{H}_I^{(r,j)}$, $\boldsymbol{C}_{\boldsymbol{s},I}^{(j)}$, and $\boldsymbol{d}_I^{(j)}(m)$ are the intercell counterparts of $\boldsymbol{H}^{(r,k)}$, $\boldsymbol{C}_{\boldsymbol{s}}^{(k)}$, and $\boldsymbol{d}^{(k)}(m)$ defined in Section 2.1.2.

To compute the cross-correlation matrix of the rth and ρth antenna intercell-interference-plus-noise vectors, the following assumptions are made: 1) thermal noise processes on different receive antennas are uncorrelated; 2) data symbols are i.i.d. with unit average energy; and 3) in each cell, packets are randomly assigned to channelization codes from a set of $Q \geq K_{\max}$ OVSF codes with spreading factor Q in a uniform fashion (i.e., a packet is assigned to the qth code with probability $1/Q$ for $q = 1, \ldots, Q$). As a

result, it is

$$\boldsymbol{R_n}^{(r,\rho)} = E\left\{\boldsymbol{n}^{(r)}(m)\boldsymbol{n}^{(\rho)H}(m)\right\}$$

$$= \sum_{j_1=1}^{J}\sum_{j_2=1}^{J}\boldsymbol{H}_I^{(r,j_1)}E\left\{\boldsymbol{C}_{\boldsymbol{s},I}^{(j_1)}\boldsymbol{d}_I^{(j_1)}(m)\boldsymbol{d}_I^{(j_2)H}(m)\boldsymbol{C}_{\boldsymbol{s},I}^{(j_2)H}\right\}\boldsymbol{H}_I^{(\rho,j_2)H}$$

$$+ \frac{N_o}{T_c}\delta_{r,\rho}\boldsymbol{I} \tag{A.2a}$$

$$= \sum_{j_1=1}^{J}\sum_{j_2=1}^{J}\boldsymbol{H}_I^{(r,j_1)}E\left\{\boldsymbol{C}_{\boldsymbol{s},I}^{(j_1)}E\left\{\boldsymbol{d}_I^{(j_1)}(m)\boldsymbol{d}_I^{(j_2)H}(m)\right\}\boldsymbol{C}_{\boldsymbol{s},I}^{(j_2)H}\right\}\boldsymbol{H}_I^{(\rho,j_2)H}$$

$$+ \frac{N_o}{T_c}\delta_{r,\rho}\boldsymbol{I} \tag{A.2b}$$

$$= \sum_{j=1}^{J}\boldsymbol{H}_I^{(r,j)}E\left\{\boldsymbol{C}_{\boldsymbol{s},I}^{(j)}\boldsymbol{C}_{\boldsymbol{s},I}^{(j)H}\right\}\boldsymbol{H}_I^{(\rho,j)H} + \frac{N_o}{T_c}\delta_{r,\rho}\boldsymbol{I} \tag{A.2c}$$

$$= \sum_{j=1}^{J}\boldsymbol{H}_I^{(r,j)}\boldsymbol{H}_I^{(\rho,j)H} + \frac{N_o}{T_c}\delta_{r,\rho}\boldsymbol{I} \tag{A.2d}$$

where (A.2b) holds due to the independence between data symbols and channelization codes, while (A.2c) and (A.2d) follow by assumptions 2) and 3), respectively.

Clearly, the autocorrelation matrix $\boldsymbol{R_n}$ of $\boldsymbol{n}(m) = [\boldsymbol{n}^{(1)T}(m),\ldots,\boldsymbol{n}^{(R)T}(m)]^T$ is a block matrix whose $r\rho$th block is $\boldsymbol{R_n}^{(r,\rho)}$ for $r,\rho = 1,\ldots,R$.

B Channel Model used in Chapter 2 Simulations

B.1   MS-BS Links

The urban microcell 3GPP/3GPP2 NLOS spatial channel model, as explained in detail in [2], is used to simulate the MS-BS channel impulse responses. Specifically, the channel coefficients are generated following the process described in Sections 5.3.2 and 5.4 of [2]. The propagation loss is provided by the COST 231 Walfisch-Ikegami NLOS model (see Chapter 4 of [12]) and is expressed (in dB) as

$$\eta(d) = \begin{cases} \eta_o(d) + \eta_{\mathrm{rts}}(d) + \eta_{\mathrm{msd}}(d), & \text{if } \eta_{\mathrm{rts}}(d) + \eta_{\mathrm{msd}}(d) > 0 \\ \eta_o(d), & \text{if } \eta_{\mathrm{rts}}(d) + \eta_{\mathrm{msd}}(d) \leq 0 \end{cases} \tag{B.1}$$

where d is the MS-BS distance (in meters), and $\eta_o(d)$, $\eta_{\mathrm{rts}}(d)$, and $\eta_{\mathrm{msd}}(d)$ are the free-space loss, the rooftop-to-street diffraction loss, and the multiple screen diffraction loss, respectively (in decibels). The Walfisch-Ikegami NLOS model is restricted to carrier frequency 800 MHz $\leq f_c \leq$ 2000 MHz, BS antenna height 4 m $\leq h_{\mathrm{BS}} \leq$ 50 m, and MS antenna height 1 m $\leq h_{\mathrm{MS}} \leq$ 3 m. At carrier frequency $f_c = 1900$ MHz, it is $\eta_o(d) = 38 + 20 \log_{10} d$, while for a BS antenna height of 12.5 m, an MS antenna height of 1.5 m, a building height of 12 m, a building separation of 50 m, a street width of 25 m, a path orientation of 30°, and a metropolitan center environment, it is $\eta_{\mathrm{rts}}(d) + \eta_{\mathrm{msd}}(d) = -3.44 + 18 \log_{10} d$.

B.2   MS-MS Links

The MS-MS channel coefficients are generated in the same way as the MS-BS channel coefficients, following the process described in Sections 5.3.2 and 5.4 of [2], with

the difference that both the angles-of-arrival (AoAs) and angles-of-departure (AoDs) of the various multipath components are determined according to steps 10 and 11 of the process. The MS-MS propagation loss is approximated by the MS-BS propagation loss predicted by the COST 231 Walfisch-Ikegami NLOS model for the minimum allowed BS antenna height (i.e., 4 m), keeping all the other parameters the same as in the MS-BS case. This results in

$$\eta_{\text{rts}}(d) + \eta_{\text{msd}}(d) = \begin{cases} -30.27 + 0.0128d + 28\log_{10} d, & \text{if } d < 500\text{m} \\ -23.87 + 28\log_{10} d, & \text{if } d \geq 500 \text{ m} \end{cases}. \tag{B.2}$$

B.3 BS-BS Links

The BS-BS channel coefficients are generated in the same way as the MS-BS channel coefficients, following the process described in Sections 5.3.2 and 5.4 of [2], with the difference that both the AoAs and AoDs of the various multipath components are determined according to steps 7 and 9 of the process. For the BS-BS propagation loss, the Maciel-Bertoni-Xia model (which is described in [26] and adopted in [14]) is used. According to this model, the propagation loss is given by (B.1), where $\eta_{\text{rts}}(d)$ and $\eta_{\text{msd}}(d)$ are calculated in a different way than in the Walfisch-Ikegami NLOS model. Approximating a BS-BS link by an MS-BS link with an MS antenna height of 11.5 m and a BS antenna height of 12.5 m and assuming a building height of 12 m, a building separation of 50 m, a mobile-to-diffracting-edge-distance of 10 m, and carrier frequency $f_c = 1900$ MHz, the Maciel-Bertoni-Xia model results in $\eta_{\text{rts}}(d) + \eta_{\text{msd}}(d) = -19.5 + 19.96\log_{10} d$.

C Proof of Proposition 1

Consider the ith link from the set $\mathcal{L}^{(k)}$ of active links in the kth RTS minislot. Contending node t_i transmits an RTS packet, using power $P_i^{(k)}$ and transmit beamforming vector $\boldsymbol{v}_i$, which is successfully received by silent node r_i, after optimum receive beamforming with vector $\boldsymbol{u}_i^{(k)}$, at (maximum) SINR

$$\gamma_i^{(k)} = \frac{P_i^{(k)} G_{ii} |\boldsymbol{u}_i^{(k)H} \boldsymbol{H}_{ii} \boldsymbol{v}_i|^2}{\sum\limits_{\substack{j \neq i \\ j \in \mathcal{L}^{(k)}}} P_j^{(k)} G_{ij} |\boldsymbol{u}_i^{(k)H} \boldsymbol{H}_{ij} \boldsymbol{v}_j|^2 + \sigma_w^2} \geq \gamma_T.$$

According to the PBOA-ORB protocol, provided that node t_i receives a CTS packet containing the scaling factor $\alpha_i^{(k)} = \min\{1, (1+\epsilon)\gamma_T/\gamma_i^{(k)}\}$ from node r_i, it becomes locked and transmits at power $P_i^{(k+1)} = \alpha_i^{(k)} P_i^{(k)}$ in the $(k+1)$th RTS minislot. Irrespective of the outcome for the other transmitting nodes t_j, $j \neq i$, during the kth minislot pair (i.e., whether they are unsuccessfully contending, successfully contending, or locked), their transmit powers will be either $P_j^{(k+1)} = 0$ or $P_j^{(k+1)} \leq P_j^{(k)}$ in the $(k+1)$th RTS minislot. Thus, assuming channel time invariance, the SINR at node r_i, after optimum receive beamforming with vector $\boldsymbol{u}_i^{(k+1)}$, is

$$\gamma_i^{(k+1)} = \frac{P_i^{(k+1)} G_{ii} |\boldsymbol{u}_i^{(k+1)H} \boldsymbol{H}_{ii} \boldsymbol{v}_i|^2}{\sum\limits_{\substack{j \neq i \\ j \in \mathcal{L}^{(k)}}} P_j^{(k+1)} G_{ij} |\boldsymbol{u}_i^{(k+1)H} \boldsymbol{H}_{ij} \boldsymbol{v}_j|^2 + \sigma_w^2} \tag{C.1a}$$

$$\geq \frac{P_i^{(k+1)} G_{ii} |\boldsymbol{u}_i^{(k)H} \boldsymbol{H}_{ii} \boldsymbol{v}_i|^2}{\sum\limits_{\substack{j \neq i \\ j \in \mathcal{L}^{(k)}}} P_j^{(k+1)} G_{ij} |\boldsymbol{u}_i^{(k)H} \boldsymbol{H}_{ij} \boldsymbol{v}_j|^2 + \sigma_w^2} \tag{C.1b}$$

$$\geq \frac{P_i^{(k)} G_{ii} |\boldsymbol{u}_i^{(k)H} \boldsymbol{H}_{ii} \boldsymbol{v}_i|^2}{\sum\limits_{\substack{j \neq i \\ j \in \mathcal{L}^{(k)}}} P_j^{(k)} G_{ij} |\boldsymbol{u}_i^{(k)H} \boldsymbol{H}_{ij} \boldsymbol{v}_j|^2 + \sigma_w^2} \min\{1, (1+\epsilon)\gamma_T/\gamma_i^{(k)}\} \tag{C.1c}$$

$$= \min\{\gamma_i^{(k)}, (1+\epsilon)\gamma_T\} \geq \gamma_T \tag{C.1d}$$

where (C.1b) follows by the definition of $\boldsymbol{u}_i^{(k+1)}$ as the ORB vector and (C.1c) by the fact that $0 \leq P_j^{(k+1)} \leq P_j^{(k)}$ for $j \neq i$. Therefore, successful reception of the RTS packet sent by node t_i in the $(k+1)$th RTS minislot is guaranteed, as suggested by Proposition 1.

D Proof of Proposition 2

Consider the ith link from the set of successful links $\mathcal{S}^{(k)}$ in the kth RTS minislot. Contending node t_i transmits an RTS packet using power $P_i^{(k)}$ and transmit beamforming vector $\boldsymbol{v}_i^{(k)}$, which is received by silent node r_i, after optimum receive beamforming with vector $\boldsymbol{u}_i^{(k)}$, at SINR

$$\gamma_i^{(k)} = \frac{P_i^{(k)} G_{ii} |\boldsymbol{u}_i^{(k)H} \boldsymbol{H}_{ii} \boldsymbol{v}_i^{(k)}|^2}{\displaystyle\sum_{\substack{j \neq i \\ j \in \mathcal{S}^{(k)}}} P_j^{(k)} G_{ij} |\boldsymbol{u}_i^{(k)H} \boldsymbol{H}_{ij} \boldsymbol{v}_j^{(k)}|^2 + n_i^{(k)}} \geq \gamma_T$$

where $n_i^{(k)}$ captures thermal noise and interference due to unsuccessful links $\bar{\mathcal{S}}^{(k)}$. In the kth CTS minislot, node r_i responds with a CTS packet sent at power $\tilde{P}_i^{(k)}$ using the transmit beamforming vector $\boldsymbol{u}_i^{(k)*}$. Based on the PBOA-TORB protocol, the power level $\tilde{P}_i^{(k)}$ is determined by applying the Network Duality Theorem on the network topology formed by the successful links $\mathcal{S}^{(k)}$, for target SINR $\gamma_{i,out}^{(k)}$ defined in (3.17). Note that $\gamma_{i,out}^{(k)} \geq \gamma_T$ since, for $P_{i,out}^{(k)} = P_i^{(k)} \min\{1, (1+\epsilon)\gamma_T/\gamma_i^{(k)}\}$, it is

$$\begin{aligned}
\gamma_{i,out}^{(k)} &= \frac{P_{i,out}^{(k)} G_{ii} |\boldsymbol{u}_i^{(k)H} \boldsymbol{H}_{ii} \boldsymbol{v}_i^{(k)}|^2}{\displaystyle\sum_{\substack{j \neq i \\ j \in \mathcal{S}^{(k)}}} P_{j,out}^{(k)} G_{ij} |\boldsymbol{u}_i^{(k)H} \boldsymbol{H}_{ij} \boldsymbol{v}_j^{(k)}|^2 + n_i^{(k)}} \\[2mm]
&\geq \frac{P_i^{(k)} G_{ii} |\boldsymbol{u}_i^{(k)H} \boldsymbol{H}_{ii} \boldsymbol{v}_i^{(k)}|^2}{\displaystyle\sum_{\substack{j \neq i \\ j \in \mathcal{S}^{(k)}}} P_j^{(k)} G_{ij} |\boldsymbol{u}_i^{(k)H} \boldsymbol{H}_{ij} \boldsymbol{v}_j^{(k)}|^2 + n_i^{(k)}} \min\{1, (1+\epsilon)\gamma_T/\gamma_i^{(k)}\} \\[2mm]
&= \min\{\gamma_i^{(k)}, (1+\epsilon)\gamma_T\} \geq \gamma_T.
\end{aligned} \qquad (\text{D.1})$$

Node t_i employs the ORB vector $\tilde{\boldsymbol{u}}_i^{(k)H}$ to receive the CTS packet sent by r_i at maximum SINR $\tilde{\gamma}_i^{(k)}$. This SINR satisfies

$$\tilde{\gamma}_i^{(k)} = \frac{\tilde{P}_i^{(k)} G_{ii} |\tilde{\boldsymbol{u}}_i^{(k)H} \boldsymbol{H}_{ii}^T \boldsymbol{u}_i^{(k)*}|^2}{\displaystyle\sum_{\substack{j \neq i \\ j \in \mathcal{S}^{(k)}}} \tilde{P}_j^{(k)} G_{ji} |\tilde{\boldsymbol{u}}_i^{(k)H} \boldsymbol{H}_{ji}^T \boldsymbol{u}_j^{(k)*}|^2 + \sigma_w^2} \tag{D.2a}$$

$$\geq \frac{\tilde{P}_i^{(k)} G_{ii} |\boldsymbol{v}_i^{(k)T} \boldsymbol{H}_{ii}^T \boldsymbol{u}_i^{(k)*}|^2}{\displaystyle\sum_{\substack{j \neq i \\ j \in \mathcal{S}^{(k)}}} \tilde{P}_j^{(k)} G_{ji} |\boldsymbol{v}_i^{(k)T} \boldsymbol{H}_{ji}^T \boldsymbol{u}_j^{(k)*}|^2 + \sigma_w^2} \tag{D.2b}$$

$$= \gamma_{i,out}^{(k)} \geq \gamma_T \tag{D.2c}$$

where (D.2b) follows by definition of the ORB vector, and (D.2c) follows by (3.18a) and (D.1). Consequently, successful reception of the CTS packet is guaranteed and Remark 1 in Section 3.3.3 is proved.

In the $(k+1)$th RTS minislot, node t_i is locked and transmits an RTS packet using power $P_i^{(k+1)}$ and beamforming vector $\boldsymbol{v}_i^{(k+1)} = \tilde{\boldsymbol{u}}_i^{(k)*}$. The power level $P_i^{(k+1)}$ is determined by means of the Network Duality Theorem on the network topology formed by the successful links $\mathcal{S}^{(k)}$, for target SINR $\tilde{\gamma}_{i,out}^{(k)}$ defined in (3.21). Following the same steps as in (D.1), it can be shown that

$$\tilde{\gamma}_{i,out}^{(k)} \geq \min\{\tilde{\gamma}_i^{(k)}, (1+\epsilon)\gamma_T\} \geq \gamma_T. \tag{D.3}$$

Transmitting nodes corresponding to successful links $\mathcal{S}^{(k)}$ update their power and beamforming vector in a similar fashion as node t_i, while those corresponding to unsuccessful links $\bar{\mathcal{S}}^{(k)}$ randomly back off; only a subset $\bar{\mathcal{S}}_p^{(k)} \subseteq \bar{\mathcal{S}}^{(k)}$ of them persist contending, using the same power $P_\ell^{(k+1)} = P_\ell^{(k)}$ and beamforming vector $\boldsymbol{v}_\ell^{(k+1)} = \boldsymbol{v}_\ell^{(k)}$ as in the kth RTS minislot. Assuming channel time invariance, the SINR at node r_i, after optimum receive

beamforming with vector $\boldsymbol{u}_i^{(k+1)}$, is

$$\gamma_i^{(k+1)} = \frac{P_i^{(k+1)} G_{ii} |\boldsymbol{u}_i^{(k+1)H} \boldsymbol{H}_{ii} \boldsymbol{v}_i^{(k+1)}|^2}{\displaystyle\sum_{\substack{j \neq i \\ j \in \mathcal{S}^{(k)}}} P_j^{(k+1)} G_{ij} |\boldsymbol{u}_i^{(k+1)H} \boldsymbol{H}_{ij} \boldsymbol{v}_j^{(k+1)}|^2 + \sum_{\ell \in \bar{\mathcal{S}}_p^{(k)}} P_\ell^{(k)} G_{i\ell} |\boldsymbol{u}_i^{(k+1)H} \boldsymbol{H}_{i\ell} \boldsymbol{v}_\ell^{(k)}|^2 + \sigma_w^2}$$

$$\tag{D.4a}$$

$$\geq \frac{P_i^{(k+1)} G_{ii} |\boldsymbol{u}_i^{(k)H} \boldsymbol{H}_{ii} \boldsymbol{v}_i^{(k+1)}|^2}{\displaystyle\sum_{\substack{j \neq i \\ j \in \mathcal{S}^{(k)}}} P_j^{(k+1)} G_{ij} |\boldsymbol{u}_i^{(k)H} \boldsymbol{H}_{ij} \boldsymbol{v}_j^{(k+1)}|^2 + \sum_{\ell \in \bar{\mathcal{S}}_p^{(k)}} P_\ell^{(k)} G_{i\ell} |\boldsymbol{u}_i^{(k)H} \boldsymbol{H}_{i\ell} \boldsymbol{v}_\ell^{(k)}|^2 + \sigma_w^2}$$

$$\tag{D.4b}$$

$$\geq \frac{P_i^{(k+1)} G_{ii} |\boldsymbol{u}_i^{(k)H} \boldsymbol{H}_{ii} \boldsymbol{v}_i^{(k+1)}|^2}{\displaystyle\sum_{\substack{j \neq i \\ j \in \mathcal{S}^{(k)}}} P_j^{(k+1)} G_{ij} |\boldsymbol{u}_i^{(k)H} \boldsymbol{H}_{ij} \boldsymbol{v}_j^{(k+1)}|^2 + \underbrace{\sum_{\ell \in \bar{\mathcal{S}}^{(k)}} P_\ell^{(k)} G_{i\ell} |\boldsymbol{u}_i^{(k)H} \boldsymbol{H}_{i\ell} \boldsymbol{v}_\ell^{(k)}|^2 + \sigma_w^2}_{n_i^{(k)}}}$$

$$\tag{D.4c}$$

$$= \tilde{\gamma}_{i,out}^{(k)} \geq \gamma_T \tag{D.4d}$$

where (D.4c) follows due to $\bar{\mathcal{S}}_p^{(k)} \subseteq \bar{\mathcal{S}}^{(k)}$ and (D.4d) due to (3.22) and (D.3). Therefore, successful reception of the RTS packet sent by node t_i in the $(k+1)$th RTS minislot is guaranteed, as suggested by Proposition 2.

Abbreviations

3GPP	third-generation partnership project
AWGN	additive white Gaussian noise
BS	base station
cdf	cumulative distribution function
CDMA	code-division multiple access
CI	colored intercell interference
CSI	channel state information
CSMA/CA	carrier-sensing multiple access with collision avoidance
CTS	clear to send
dB	decibels, $10\log_{10}(\cdot)$
DCA	dynamic channel allocation
DL	downlink
FCA	fixed channel allocation
FDD	frequency-division duplexing
FIFO	first in first out
GPS	global positioning system
IADCA	interference-aware dynamic channel allocation
IEEE	Institute of Electrical and Electronic Engineers
i.i.d.	independent and identically distributed
ISI	intersymbol interference
LMMSE	linear minimum mean square error
LMS	least-mean squares
LOS	line-of-sight
MAC	medium access control
MAI	multiple access interference
MIMO	multiple input multiple output
MMSE	minimum mean square error
MS	mobile station
NLOS	non-line-of-sight
ORB	optimum receive beamforming
OVSF	orthogonal variable spreading factor
PBOA	progressive back-off algorithm
PHY	physical (layer)
QPSK	quadrature phase-shift keying
RDCA	random dynamic channel allocation

RLS	recursive least squares
RRC	root raised cosine
RTS	request to send
SINR	signal-to-interference-plus-noise ratio
SNR	signal-to-noise ratio
TDD	time-division duplexing
TORB	transmit and optimum receive beamforming
UL	uplink
UMTS	universal mobile telecommunications system
UTRA	universal terrestrial radio access
WI	white intercell interference

Symbols

j	$\sqrt{-1}$
$\star$	convolution operator
$\otimes$	Kronecker product operator
$\neq$	not equal
$<$	less than
$\leq$	less than or equal
$>$	greater than
$\geq$	greater than or equal
$\in$	is an element of
$\subseteq$	is a subset of
$\mathbb{N}$	set of natural numbers
$\mathbb{R}$	set of real numbers
$\mathbb{C}$	set of complex numbers
$\{x_i, i = 1, \ldots, N\}$	set of elements $x_1, \ldots, x_N$
$|\mathcal{L}|$	cardinality of set $\mathcal{L}$
$|\cdot|$	Euclidean norm
$\lfloor \cdot \rfloor$	floor function
$\lceil \cdot \rceil$	ceiling function
$[\cdot]$	closed interval
$[\cdot)$	semi-open interval
$\mathbf{1}$	vector with elements equal to 1
$\boldsymbol{x} = [x_1, \ldots, x_N]$	vector with elements $x_1, \ldots, x_N$
$\{\boldsymbol{x}_i\}_{i \in \mathcal{L}}$	set of vectors $\boldsymbol{x}_i$ with index i taking values in set $\mathcal{L}$
$\boldsymbol{I}_N$	$N \times N$ identity matrix
$\boldsymbol{H} = \left[H_{i,j} \right]$	matrix with elements $H_{i,j}$
$H_{i,j} = \left[\boldsymbol{H} \right]_{i,j}$	ijth element of matrix $\boldsymbol{H}$
$\angle \cdot$	phase of a complex number
$\hat{(\cdot)}$	estimate of
$(\cdot)^*$	complex conjugate
$(\cdot)^{-1}$	inverse
$(\cdot)^T$	transpose operator
$(\cdot)^H$	Hermitian (complex conjugate transpose) operator
$\mathrm{tr}(\cdot)$	trace of (square matrix)
$\mathrm{rank}(\cdot)$	rank of matrix
$E\{\cdot\}$	expectation operator

$\mathcal{Q}(\cdot)$	Gaussian Q-function
$\delta(\cdot)$	Dirac delta function
$\delta_{i,j}$	Kronecker delta function
max	maximum
min	minimum
argmin	minimizer of
argmax	maximizer of
$\prod_{n=1}^{N}$	multiple product
$\sum_{i=1}^{N}$	multiple sum
$x \bmod y$	x modulo y
$x \times y$	product of x and y
$\mathcal{N}_c(\bar{x}, \sigma^2)$	complex Gaussian distribution with mean $\bar{x}$ and variance σ^2

Bibliography

[1] *Spreading and modulation (TDD)*, 3rd Generation Partnership Project Technical Specification Group, Radio Access Network Working Group 1, Tech. Spec. 3GPP TS 25.223 (Rel-7), Mar. 2006. [Online]. Available: http://www.3gpp.org/ftp/Specs/html-info/25223.htm

[2] *Spatial Channel Model for Multiple Input Multiple Output (MIMO) Simulations*, 3rd Generation Partnership Project Technical Specification Group, Radio Access Network Working Group 1, Tech. Rep. 3GPP TR 25.996 (Rel-7), June 2007. [Online]. Available: http://www.3gpp.org/ftp/Specs/html-info/25996.htm

[3] G. Bianchi, "Performance analysis of the IEEE 802.11 distributed coordination function," *IEEE J. Select. Areas Commun.*, vol. 18, no. 3, pp. 535–547, Mar. 2000.

[4] G. Caire and U. Mitra, "Structured multiuser channel estimation for block-synchronous DS/CDMA," *IEEE Trans. Commun.*, vol. 49, no. 9, pp. 1605–1617, Sept. 2001.

[5] P. Casari, M. Levorato, and M. Zorzi, "On the implications of layered space-time multiuser detection on the design of MAC protocols for ad hoc networks," in *Proc. IEEE Intern. Symp. on Personal, Indoor and Mobile Radio Commun. (PIMRC)*, Berlin, Germany, Sept. 2005, pp. 1354–1360.

[6] ——, "MAC/PHY cross-layer design of MIMO ad hoc networks with layered multiuser detection," *IEEE Trans. Wireless Commun.*, vol. 7, no. 11, pp. 4596–4607, Nov. 2008.

[7] P. Castoldi and H. Kobayashi, "Co-channel interference mitigation detectors for multirate transmission in TD-CDMA systems," *IEEE J. Select. Areas Commun.*, vol. 20, no. 2, pp. 273–286, Feb. 2002.

[8] J.-H. Chang, L. Tassiulas, and F. Rashid-Farrokhi, "Joint transmitter receiver diversity for efficient space division multiaccess," *IEEE Trans. Wireless Commun.*, vol. 1, no. 1, pp. 16–27, Jan. 2002.

[9] B. Chen and M. J. Gans, "MIMO communications in ad hoc networks," *IEEE Trans. Signal Processing*, vol. 54, no. 7, pp. 2773–2783, July 2006.

[10] C.-J. Chen and L.-C. Wang, "Suppressing opposite-direction interference in TDD/CDMA systems with asymmetric traffic by antenna beamforming," *IEEE Trans. Veh. Technol.*, vol. 53, no. 4, pp. 956–967, July 2004.

[11] W. Cooper, J. R. Zeidler, and R. R. Bitmead, "Modeling dynamic channel-allocation algorithms in multi-BS TDD wireless networks with Internet-based traffic," *IEEE Trans. Veh. Technol.*, vol. 53, no. 3, pp. 783–804, May 2004.

[12] *Digital Mobile Radio Towards Future Generation Systems*, COST 231, Final Rep. [Online]. Available: http://www.lx.it.pt/cost231/final_report.htm

[13] R. Esmailzadeh, M. Nakagawa, and A. Jones, "TDD-CDMA for the 4th generation of wireless communications," *IEEE Wireless Commun. Mag.*, vol. 10, no. 4, pp. 8–15, Aug. 2003.

[14] *Selection Procedures for the Choice of Radio Transmission Technologies of the UMTS (UMTS 30.03)*, Eur. Telecommun. Stand. Inst., Tech. Rep. ETSI TR 101 112 v3.2.0, Apr. 1998. [Online]. Available: http://webapp.etsi.org/exchangefolder/ tr_101112v030200p.pdf

[15] G. J. Foschini, G. D. Golden, R. A. Valenzuela, and P. W. Wolniansky, "Simplified processing for high spectral efficiency wireless communication employing multi-element arrays," *IEEE J. Select. Areas Commun.*, vol. 17, no. 11, pp. 1841–1852, Nov. 1999.

[16] G. H. Golub and C. F. V. Loan, *Matrix Computations*, 3rd ed. Baltimore: Johns Hopkins University Press, 1996.

[17] M. Haardt, A. Klein, R. Koehn, S. Oestreich, M. Purat, V. Sommer, and T. Ulrich, "The TD-CDMA based UTRA TDD mode," *IEEE J. Select. Areas Commun.*, vol. 18, no. 8, pp. 1375–1385, Aug. 2000.

[18] H. Haas and S. McLaughlin, "A dynamic channel assignment algorithm for a hybrid TDMA/CDMA-TDD interface using the novel TS-opposing technique," *IEEE J. Select. Areas Commun.*, vol. 19, no. 10, pp. 1831–1846, Oct. 2001.

[19] H. Holma, S. Heikkinen, O.-A. Lehtinen, and A. Toskala, "Interference considerations for the time division duplex mode of the UMTS terrestrial radio access," *IEEE J. Select. Areas Commun.*, vol. 18, no. 8, pp. 1386–1393, Aug. 2000.

[20] A. M. Hunter, J. G. Andrews, and S. P. Weber, "Capacity scaling of ad hoc networks with spatial diversity," in *Proc. IEEE Intern. Symp. on Inform. Theory (ISIT)*, Nice, France, June 2007, pp. 1446–1450.

[21] W. S. Jeon and D. G. Jeong, "Comparison of time slot allocation strategies for CDMA/TDD systems," *IEEE J. Select. Areas Commun.*, vol. 18, no. 7, pp. 1271–1278, July 2000.

[22] W. Jeong and M. Kavehrad, "Cochannel interference reduction in dynamic-TDD fixed wireless applications, using time slot allocation algorithms," *IEEE Trans. Commun.*, vol. 50, no. 10, pp. 1627–1636, Oct. 2002.

[23] N. Jindal, J. G. Andrews, and S. Weber, "Rethinking MIMO for wireless networks: Linear throughput increases with multiple receive antennas," in *Proc. IEEE Int. Conf. Commun. (ICC)*, Dresden, Germany, June 2009.

[24] P. Jung and J. Blanz, "Joint detection with coherent receiver antenna diversity in CDMA mobile radio systems," *IEEE Trans. Veh. Technol.*, vol. 44, no. 1, pp. 76–88, Feb. 1995.

[25] M. Lindström, "Improved TDD resource allocation through inter-mobile interference avoidance," in *Proc. IEEE 53rd Veh. Technol. Conf. (VTC)*, Rhodes, Greece, May 2001, pp. 1027–1031.

[26] L. R. Maciel, H. L. Bertoni, and H. H. Xia, "Unified approach to prediction of propagation over buildings for all ranges of base station antenna height," *IEEE Trans. Veh. Technol.*, vol. 42, no. 1, pp. 41–45, Feb. 1993.

[27] W. H. Mow, "A new unified construction of perfect root-of-unity sequences," in *Proc. IEEE 4th Int. Symp. Spread Spectrum Techn. Applicat. (ISSSTA)*, Mainz, Germany, Sept. 1996, pp. 955–959.

[28] A. Muqattash and M. Krunz, "CDMA-based MAC protocol for wireless ad hoc networks," in *Proc. ACM MOBIHOC*, Annapolis, MD, June 2003, pp. 153–164.

[29] J. Nasreddine and X. Lagrange, "Time slot allocation based on a path gain division scheme for TD-CDMA TDD systems," in *Proc. IEEE 57th Veh. Technol. Conf. (VTC)*, Jeju, Korea, Apr. 2003, pp. 1410–1414.

[30] S. Ni and L. Hanzo, "Genetically enhanced performance of a UTRA-like time-division duplex CDMA network," in *Proc. IEEE 61st Veh. Technol. Conf. (VTC)*, Stockholm, Sweden, May 2005, pp. 2279–2283.

[31] M. Park, R. W. Heath Jr., and S. M. Nettles, "Improving throughput and fairness for MIMO ad hoc networks using antenna selection diversity," in *Proc. IEEE Global Commun. Conf. (GLOBECOM)*, Dallas, TX, Nov. 2004, pp. 3363–3367.

[32] M. Peng, J. Zhang, X. Zhu, and W. Wang, "A novel dynamic channel allocation scheme to support asymmetrical services in TDD-CDMA systems," in *Proc. IEEE Int. Conf. Commun. Technol. (ICCT)*, Beijing, China, Apr. 2003, pp. 794–798.

[33] H. V. Poor and S. Verdù, "Probability of error in MMSE multiuser detection," *IEEE Trans. Inform. Theory*, vol. 43, no. 3, pp. 858–871, May 1997.

[34] J. G. Proakis, *Digital Communications*, 4th ed. New York, NY: McGraw-Hill, 2001.

[35] F. Rashid-Farrokhi, K. J. R. Liu, and L. Tassiulas, "Transmit beamforming and power control for cellular wireless systems," *IEEE J. Select. Areas Commun.*, vol. 16, no. 8, pp. 1437–1450, Oct. 1998.

[36] F. Rashid-Farrokhi, L. Tassiulas, and K. J. R. Liu, "Joint optimal power control and beamforming in wireless networks using antenna arrays," *IEEE Trans. Commun.*, vol. 46, no. 10, pp. 1313–1324, Oct. 1998.

[37] K. Römer, "Time synchronization in ad hoc networks," in *Proc. ACM MOBIHOC*, Long Beach, CA, Oct. 2001, pp. 173–182.

[38] B. Song, R. L. Cruz, and B. D. Rao, "Network duality for multiuser MIMO beamforming networks and applications," *IEEE Trans. Commun.*, vol. 55, no. 3, pp. 618–629, Mar. 2007.

[39] Y. Song and S. D. Blostein, "Channel estimation and data detection for MIMO systems under spatially and temporally colored interference," *EURASIP J. Appl. Signal Process.*, vol. 2004, no. 5, pp. 685–695, July-Aug. 2004.

[40] A. Stamoulis and N. Al-Dhahir, "Impact of space-time block codes on 802.11 network throughput," *IEEE Trans. Wireless Commun.*, vol. 2, no. 5, pp. 1029–1039, Sept. 2003.

[41] B. Steiner and P. Jung, "Optimum and suboptimum channel estimation for the uplink of CDMA mobile radio systems with joint detection," *Eur. Trans. Telecommun.*, vol. 5, no. 1, pp. 39–50, Jan.-Feb. 1994.

[42] V. Tarokh, H. Jafarkhani, and A. R. Calderbank, "Space-time block coding for wireless communications: Performance results," *IEEE J. Select. Areas Commun.*, vol. 17, no. 3, pp. 451–460, Mar. 1999.

[43] V. Tarokh, A. Naguib, N. Seshadri, and A. R. Calderbank, "Space-time codes for high data rate wireless communication: Performance criteria in the presence of channel estimation errors, mobility, and multiple paths," vol. 47, no. 2, pp. 199–207, Feb. 1999.

[44] V. Tarokh, N. Seshadri, and A. R. Calderbank, "Space-time codes for high data rate wireless communication: Performance criterion and code construction," *IEEE Trans. Inform. Theory*, vol. 44, no. 2, pp. 744–765, Mar. 1998.

[45] S. Toumpis and A. J. Goldsmith, "New media access protocols for wireless ad hoc networks based on cross-layer principles," *IEEE Trans. Wireless Commun.*, vol. 5, no. 8, pp. 2228–2241, Aug. 2006.

[46] H. L. Van Trees, *Optimum Array Processing. Part IV of Detection, Estimation and Modulation Theory.* New York: Wiley-Interscience, 2002.

[47] A. Vanelli-Coralli, R. Padovani, J. Hou, and J. E. Smee, "Capacity of cell clusters with coordinated processing," in *Proc. Inform. Theory Applicat. (ITA) Inaugural Workshop*, San Diego, CA: Univ. Calif., Feb. 2006. [Online]. Available: http://ita.ucsd.edu/workshop/06/talks/papers/118.pdf

[48] P. Viswanath and D. N. C. Tse, "Sum capacity of the vector Gaussian broadcast channel and uplink-downlink duality," *IEEE Trans. Inf. Theory*, vol. 49, no. 8, pp. 1912–1921, Aug. 2003.

[49] M. Vollmer, M. Haardt, and J. Götze, "Comparative study of joint-detection techniques for TD-CDMA based mobile radio systems," *IEEE J. Select. Areas Commun.*, vol. 19, no. 8, pp. 1461–1475, Aug. 2001.

[50] L.-C. Wang, S.-Y. Huang, and Y.-C. Tseng, "Interference analysis and resource allocation for TDD-CDMA systems to support asymmetric services by using directional antennas," *IEEE Trans. Veh. Technol.*, vol. 54, no. 3, pp. 1056–1069, May 2005.

[51] M. Weckerle and A. Papathanassiou, "Performance analysis of multi-antenna TD-CDMA receivers with estimation and consideration of the interference covariance matrix," *Int. J. Wireless Inform. Netw.*, vol. 6, no. 3, pp. 157–170, July 1999.

[52] S.-H. Wie and D.-H. Cho, "Time slot allocation scheme based on a region division in CDMA/TDD systems," in *Proc. IEEE 53rd Veh. Technol. Conf. (VTC)*, Rhodes, Greece, May 2001, pp. 2445–2449.

[53] J. H. Winters and J. Salz, "Upper bounds on the bit-error rate of optimum combining in wireless systems," *IEEE Trans. Commun.*, vol. 46, no. 12, pp. 1619–1624, Dec. 1998.

[54] D. Zhou and T.-H. Lai, "An accurate and scalable clock synchronization protocol for IEEE 802.11-based multihop ad hoc networks," *IEEE Trans. Parallel Distrib. Syst.*, vol. 18, no. 12, pp. 1797–1808, Dec. 2007.

[55] M. Zorzi, J. R. Zeidler, A. Anderson, B. Rao, J. G. Proakis, A. L. Swindlehurst, M. Jensen, and S. V. Krishnamurthy, "Cross-layer issues in MAC protocol design for MIMO ad hoc networks," *IEEE Wireless Commun. Mag.*, vol. 13, no. 4, pp. 62–76, Aug. 2006.